

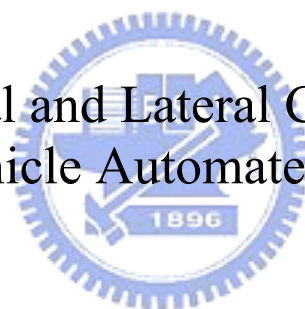
國立交通大學

電機與控制工程系

博士論文

自動車輛駕駛縱向暨橫向控制設計

Longitudinal and Lateral Control Design
for Vehicle Automated Driving



研究生：蔣欣翰

指導教授：吳炳飛 教授

李祖添 教授

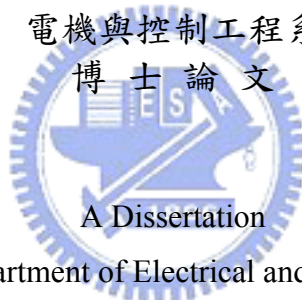
吳幸珍 教授

中華民國九十七年二月

自動車輛駕駛縱向暨橫向控制設計
Longitudinal and Lateral Control Design for Vehicle Automated Driving

研究生：蔣欣翰	Student : Hsin-Han Chiang
指導教授：吳炳飛	Advisor(s) : Bing-Fei Wu
李祖添	Tsu-Tian Lee
吳幸珍	Shinq-Jen Wu

國立交通大學
電機與控制工程系
博士論文



Submitted to Department of Electrical and Control Engineering
College of Electrical and Computer Engineering
National Chiao Tung University
in partial Fulfillment of the Requirements
for the Degree of
Doctor of Philosophy
in

Electrical and Control Engineering

February 2008

Hsinchu, Taiwan, Republic of China

中華民國九十七年二月

自動車輛駕駛縱向暨橫向控制設計

研究生：蔣欣翰

指導教授：吳炳飛 博士

李祖添 博士

吳幸珍 博士

國立交通大學電機與控制工程系博士班

摘 要

車輛駕駛自動化是先進車輛系統(Advanced vehicle systems)主要研究部份之一，Taiwan iTS-1 是由交通大學自行開發之自動駕駛實驗車。在本論文中，我們介紹此一多模式自動駕駛之系統，內容包含控制目標之決定、系統架構設計、車輛動態模型驗證、控制演算法、以及路上測試。此系統實現於 Taiwan iTS-1 並於真實交通環境高速道路及市區道路測試，驗證其正確及有效性。我們設計一個階層控制的自動駕駛系統，上層控制(Upper-level control)判斷道路交通環境並決定是否啟動道路保持、道路切換、定速及適應巡航控制、以及停走操作模式，並計算該模式操作所需之安全車速及行駛軌跡，再交由車體控制(Vehicle-body control)來執行。為使系統能像駕駛人一般控制車輛行駛速度以及轉向，我們採用模糊控制技術來設計車體控制器，因系統除了具有像駕駛人之模式決策(Decision-making)，也模仿駕駛人之智能及行為，並展現可與駕駛人比擬之加速、剎車、以及轉向操控。另外，考慮到車輛縱向及橫向動態耦合(Coupling)之特性，我們發展一種具有三自由度之非線性車輛動態模型，設計一個整合縱向及橫向之控制器，並藉由 *CarSim* 模擬環境來驗證此控制演算法之可行性及實用性。

Longitudinal and Lateral Control Design for Vehicle Automated Driving

Student : Hsin-Han Chiang

Advisor(s): Dr. Bing-Fei Wu

Dr. Tsu-Tian Lee

Dr. Shinq-Jen Wu

Department of Electrical and Control Engineering

National Chiao Tung University

ABSTRACT

Vehicle automation is an important research topic of advanced vehicle systems (AVS). Taiwan *i*TS-1 is an experimental autonomous vehicle developed by National Chiao Tung University (NCTU). In this dissertation, a complete process of developing a multi-mode automated driving system is presented. This process consists of control objectives determination, system configuration design, vehicle dynamics modeling and validation, control algorithm development, and on-road testing. A hierarchical-control structure is proposed in the system to achieve the integrated longitudinal and lateral vehicle control. Upper-level control perceives road environment and determines the proper and safe operation modes including lane-keeping, lane-change, cruise control, adaptive cruise control, and stop-and-go. In each mode, the desired-velocity and reference-trajectory are primarily determined, and then are forwarded to vehicle-body control. To incorporate well driving tasks of human drivers into our system, vehicle-body control utilizes the fuzzy control technique to regulate the vehicle to adapt to the desired command (velocity and trajectory). In addition to the decision-making scheme, our system can mimic a human's intelligence and behavior to manage throttle, brake, and steering actuators in a driver-compatible way. Besides, to consider the coupling effects between the longitudinal and the lateral motion of a vehicle, a nonlinear three-degree-of-freedom vehicle dynamics is developed for a combined longitudinal and lateral vehicle controlling design. This controller is subsequently evaluated on a virtual vehicle in *CarSim* with remarkable results. The developed system has been verified repeatedly on highway and urban environments, respectively, with great success.

Acknowledgement

我非常感謝，也非常幸運地，我有三位指導教授—謹向我的指導教授 李祖添老師致上最感謝之意。感謝老師從碩士班開始的悉心指導，儘管博士班時期老師常在台北，但仍抽空回來與我們討論，且提供我們良好的研究環境。從老師的言行以及對學問的態度，影響我甚巨，心裡常記著老師勉勵我們：「要堅持，要認真，還有善良。」非常感謝指導教授 吳炳飛老師，在博士班的過程中，老師的積極研究態度與訓練要求深切的感染我，全方位對軟硬體技術以及理論的學問，更是我深感佩服及想學習的目標，永不忘老師的訓示：「一個人的態度決定一個人的高度。」此外，也向指導教授 吳幸珍老師致上最深的感謝，從碩士班到博士班，在理論方面指導我甚多，也經由不斷與老師討論，不斷激發我研究上的思考，也將謹記老師：「以研究來貢獻社會。」的自我期許。

感謝口試委員 鄧清政教授、姚立德教授、以及陳柏全教授，在口試時提出寶貴的意見，以及不同的思考方向與問題，使得論文內容能更臻完備。

感謝系上老師 廖德誠教授、鄭木火教授、邱一教授，在課程上的指導以及球場上的交流，讓我感覺亦師亦友的溫暖。

在博士班的過程中，也非常感謝彭昭暉學長，願意不斷地勉勵我以及分享豐富的人生觀，讓我對幸福的追求有不同的體認，更銘記學長的期勉：「存善心，為善事。」此外，也感謝實驗室文真學姐、保村學長、冠銘學長和炳榮，學弟忠潔與鎮南，一起度過實驗室共事的日子。

感謝 CSSP Lab 已畢業的學弟岑瑋、俊樺、嘉賢，我永不忘曾經一起沒日沒夜、跑遍快速道路 68 號作實驗的過程，感謝你們在硬體上的幫忙，才以使我的論文更加精彩。感謝學弟威儀、學妹依庭，在目前持續進行的研究上努力與幫忙。我很榮幸遇到你們這一群伙伴。

在此也要感謝陪我度過這一段求學過程的所有朋友們，我亦珍惜每一個過程與時光。最後，非常感謝我摯愛的家人，爺爺、奶奶、爸爸、媽媽和遠在美國的妹妹，你們的支持、照顧、容忍和深切的期盼是我完成學位的精神支柱，謹將這一份小小榮耀獻給你們。

Table of Content

Abstract in Chinese	i
Abstract in English	ii
Acknowledgement	iii
Contents	iv
List of Figures	vi
List of Tables	ix
Nomenclature	x
1. Introduction	1
1.1 Present Work Survey	1
1.2 Motivation	2
1.3 Major Contribution	4
1.4 Dissertation Overview	5
2. Vehicle Overview	6
2.1 Automated Vehicular Equipments	6
2.2 Automated Driving System Diagram	8
2.3 Function-flow	10
3. Lateral Control system Design	12
3.1 Vehicle Lateral Dynamics	12
3.2 Lane-keeping Control Design	16
3.2.1 Observer Design	19
3.2.2 Fuzzy Gain Scheduling	20
3.2.3 Analysis for the Lateral Controller with FGS	24
3.3 Lane-change Control Design	27
4. Longitudinal Control System Design	33
4.1 Modeling for Vehicle Longitudinal Dynamics	33

4.2	Longitudinal Automation System Design.....	37
4.2.1	Adaptive Horizontal Detection Area.....	38
4.2.2	Supervisory Control.....	42
4.2.3	Regulation Control.....	49
4.3	Collision Warning/Avoidance Maneuver.....	55
5.	Combined Longitudinal and Lateral Control Design.....	59
5.1	Nonlinear Vehicle Longitudinal and Lateral Coupling Dynamics.....	59
5.2	T-S Fuzzy Modeling for Nonlinear Vehicle Dynamics.....	63
5.3	Fuzzy Automated Driving Control Design.....	68
5.3.1	Fuzzy Controller Design.....	68
5.3.2	Fuzzy Observer Design.....	70
5.4	Numerical Simulations	73
6.	Experimental Results.....	78
6.1	Test-track Testing.....	78
6.2	Freeway/Highway Testing.....	81
6.3	Urban-road Testing.....	93
7.	Conclusions and Future Works.....	98
	References	100
	Appendix A.	105
	Appendix B.	107
	Appendix C.	108
	Vita	109
	Publication List	110



List of Figures

Fig. 2-1.	System architecture in the test-bed vehicle, Taiwan <i>i</i> TS-1.....	6
Fig. 2-2.	Two-level hierarchy of the proposed automated driving system.....	8
Fig. 2-3.	Structure of controller/vehicle system.....	9
Fig. 2-4.	Function-flow of the upper-level control.....	10
Fig. 3-1.	Bicycle model for front-steering vehicles.....	12
Fig. 3-2.	Exemplified cornering characteristics of front and rear tires. (Dotted line: high friction road, and dashed line: low friction road).....	14
Fig. 3-3.	The relation between the steering ratio and the average error of measurements.....	15
Fig. 3-4.	The states signal for verification between the model and the vehicle in the case $i_{sr}= 26$. (solid line: model; dashed line: vehicle).....	15
Fig. 3-5.	Vehicle lateral dynamics with respect to road geometry.....	16
Fig. 3-6.	Block diagram of the proposed auto-tuning lateral control system.....	21
Fig. 3-7.	The membership functions for (a) v_x , (b) y_{Ld} , and (c) Δ_{fg}	22
Fig. 3-8.	The performance of the proposed pure feedback and FGS-feedback as compared to curvature-feedforward approach in [16].....	23
Fig. 3-9.	Closed-loop performance for the normal condition and 10% variation in the cornering stiffness.....	24
Fig. 3-10.	Equivalent block diagram for the single-point previewed pursuit controller/vehicle system.....	25
Fig. 3-11.	Frequency response characteristics for our steering controller/vehicle system.....	26
Fig. 3-12.	Illustration of the lane-change maneuver.....	27
Fig. 3-13.	Time optimal lateral jerk reference signal in [41].....	28
Fig. 3-14.	Modified lateral jerk reference signal.....	29
Fig. 3-15(a).	Magnitude plot of front-wheel angel to yaw rate $H_{\gamma-\delta}(s)$	30
Fig. 3-15(b).	Velocity-dependent function $h_{\gamma-\delta}(v_x)$ at velocities from 5 to 30 m/s....	31
Fig. 4-1.	Nonlinear model of the vehicle longitudinal dynamics.....	33
Fig. 4-2.	Closed-loop configuration employed in the identification of ψ , q_1 , q_2 , and q_3	34

Fig. 4-3.	The averaged values of ψ , q_1 , q_2 , and q_3 , verses velocity of the vehicle.....	35
Fig. 4-4.	The I/O responses of the simulation model and its comparison with the real vehicle.....	36
Fig. 4-5.	Dual-loop structure of the longitudinal automation system.....	37
Fig. 4-6.	Illustration of the scenario of a vehicle following on curves.....	38
Fig. 4-7.	Derivation of the signed distance.....	49
Fig. 4-8.	Membership functions of (a) the fuzzy input and (b) the fuzzy output.....	51
Fig. 4-9.	Overall structure of the proposed regulation control structure.....	51
Fig. 4-10.	Constant velocity-tracking performance for (a) proposed PD-based FLC and (b) PID-based FLC.....	52
Fig. 4-11.	Control surface of the single-input fuzzy control.....	52
Fig. 4-12.	Headway distance for car-following.....	55
Fig. 4-13.	The relation between the TTC and the warning evaluate signal with respect to different velocities.....	57
Fig. 4-14.	Warning degree in three zones.....	58
Fig. 5-1.	3-DOF vehicle model.....	59
Fig. 5-2.	Global sector nonlinearity.....	63
Fig. 5-3.	Membership functions for z_1 , z_2 , and z_3	64
Fig. 5-4.	Animation window of Comparison 1.....	73
Fig. 5-5(a).	Lateral offset comparison of the proposed controller against the Autopia approach.....	74
Fig. 5-5(b).	Velocity comparison of the proposed controller against the Autopia approach.....	74
Fig. 5-6.	Animation window of Comparison 2.....	75
Fig. 5-7(a).	Trajectory comparison of the proposed controller against the MacAdam model with preview time 1 s.....	76
Fig. 5-7(b).	Velocity comparison of the proposed controller against the PI speed controller.....	76
Fig. 6-1(a).	The experimental results without FGS on the CDTT (straight lane with flat surface).....	79
Fig. 6-1(b).	The experimental results with FGS on the CDTT (straight lane with	

	flat surface).....	80
Fig. 6-1(c).	The experimental results with FGS on the NVHSTT (straight lane with irregular surface including single-side lane marking segment).....	80
Fig. 6-2.	The snapshot of the experiment on expressway.....	81
Fig. 6-3.	The sampled history of vehicle following experiments without adaptive HDA maneuver (Dashed line: reference signal; solid line: real signal).....	82
Fig. 6-4.	The sampled history of experiments involving the transition between CC and ACC mode (Dashed line: reference signal; solid line: real signal).....	83
Fig. 6-5.	Performance of ACC mode (fixed-distance-tracking) in a real traffic environment.....	84
Fig. 6-6.	Experimental results of CC mode switching to ACC mode.....	86
Fig. 6-7.	ACC mode operation with throttle and brake actuation.....	87
Fig. 6-8.	Performance of LK mode operation under real-traffic environment in Highway No. 3.....	88
Fig. 6-9.	LK mode operation under crucial curves in Expressway No. 68.....	89
Fig. 6-10.	Lane-marking detection in the lane-change scenario from the display of vision system.....	90
Fig. 6-11.	The transition between LK mode and turn-left LC mode.....	91
Fig. 6-12.	Turn-right LC mode operation with the velocity 70 km/h.....	91
Fig. 6-13(a).	Turn-right LC mode at 62 km/h with early-switch maneuver.....	92
Fig. 6-13(b).	Turn-left LC mode at 67 km/h with early-switch maneuver.....	92
Fig. 6-14.	The in-vehicle view for stop-and-go maneuver in the Nanliao Harbor Park. (a) Low speed CC mode; (b) Stop-and-go mode.....	93
Fig. 6-15.	Low speed CC mode switches to stop-and-go mode.....	94
Fig. 6-16.	Stop-and-go mode of the supreme 30 km/h.....	95
Fig. 6-17.	Experimental results of the vision-based lane-change maneuver.....	96
Fig. 6-18.	Experimental results of the GPS-guided lane-change maneuver.....	97
Fig. B-1.	Horizontal detection area.....	107

List of Tables

Table 3-1.	Rule Base of FGS.....	22
Table 3-2.	Crossover freq. of controller/vehicle system.....	26
Table 4-1.	(δ_{sw}, θ) with varying velocities and radiuses of curves.....	41
Table 4-2.	Comparative results between ISO 15622 and adaptive HDA.....	41
Table 4-3.	Rule table of the SFLLC.....	51
Table 5-1.	DLC performance with different preview distances.....	77
Table 6-1.	Testing conditions of different environmental sets.....	78
Table 6-2.	Performance of CC mode at different velocities.....	85
Table A.1	Specification of Taiwan <i>i</i> TS-1.....	105
Table A.2	List of equipments in Taiwan <i>i</i> TS-1.....	105
Table A.3	Nominal parameter values of the vehicle platform (Taiwan <i>i</i> TS-1).....	106



NOMENCLATURE

F_{yf}, F_{yr}	Lateral forces of front and rear tires, respectively.
C_f, C_r	Cornering stiffness of front and rear tires, respectively.
α_f, α_r	Slip angle of front and rear tires, respectively.
m	Mass of the vehicle.
I_z	Inertia moment around the center of gravity (CG) of vehicle.
a, b	Distance from front and rear tires to CG, respectively.
v_x	Longitudinal velocity in the CG of vehicle.
v_y	Lateral velocity in the CG of vehicle.
γ	Yaw rate in the CG of vehicle.
δ_{SW}	Steering wheel (SW) angle.
δ_f	Front-wheel angle of the vehicle.
i_{sr}	Steering ratio between the steering wheel and front wheel.
a_y	Lateral acceleration in the CG of vehicle.
L_d	Look-ahead distance for previewed navigation.
y_{Ld}	Lateral offset to the road centerline at a look-ahead distance L_d .
ε_{Ld}	Angle between the tangent to the road and the vehicle axis at a look-ahead distance L_d .
ρ_{Ld}	Road curvature at a look-ahead distance L_d .
\underline{x}	State vector of vehicle dynamics.
A, B, E	Vehicle linear model matrices.
K_{fb}	Full-state feedback control.
τ	Transport lag of controlling input.
I_n, I_m	Identity matrices with dimensions $n = 4$ and $m = 1$, respectively.
Δ_i	Tuning gain of the i -th fuzzy rule.
Δ_{fg}	Inferred gain of fuzzy gain scheduling (FGS).
μ_i	The i -th rule strength of FGS.
y_{cg}	Deviation of the vehicle's CG from the lane center.
y_{des}	Desired lane-width for lane-change maneuver.
A_{max}	Maximum admissible lateral acceleration.
J_{max}	Maximum admissible lateral jerk.
β	Side-slip angle of the vehicle's CG.

ϕ	Yaw angle with respect to the road.
a_f	Acceleration of the following vehicle.
a_{fmax}	Constraint of maximum acceleration.
a_p	Acceleration of the preceding vehicle.
d_R	Distance in the feasible range of forward-looking sensor (FLS).
D_s	Signed distance of FLC.
k_t	Damping gain.
L	Minimum distance or typical vehicle length.
R_f	Radius of the curved road.
R	Relative distance between the preceding and the following vehicles.
R_{des}	Desired distance between vehicles
R_i	Spacing error for the i th vehicle in a platoon.
S	Sliding manifold.
S_h	Switching line.
T_s	Sampling period in the control process.
u_i	Distinct value of the i -th rule output.
V_p	Forward velocity of the preceding vehicle.
V_f	Forward velocity of the following vehicle.
V_C	Commanded velocity of the following vehicle.
V_{des}	Driver-selected velocity for the following vehicle.
X_p	Position of the preceding vehicle.
X_f	Position of the following vehicle.
θ	Expanded angle in the adaptive detection area.
σ	Desired headway time (in seconds).
λ	Sliding surface gain.
α	Slope of the switching line.
L_{wb}	Length of wheelbase.
k_D	Drag coefficient from aerodynamics.
F_T	Net force of traction or braking exerted on the tires.
f	Rotating friction coefficient.
g	Acceleration of gravity.
k_L	Lift coefficient from aerodynamics.
ψ	Heading angle.

ψ_D	Desired heading angle with respect to the reference curvature of road.
ρ_r	Reference curvature of the road.
y_e	Distance from the road center to the sensor mounted at a distance d_s ahead of the vehicle's CG.



Chapter 1

Introduction

1.1. Present Work Survey

The development of automatic driving and highway automation provides an opportunity to relieve the driver from undesired routines of driving task. From the late 1980s, a number of research programs have been aiming to develop various advanced technologies for intelligent transportation systems (ITS) in the United States, Europe and Japan; especially for improving highway-capacity and driving-safety by automation in both highway-system and vehicle-level. This dissertation focuses on achieving automation in vehicle-level. An autonomous vehicle has to execute some or all driving tasks without external intervention. Therefore, intelligence is indispensable for such a vehicle to perform the required driving tasks.

Partners for Advanced Transit and Highways (PATH) program developed an infrastructure-based lane embedded with discrete magnetic markers so that automatic vehicles can circulate autonomously and form platoons [1, 2]. Moreover, in this program, Hessburg and Tomizuka propose a lateral-vehicle-guidance system based on fuzzy logic control (FLC) and successfully implemented it on a Toyota Celica vehicle [3]. The Navigation Laboratory (NavLab) at Carnegie Mellon University demonstrated automated steering control by artificial-vision and neural-network-based control techniques [4]. A navigation system for autonomous lane-keeping and lane-change on their test-bed vehicles (Honda Accord LX) was developed by a team in the Ohio State University (OSU) [5, 6][16]. Dickmanns' team at University of Bundeswehr in Germany developed an artificial-vision-based automatic driving system installed in a van with automated actuators. It can drive at speeds up to 130 km/h on highway [7, 8]. Alberto Broggi's team developed the ARGO vehicle at Parma University. ARGO executed an automatic artificial-vision-based steering mission over 2000 km on highway [9]. In AUTOPIA program two Citroen Berlingo vans, which are embedded with fuzzy-logic-based control system for mimicking human driving behavior, carried out driving and route-tracking tasks under urban-like environments [10-12]. Tsugawa's team in Japan demonstrated their intelligent vehicles with fully automatic driving on normal roads by global positioning system (GPS) and inter-vehicle communications [13, 14]. In China, the

vision-navigation-based intelligent vehicle (THMR-V) developed by Tsinghua University performed autonomous high-speed lane-keeping on a structured road [15].

1.2. Motivation

In general, an automated vehicle possesses two basic control tasks, namely longitudinal control and lateral control. Longitudinal involves speed control and inter-vehicle spacing control with consideration of comfort and safety. Lateral control keeps the vehicle in line with the road centerline and steers the vehicle to an adjacent lane while the good passenger comfort should be maintained.

Assistance in vehicle speed control and car-following is presently one of the most popular research topics throughout the automotive industry and in the field of intelligent transportation systems (ITS). In the view of improving the safety of occupants of the car by and relieving drivers of tedious tasks, cruise control (CC) systems are developed with the capacity of maintaining a driver-selected speed in the beginning. A much improved version, namely, adaptive cruise control (ACC) systems extend the car-following capability to CC systems. Furthermore, solutions for stop and go situations are now attracting much interest and also highly expected in the catalog of features. Although the procedures for controlling throttle and brake pedal can be based on complicated mathematical models, such a comprehensive longitudinal system of vehicle is very difficult to be linearized. The use of fuzzy logic can avert very complex approximate models which can not be computationally efficient.

Two fuzzy controllers for cruise control (CC) and adaptive cruise control (ACC) with stop-and-go maneuver have been demonstrated [10, 11] to be able to overcome the low-speed limitation in conventional ACC systems. However, no transition between CC, ACC, and stop-and-go is developed while encountering a preceding vehicle is required in order to do that. Moreover, the different fuzzy rules for CC and ACC will lead to the more complexity of tuning parameters in FLC. In this dissertation, we use stripe-partition instead of grid-partition for input space in our fuzzy speed control scheme. By doing so, the number of tuning parameters in FLC can be significantly reduced.

As to lateral control system, the issue of maintaining driver compatibility in a wide speed range is solved [17] by proposing a steering control that incorporates variable multiple look-ahead distances. Unfortunately, for the real-time vision system, the look-ahead distance can not be chosen too far because the lane-detection data becomes more erroneous due to

degradation of image resolution [18]. The curvature information at a look-ahead distance is additionally used to improve the steering performance [3][16, 17] while entering/existing curves. However, the correct curvature data is difficult to obtain in practice especially for vision-based approaches. To exhibit adaptive behavior in driver's steering tasks, a fuzzy gain scheduling (FGS) is proposed to adjust the steering effort by considering the lateral offset at a look-ahead and the instantaneous velocity of the vehicle. Consequently, the crossover model principle is employed to present that our closed-loop steering system provides a driver-compatible way.

Although the look-ahead sensor (such as vision system) replicate human driving behavior in measuring the lateral offset ahead of the vehicle, the road data can not be measured continuously during the transition from one lane to another. It is more difficult for lane-change when there is a so-called "dead-zone" period in which the preview information can not be available due to invalid lane-detection. In an attempt to handle this transition period of "open-loop" characteristics, a reliable time series steering angle command should be developed against adverse disturbances from vehicle-road interaction, uncertainties in vehicle parameters, and actuator nonlinearities.

As described in previous approaches, speed control and steering control are often considered as two separate control problems by assuming that longitudinal and lateral dynamics are independent. However, it is well know that the coupling effects become increasingly significant when the vehicle experiences higher lateral accelerations, larger tire forces, and adverse road conditions. Even though the solution is to merge the two control tasks into single, only a few works have been reported as yet. Sliding control and dynamic surface control methods are used to facilitate the inclusion of the complex, nonlinear coupling effects in the controller derivation [19]. Besides, a series of works have been proposed with nonlinear control techniques based on *Lyapunov* approach [20]-[22]. Recently, several remarkable works have shown the significant progress toward a coordinated longitudinal and lateral motion control of vehicles. A combined control of longitudinal and lateral motions using robust adaptive control by backstepping is proposed to control the unmatched nonlinear vehicle dynamics even under adverse driving conditions [23]. To compensate the inherent model discrepancies of the vehicle, an on-line adaptive neural module was implemented on top of a proportional plus derivative controller in synthesizing a neuroadaptive combined lateral and longitudinal control for highway vehicles in [24].

1.3. Major Contribution

The traffic on real highways remains complex and difficult to be managed such that different functions are required to be performed as well as vehicle control which is necessary to design the decision and the control for an automated vehicle from a safe viewpoint. Taiwan *i*TS-1 is the first intelligent vehicle developed by National Chiao Tung University (NCTU) in Taiwan [25]. In this dissertation, we propose a hierarchical-control autonomy structure to achieve integrated longitudinal and lateral control on highway and urban-road environments. The upper-level control analyzes the traffic situation and determines a driving mode among several developed modes, while the vehicle-body control executes the real-time control signal based on the determined driving mode. The good driving task depends on the well logical reasoning in underlying systems and dealing with uncertainty related to environment perception. Therefore, it motivates to integrate aspects of human intelligence and behaviors into the vehicle-body control so that driving actuators can be managed in a way similar to humans. Instead of using the mathematical representation of the systems, the behavior and experience of human drivers can be built into the system through fuzzy reasoning which is undeniably a useful feature for emulating the human reactions. Classical approaches frequently fail to yield appropriate models of complex processes, while fuzzy control technique provides an alternative tool for dealing with vehicle and its subsystem complexity. In this way, the controller at vehicle-body level has the same structure across different driving modes at upper-level; besides, the upper-level control is modular and extensible for accommodating to evolutionary modification by easily adding supplementary modes into the decision, and incorporating additional real-time information into the control.

Taiwan *i*TS-1 is embedded with heterogeneous systems including various sensors, core controller, interfacing, and mechanisms to carry out automatic driving. For lack of support from the vehicle industry, whole equipments including data-acquisition sensors, interfacing circuits, and motor-actuators are self-installed in the vehicle. The developed system on Taiwan *i*TS-1 has been verified through considerable experiments on test tracks and real highway environments. There are two indicators to access successful testing: a) safety means the system stability (or reliability) and robustness, and b) performance highlights the system consistency and passenger comfort. The designing procedure consists of control objectives determination, sensing system development, actuator design, vehicle dynamics validation, control algorithm design, system integration, and on-road testing. In other words,

development of a successful system demands not only technical understanding of the control problems, but also a sound knowledge of system engineering practice. Every element is crucial in a good mechatronic system design and therefore the success of the testing can be achieved.

In the later part of dissertation, a systematic design of the combined control of vehicle longitudinal and lateral motions for automated driving is presented. The nonlinear 3-degree-of-freedom (3-DOF) dynamic model with the parameters of real vehicle is used. This approach firstly derives the T-S fuzzy model in accordance with the complex nonlinearities and input-coupling characteristics of vehicle dynamics. And then, we can design the fuzzy speed and steering controller such that the vehicle system can be in pursuit of the reference states (i.e., desired vehicle velocity and lateral offset to the road centerline). This controller drives the vehicle to be in line with the desired targets with the assurance of minimum energy consumption [26, 27]. Only the small angle approximation is used. The resulting controlling can be directly solved to obtain the real control inputs of vehicle. The control approach facilitates the inclusion of the complex and nonlinear coupling effects in the controller design. Eventually the proposed scheme is validated and the improved controller performance is demonstrated in the environment of *CarSim* [28], a general software tool to simulate the dynamic behavior of a road vehicle.

1.4. Dissertation Overview

The rest of this dissertation is organized as follows. Chapter 2 describes the overview of our vehicle platform, namely Taiwan *iTS-1*. The design of the lateral control system with lane-keeping and lane-change control are presented in Chapter 3. In Chapter 4, the modeling of vehicle longitudinal dynamics and the longitudinal control system design with CC, ACC, and stop-and-go are presented. Besides, the developed collision avoidance/warning scheme is also introduced. In Chapter 5, fuzzy modeling for a nonlinear 3-DOF vehicle dynamics is described and the combined longitudinal and lateral control is achieved by utilization of optimal fuzzy control design. Experimental results under real traffic environment are presented in Chapter 6 to demonstrate the system's validness. Finally, conclusions are included in Chapter 7.

Chapter 2

Vehicle Overview

2.1. Automated Vehicular System

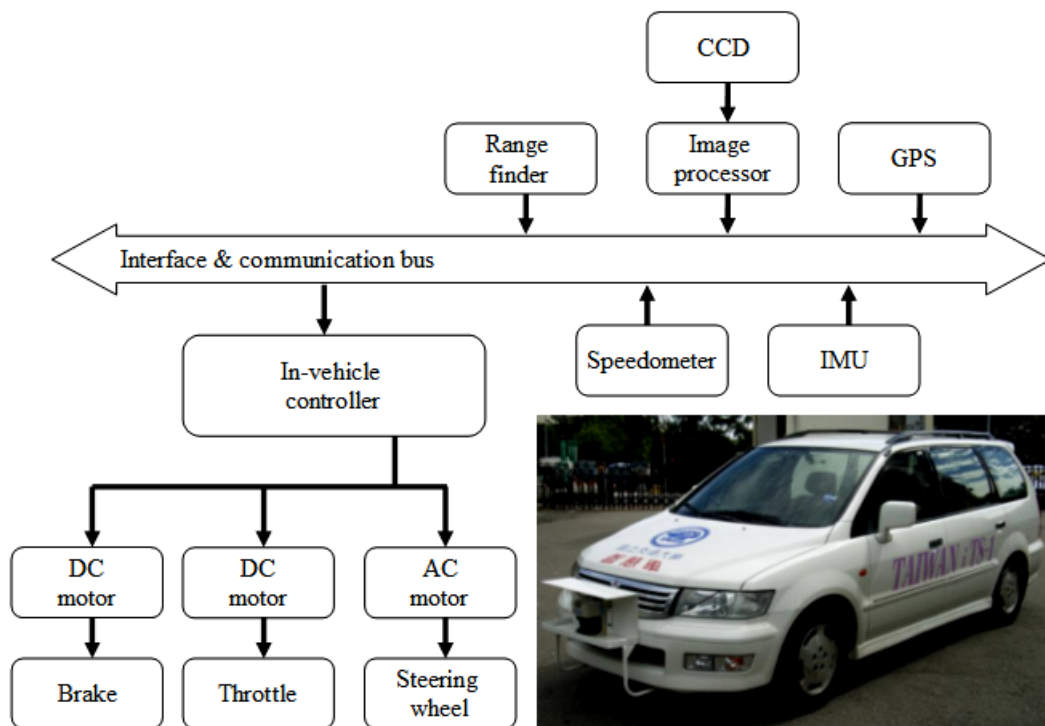


Fig. 2-1. System architecture of the test-bed vehicle, Taiwan *iTS-1*.

As shown in Fig. 2-1, Taiwan *iTS-1* (a prototype of Mitsubishi Savrin wagon) is equipped with a throttle, a brake, and a steering-wheel (SW) actuating system. Two internal state sensors, namely the speedometer and an inertia measurements unit (IMU), are used to sense the vehicle's velocity, acceleration and angular rate, respectively. Besides, the utilized primary sensors include a real-time kinematical differential GPS (RTK-DGPS), an image processor with a monochromatic CCD camera, and a laser range finder. Initially, the in-vehicle controller is developed in a dSPACE Microautobox (MABX), a real-time hardware with a rapid prototype for control design and verification [29]. At present, the in-vehicle controller is successfully realized by a DSP-based stand-alone board [30, 31]. The in-vehicle controller communicates with various sensors through an interface board, and can be

reprogrammed onboard with data analysis and calibration via a notebook. Through environmental perception from primary sensors, the in-vehicle controller runs the driving control algorithm and sends throttle, brake, and SW controlling commands to actuating motors to achieve vehicle longitudinal and lateral control.

An AC servomotor is installed in the SW column to enable automatic steering. The angle of SW is measured by a steering angle sensor which is set around the axis of SW. Both the vision system [18, 32] and RTK-DGPS can provide lateral information such as the deviation from the centerline and the orientation with respect to a reference trajectory. The vision system is a look-ahead sensor while RTK-DGPS is a look-down sensor, and the fundamental difference between these two sensors is the difference in the range of the lateral information. The vision detects the lane-markings ahead of the subject-vehicle, and provides the look-ahead relative positions of the vehicle with respect to the lane center. Based on RTK-DGPS, the relative position data are compared with a digital map on which the target route has been previously specified to be tracked.

As for longitudinal control, a throttle valve is driven by a mounted DC servomotor avoiding any change to vehicle's internal-components. A throttle position sensor (TPS) is composed of an A/D converter encoding an analog voltage into a normalized digital signal [33]. The brake pedal is automated by using a DC servomotor which is connected to a braided steel cable via an electromagnet. Its position is measured in terms of voltage variation output from a linear position transducer [30]. The main sensor for longitudinal control is the range finder which provides the current headway distance between the subject-vehicle and a preceding-vehicle in the same lane.

The specification of Taiwan iTS-1 and the utilized sensors, signal processors, and actuators are given in Appendix A.

2.2. Automated Driving System Diagram

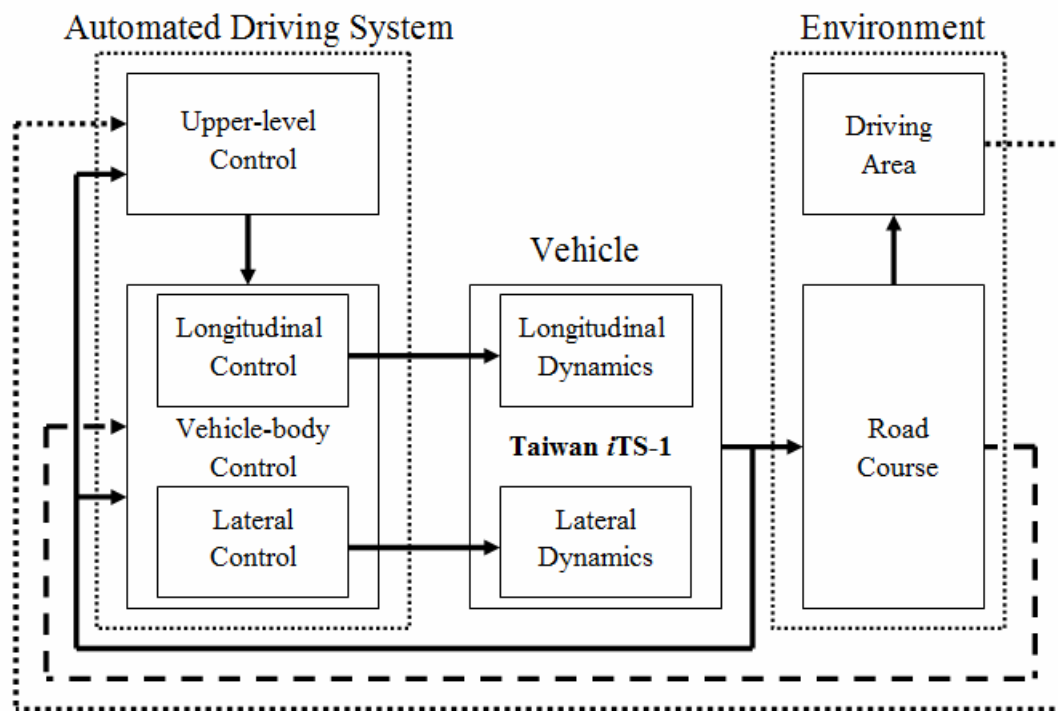


Fig. 2-2. Two-level hierarchy of the proposed automated driving system.

We use a two-level hierarchical architecture as shown in Fig. 2-2 to achieve automated driving or driver assistance in a highway/freeway and urban-road environment. Mimicking human driver observing the traffic situation and the course of the road, the upper-level control determines the driving modes, namely lane-keeping (LK), lane-change (LC), cruise control (CC), adaptive cruise control (ACC), and stop-and-go. This level is concerned with ensuring that the system fits the suitable driving to the existing road-condition and the traffic. After determination of driving mode, the upper-level control then provides the vehicle-body control with the reference velocity (for CC, ACC, and stop-and-go) and the reference trajectory (for LK and LC).

The vehicle-body control is the lowest level in the hierarchy, but has the highest priority at the same time because of the task of transforming the desired variables into suitable control values. As comparing sensory information to these reference data, vehicle-body control will generate SW-, throttle-, and brake-control commands to motor drivers. In addition to stability requirement, the vehicle-body control must handle uncertainties in vehicle subsystems such as engine, driveline and brake, and compensate for disturbances such as tire-road adhesion or changes in gradients. Another important factor is the transmission latency in transmitting data.

There are two major delays which come from (a) the sensor processing time such as image processing of the vision system and scanning period of the laser range finder, and (b) the actuation of servo motor. Since these delays are quite substantial, this factor have been explicitly considered into the upper-level control or the vehicle-body control design which depends on our designing approach.

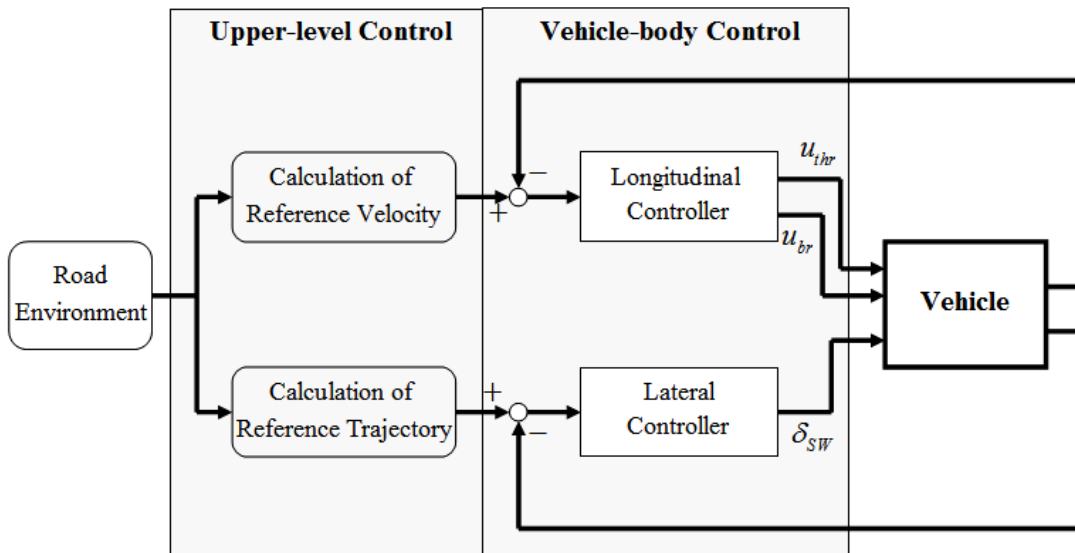


Fig. 2-3. Structure of controller/vehicle system.

The two levels can be described with “controller/vehicle” system, as illustrated in Fig. 2-3. In this figure, a division into longitudinal and lateral control is made. The upper-level control requires good knowledge about road-environment, while the vehicle-body control focuses on providing driver-comparable control behavior in carrying out the control of throttle pedal, brake pedal, and SW angle. The upper-level control is responsible for calculating the reference values of velocity (for CC, ACC, and stop-and-go) and trajectory (for LK and LC) for the longitudinal controller and lateral controller, respectively. The reference velocity changes frequently and is rather dependent upon the road traffic. The objective for the longitudinal controller is to keep the reference velocity as exactly as possible. The general task for the lateral controller is to keep the lateral error to zero, i.e., the reference trajectory is the centerline of the road. While LC mode is activated, the reference trajectory will be previously calculated in terms of desired values of lateral offset such that the vehicle can be steered from the current lane to an adjacent lane. It should be noted that either the upper-level control or the vehicle-body control is designed to be adaptive with vehicle states such as current velocity, real-time lateral error, and headway distance. In practice human drivers also

perform several driving tasks which are adaptive to these vehicle states.

By receiving the throttle-, brake-position, and SW-angle commands from the vehicle-body control, a proportional-integrate-differential (PID) controller is used to manage the AC-motor attached to the SW column to reach the target position for LK and LC mode, and another two PID controllers are used to drive DC-motors to adjust the throttle degree and the brake position for executing CC, ACC, and stop-and-go mode. This architecture, based on the cascade-control paradigm [34], is particularly useful to get over time-delay from controlling signals to action signals: rapid control can be achieved by intermediate signals which will provide faster response than the control signals.

2.3. Function-flow

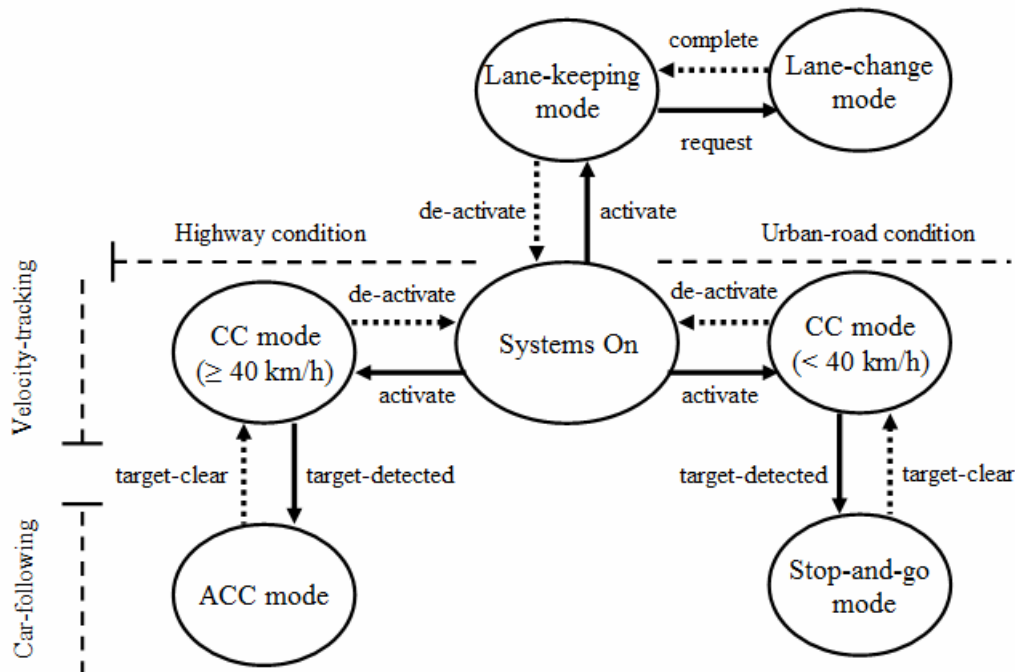


Fig. 2-4. Function-flow of the upper-level control.

In Fig. 2-4, the function-flow between LK, LC, CC, ACC, and stop-and-go mode in the upper-level control is presented. This system will initially activate LK mode or CC mode, or both simultaneously according to on-line detected traffic condition. In LK mode, the system retrieves real-time sensory information, calculates the deviation from a reference trajectory, and then generates a SW-control command. In CC mode, the subject-vehicle tracks a desired velocity profile set up by a human driver or the limited highway-velocity. As the vehicle

velocity is more than 40 km/h, the control scenario in ACC mode includes both safety-distance and fixed-distance tracking control. The former operation guarantees the safety-spacing keeping from the vehicle ahead while the later operation keeps a constant inter-vehicle spacing for the purpose of increasing the capacity of traffic flow. As a new event is detected, switching from CC mode to ACC mode is automatically activated. The system is defaulted in CC mode for clearance at road-ahead, and switches to ACC mode as a valid-target is detected. A valid-target is defined to satisfy the following conditions:

(a) it is in a designated range which is well defined to the feasible field of the utilized laser range finder;

(b) the velocity of a valid-target is slower than that of the subject-vehicle.

In ACC mode, the safety-distance is derived from constant headway-time policy. The value of fixed-distance can be set according to roadway control [35]. While the vehicle is driven under the velocity 40 km/h, it is reasonably to be assumed that the subject-vehicle is moving in an urban environment or a situation of heavy traffic such that stop-and-go mode will be activated if a valid-target is detected ahead. The preceding-vehicle might come to a complete stop owing to a traffic jam or a stop light. The modes-selection logic scheme is constructed in the upper-level control. The desired reference velocity in each mode will be filtered out, and then passed onto the vehicle-body control.

While the request of LC mode is given by the driver, the system steers the subject-vehicle from the current lane to an adjacent lane. The autonomous changing lane for overtaking a slower vehicle or an obstacle will be further developed in our system. Two schemes of lane-change maneuvers (GPS-guided lane-change and free lane-change) using RTK-DGPS and the vision system, respectively, are developed in our system. In the GPS-guided lane-change scenario, the reference trajectory calculated in the upper-level control is directly added on the lateral position of a specified route on the GPS map. This scheme guarantees the reference path-tracking stability issue, but limits the lane-change maneuver to specific locations where the map must be obtained beforehand. In the free lane-change scenario, the reference trajectory is transformed into the reference steering command that causes the subject-vehicle to track that reference. Without requiring the map information, however, the major difficulty in the free lane-change scenario is the extreme sensitivity of the system performance with respect to sensor noises and parameters variations in vehicle/road model.

Chapter 3

Lateral Control System Design

3.1. Vehicle Lateral Dynamics

In this chapter, the model for vehicle lateral dynamics is introduced to design the lane-keeping and lane-change control. As stated in [16, 32][36], the longitudinal and the lateral dynamics can be separated if the moving velocity does not vary too much. If roll movement is neglected, the vehicle lateral dynamics can be well represented by the so-called “bicycle model”. The bicycle model which dominates the lateral and yaw dynamics is useful in designing the steering controller to stabilize the vehicle keeping within the lane. As shown in Fig. 3-1, the bicycle model couples two front and two rear wheels together by assuming that the vehicle body is symmetric about the longitudinal plane, and the roll and pitch motion of vehicle are neglected.

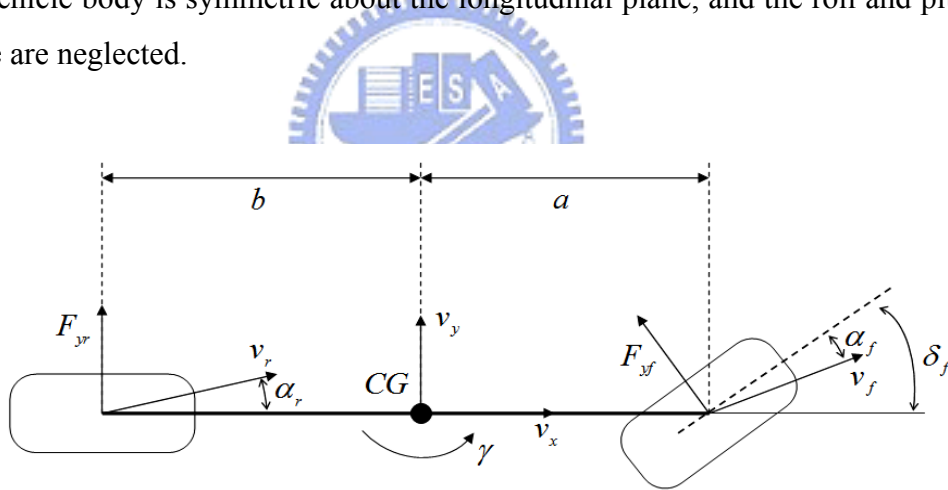


Fig. 3-1. Bicycle model for front-steering vehicles.

From Newton’s law, the net lateral forces and the net torque at the center of gravity (CG) of the vehicle can be obtained as

$$m(\dot{v}_y + v_x \cdot \gamma) = F_{yf} \cos \delta_f + F_{yr} \quad (3-1)$$

$$I_z \dot{\gamma} = F_{yf} \cdot a + F_{yr} \cdot b \quad (3-2)$$

Based on the assumption of the small steering angle ($\cos \delta_f \approx 1$) and the linear tire model, the lateral force of tire can be taken as linear proportional to the slip angle with a constant proportionality called cornering stiffness as

$$\begin{cases} F_{yf} = C_f \alpha_f \\ F_{yr} = C_r \alpha_r \end{cases} \quad (3-3)$$

The cornering stiffness of front and rear tire $C_{f,r}$ considered here is the slope of side force characteristics at the origin on a normal road condition. The slip angles α_f and α_r can be approximated as the functions of the vehicle's kinematic parameters

$$\begin{aligned} \alpha_f &= \delta_f - \frac{a\gamma + v_y}{v_x} \\ \alpha_r &= \frac{b\gamma - v_y}{v_x} \end{aligned} \quad (3-4)$$

The state equation of bicycle model can be rewritten in the following

$$\begin{bmatrix} \dot{v}_y \\ \dot{\gamma} \end{bmatrix} = \begin{bmatrix} a_1 & a_2 \\ a_3 & a_4 \end{bmatrix} \begin{bmatrix} v_y \\ \gamma \end{bmatrix} + \begin{bmatrix} b_1 \\ b_2 \end{bmatrix} \delta_f \quad (3-5)$$

where

$$a_1 = -\frac{C_f + C_r}{Mv_x}, \quad a_2 = \frac{bC_r - aC_f}{Mv_x} - v_x,$$

$$a_3 = \frac{bC_r - aC_f}{I_z v_x}, \quad a_4 = \frac{b^2 C_r - a^2 C_f}{I_z v_x},$$

$$b_1 = \frac{C_f}{M}, \quad b_2 = \frac{aC_f}{I_z}$$

Remark: In (3-1)-(3-5), the linear tire model is used by taking the cornering stiffness $C_{f,r}$ to be constant. In reality, it is found that the lateral tire force will initially increase with tire slip angle, and then saturate for a given tire/road friction condition [55-57], as shown in Fig. 3-2. To capture the saturation property of lateral tire/road friction, several nonlinear tire models were proposed. Bakker and Pacejka proposed a famous “magic formula” which represents that the lateral tire force not only depends on its slip angle but also on vehicle side slip angle $\alpha_{f,r}$, steering angle δ_f , and yaw rate γ . Without assuming small angles, the stability condition and bifurcation phenomenon with varying cornering stiffness and different velocities are presented in our previous work [57]. Besides, the front-wheel steering vehicle will become unstable due to the existence of saddle-node bifurcation which is derived in [57] and heavily depends on the rear-tire cornering force characteristics [55].

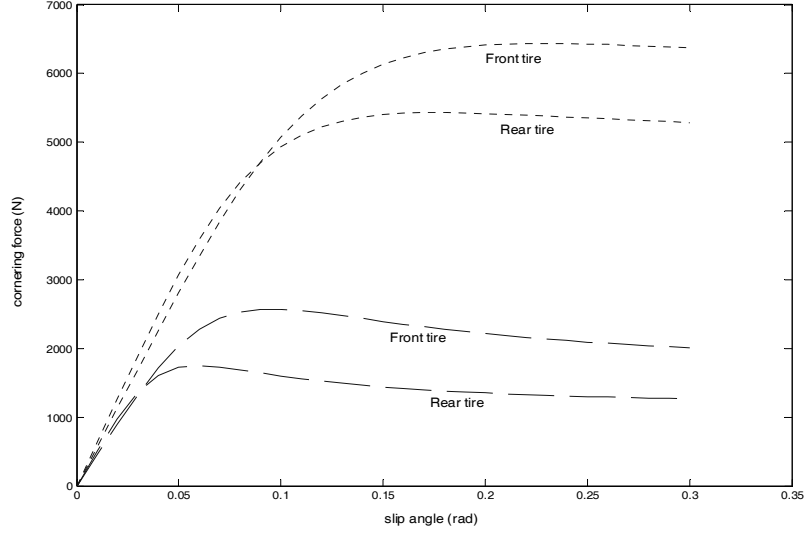


Fig. 3-2. Exemplified cornering characteristics of front and rear tires. (Dotted line: high friction road, and dashed line: low friction road)

To validate the bicycle model with the real vehicle dynamics is critical to obtain precise tracking results of steering control. The bicycle model in (3-5) varies with the vehicle speed v_x . Notably, the actual input to our vehicle platform is the SW angle δ_{SW} rather than the front-wheel angle δ_f . According to vehicular steering mechanics [37], the SW angle can be expressed as a product of the steering ratio i_{sr} and the front-wheel angle δ_f

$$\delta_{SW} = i_{sr} \cdot \delta_f \quad (3-6)$$

Because the compliance and steering torque gradients vary with increasing steering angles and load on the front tires, tire pressure, coefficient of friction, etc, in general, i_{sr} is not a fixed value for the power steering of the vehicle. However, the constant ratio can be practically used for control design. The steering ratio i_{sr} can then be adjusted slightly to yield a response that is more similar to that of the real vehicle platform. The measured SW angle was used as the input to the model. Besides yaw rate, the predicted lateral acceleration from the model can be approximately calculated by

$$a_y \cong v_x \cdot \gamma - \dot{v}_y \quad (3-7)$$

The average errors between the measurements and the model with respect to i_{sr} are illustrated in Fig. 3-3, and the minimum point is in the case of $i_{sr} = 26$. Figure 3-4 compares experimental results with the bicycle model predictions for a transient maneuver at around 60 km/h. The lateral acceleration of model agrees with the obtained experimental data in Fig. 3-4(a), and the predicted yaw rate of the vehicle also shows consistent correlation with the

experimental results in Fig. 3-4(b). Several other quantities were also measured and compared with the bicycle model. Results show that the bicycle model (3-5) can faithfully represent the lateral dynamics of the vehicle platform (Taiwan *i*TS-1).

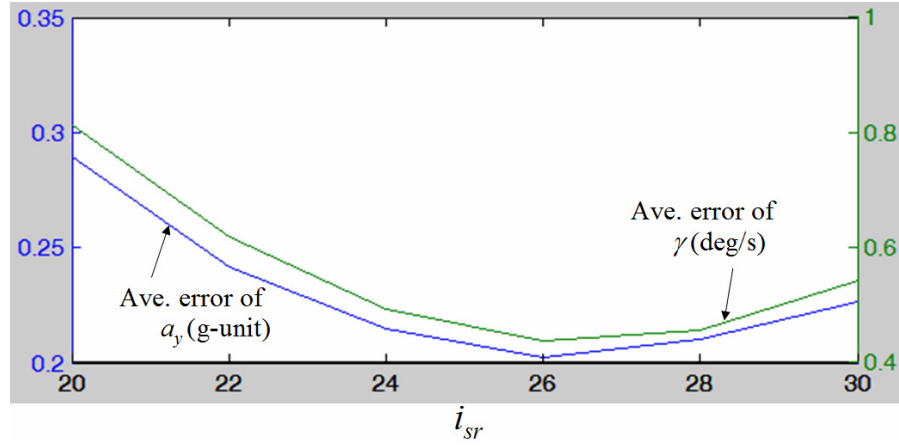


Fig. 3-3. The relation between the steering ratio and the average error of measurements.

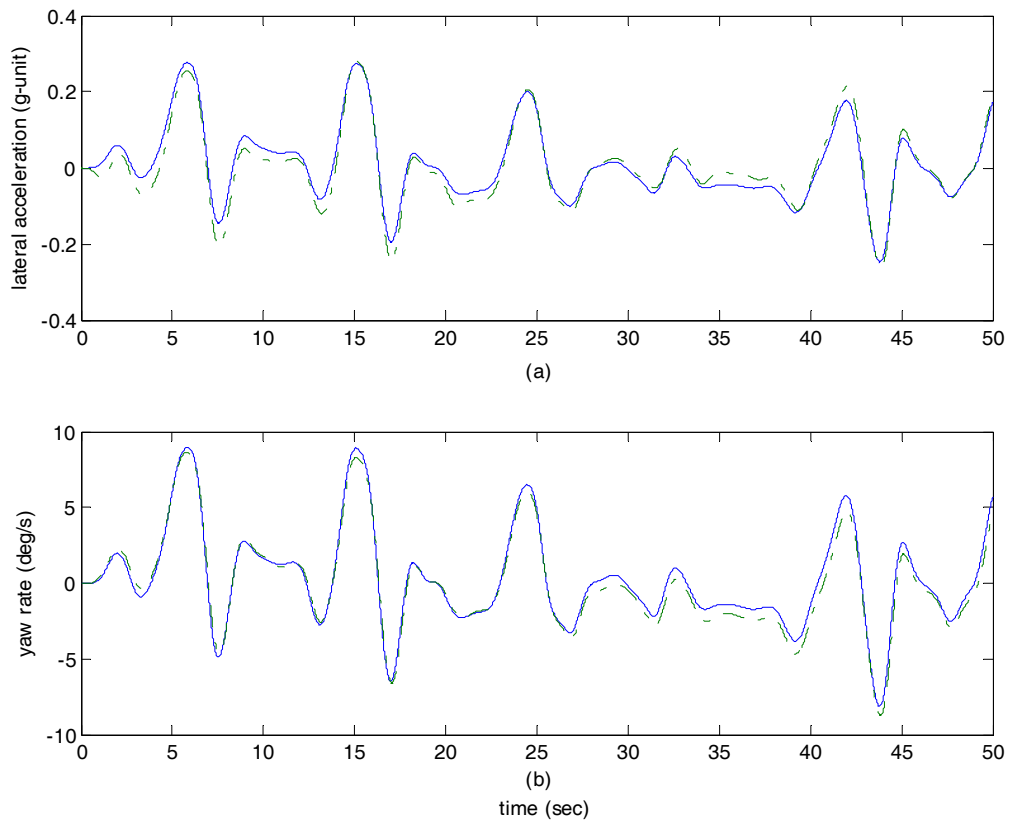


Fig. 3-4. The states signal for verification between the model and the vehicle in the case of $i_{sr} = 26$. (solid line: model output; dashed line: measured)

3.2. Lane-keeping Control Design

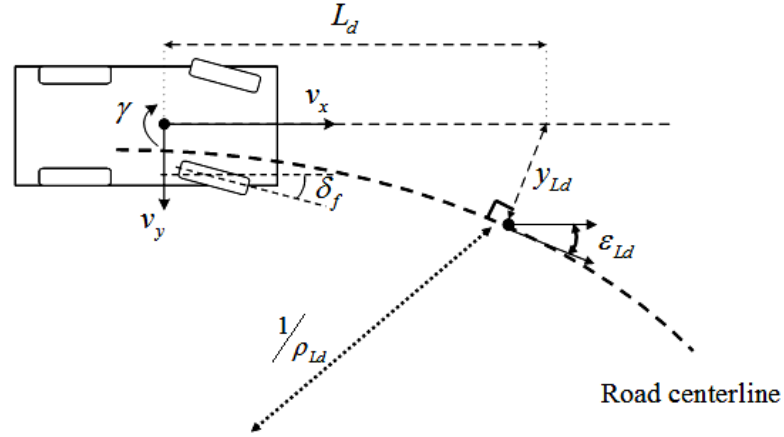


Fig. 3-5. Vehicle lateral dynamics with respect to road geometry.

The relationship between the lateral dynamics of the vehicle and the desired previewed navigation at a look-ahead distance L_d is plotted in Fig. 3-5. The valid amount of L_d is determined from the vision system [18, 32]. The previewed dynamics can be described as

$$\dot{y}_{Ld} = v_y + L_d \cdot \dot{\gamma} + v_x \cdot \epsilon_{Ld} \quad (3-8)$$

$$\dot{\epsilon}_{Ld} = \dot{\gamma} - v_x \cdot \rho_{Ld} \quad (3-9)$$

where the parameters have been defined in Nomenclature.

The bicycle model (3-5) is combined with the previewed dynamics (3-8) and (3-9) to form a linear state-space equation

$$\dot{\underline{x}} = A\underline{x} + Bu + E\rho_{Ld} \quad (3-10)$$

$$\text{with } A = \begin{bmatrix} a_1 & a_2 & 0 & 0 \\ a_3 & a_4 & 0 & 0 \\ 1 & L_d & 0 & v_x \\ 0 & 1 & 0 & 0 \end{bmatrix}, \quad B = \begin{bmatrix} b_1 \\ b_2 \\ 0 \\ 0 \end{bmatrix}, \quad E = \begin{bmatrix} 0 \\ 0 \\ 0 \\ -v_x \end{bmatrix}$$

where the state vector $\underline{x} = [v_y, \gamma, y_{Ld}, \epsilon_{Ld}]^T$, the control input $u = \delta_f$, and the previewed road curvature ρ_{Ld} is viewed as an exogenous disturbance of the system.

The linear system in (3-10) is parameterized with the longitudinal vehicle speed v_x . As v_x increases, the poles of the system move toward the imaginary axis, reducing the stability. Notably, changing the look-ahead distance L_d does not affect the poles location in the transfer function from δ_f to the previewed lateral offset y_{Ld} . If L_d is regarded as being close to the front of the vehicle, then the damping of the zeros in system (3-10) declines drastically and a

high-gain controller drives the closed-loop poles toward the zeros, resulting in a poorly damped closed-loop system. However, L_d can not be chosen too distant from the reliable field of the vision system. The image resolution at far look-ahead distance will be degraded such that collected data includes more errors. As the result of numerous experimental verifications, the reliable value of L_d is chosen as 10 ~ 15 m according to the developed vision system [18].

The control objective for vehicle lane-keeping is to regulate the offset at the look-ahead y_{Ld} to zero. Moreover, the controller is well anticipated to ensure that the vehicle lateral acceleration does not exceed $0.4g$ (g is 9.8 m/s^2) during the control process, such that smooth responses and the comfort of the passengers can be achieved. Given the vehicle model as (3-10), the state feedback control seems to be naturally applied with $u = -K_{fb} \underline{x}$ where $K_{fb} = [k_{v_y} \quad k_{\gamma} \quad k_{y_{Ld}} \quad k_{e_{Ld}}]$. Here the pole-placement design approach is adopted to consider that the control effort required is related to how far the open-loop poles are moved by the feedback. The objective of pole-placement aims to fix specifically the undesirable aspects of the open-loop response, and avoids either large increases in bandwidth or efforts while poles are moved [38]. Moreover, it typically allows smaller gains and thus smaller control efforts by moving poles that are near zeros rather than arbitrarily assigning all the poles. The closed-loop poles for the system with high order (>2) can be chosen as a desired pair of dominant second-order poles with the rest poles which correspond to sufficiently damped modes, so that the system will mimic a second-order response with the reasonable balance between system errors and control effort. The closed-loop bandwidth for the look-ahead lateral offset is chosen at 5.35 rad/s to mimic human responses [16]. As for comfort requirement, the corresponding closed-loop poles are chosen to ensure that the lateral acceleration above 0.5 Hz will not be amplified during the steering path. Besides, the pole-selection can also be specified by the bandwidth requirement with regard to the transfer function $y_{Ld}(s)/\rho_{Ld}(s)$ with the maximal allowable y_{Ld} to reasonable step changes of ρ_{Ld} [3-6]. From the computer simulations for the closed-loop system response with the step change in curvature, it is found that the complex poles with a damping ratio $\zeta = 0.707$ will meet the constraint of lateral acceleration. Therefore, the natural frequency ω_n of the prototype second-order system can be determined by [39]

$$\text{BW} = \omega_n \left[(1 - 2\zeta^2) + \sqrt{4\zeta^4 - 4\zeta^2 + 2} \right]^{1/2}, \quad (3-11)$$

and then we have the conjugate dominant poles as $s_{1,2} = -3.58 \pm 3.58j$. The other two poles are chosen as those in the original system. Notably, increasing the speed will reduce the stability

of the closed-loop system since the poles move close to the imaginary axis.

Recall the system matrix A in (3-10) is time-varying with the longitudinal vehicle velocity v_x . The feedback control is supposed to be designed under the highest speed of interest such that the stability for lower velocities can be guaranteed by applying the convex nature of the lateral vehicle dynamics. The following proposition summarizes this approach of using full state feedback control design.

Proposition 1: If a constant feedback control K_{fb} is chosen such that

$$A_{CL\min}^T P + PA_{CL\min} < 0 \quad (3-12a)$$

and

$$A_{CL\max}^T P + PA_{CL\max} < 0 \quad (3-12b)$$

where

$$\begin{aligned} A_{CL\min} &= A(v_{x\min}) - BK_{fb} \\ A_{CL\max} &= A(v_{x\max}) - BK_{fb} \end{aligned}$$

for a matrix $P > 0$, than the closed-loop system is stable for varying velocities of the range $v_{x\min} \leq v_x \leq v_{x\max}$.

Proof:

The closed-loop matrix at a velocity v_x can be represented as a convex combination of $A_{CL}(v_{x\min})$ and $A_{CL}(v_{x\max})$, namely

$$\begin{aligned} A_{CL}(v_x) &= A(v_x) - BK_{fb} \\ &= \mu A_{CL\min} + (1 - \mu) A_{CL\max} \end{aligned}$$

where μ is a parameter whose values depend on the vehicle velocity v_x and at the range $0 \leq \mu(v_x) \leq 1$.

By choosing Lyapunov candidate as $V = x^T P x$, we can obtain its derivative as

$$\begin{aligned} \dot{V} &= \dot{x}^T P x + x^T P \dot{x} \\ &= x^T (A_{CL}^T(v_x) P + P A_{CL}(v_x)) x \\ &= \mu x^T (A_{CL\min}^T P + P A_{CL\min}) x + (1 - \mu) x^T (A_{CL\max}^T P + P A_{CL\max}) x \\ &< 0 \end{aligned}$$

The proof is complete.

Furthermore, the transport lag is also emphasized in the lateral controller design. The transport lag is caused by the SW motor which arises while the desired command is sent to force the actuator, and also includes image processing delay. The further phase lags are added over the range of frequencies, and severely destabilizing the overall system. Thus a

pure transport lag element $e^{-s\tau}$ is included into the designed lateral controller. The input can be described as $u = e^{-s\tau}u^0$ with $u^0 = -K_{fb}\underline{x}$. By using the approximation of first-order Pade polynomial,

$$e^{-s\tau} \cong \frac{1 - \tau s/2}{1 + \tau s/2} \quad (3-13)$$

and the input becomes

$$\begin{aligned} \dot{u} &= \frac{2}{\tau}(u^0 - u) - \dot{u}^0 \\ &= \frac{2}{\tau}(u^0 - u) + K_{fb}(Ax + Bu + E\rho_{Ld}) \\ &= K_{fb}\left(A - \frac{2}{\tau}I_n\right)x + \left(K_{fb}B - \frac{2}{\tau}I_m\right)u + K_{fb}E\rho_{Ld} \end{aligned} \quad (3-14)$$

By combining the system (3-10) with (3-14), we obtain the augmented system:

$$\begin{bmatrix} \dot{x} \\ \dot{u} \end{bmatrix} = \begin{bmatrix} A & B \\ K_{fb}\left(A - \frac{2}{\tau}I_n\right) & \left(K_{fb}B - \frac{2}{\tau}I_m\right) \end{bmatrix} \begin{bmatrix} x \\ u \end{bmatrix} + \begin{bmatrix} E \\ K_{fb}E \end{bmatrix} \rho_{Ld} \quad (3-15)$$

The stability of the transport-lagged system is determined by the characteristic roots of the system matrix in (3-15); consequently, the feedback controller K_{fb} is designed to guarantee the stability of the closed-loop system (3-15) with a transport lag at the highest velocity (145 km/h in our system).

Remark 1: Due to the presence of nonzero term ρ_{Ld} , the states in (3-15) will not all converge to zero when the vehicle is traveling on a curve even through the closed-loop matrix A_{CL} is asymptotically stable.

Remark 2: The transport lag comes from the transmission delay in two latencies: 0.04 s for the complete processing of the vision system and measurements available to the controller, and 0.52 s for the average duration gathered by the step response and sine wave tracking between the command and the reaction of servo motor. We choose the transport lag 0.6 s in stable controller design.

3.2.1. Observer Design

Based on the state space model of vehicle lateral dynamics, the full-state feedback control strategy, i.e., all the states must be measurable, is applied in the previous section. However, it is difficult to measure the lateral velocity v_y of vehicles directly from general available sensors. In addition, it is not expected for rapid response in control due to the sensor noise in high

frequency. Thus, the observer design is naturally adopted for the lateral control system.

By considering the system (3-10) again and feeding back the error between the measured and estimated outputs, the equation for the observer scheme can be described as

$$\dot{\hat{x}} = A(v_x)\hat{x} + Bu + L_o(y - C\hat{x}) \quad (3-16)$$

$$y = Cx \quad (3-17)$$

with

$$C = \begin{bmatrix} 0 & 1 & 0 & 0 \\ 0 & 0 & 1 & 0 \\ 0 & 0 & 0 & 1 \end{bmatrix}$$

where \hat{x} denotes the estimated states.

The measurements in previewed lateral offset y_{Ld} and angle ε_{Ld} can be obtained from the real-time vision system [18], while the yaw rate γ can be provided from optic gyro.

The observer gain matrix $L_o \in \mathfrak{R}^{4 \times 3}$ is chosen to achieve satisfactory error characteristics in a number of ways. Here, the pole-placement technique is adopted for the pole-selection convenience of feedback control. As with the control design, the best estimator design keeps the balance between good transient response and low-enough bandwidth such that sensor noise does not significantly impair actuator [38]. Hence, the observer pole locations are selected to be slower than two times the controller poles, and this yields the overall system with lower bandwidth and more noise reduction.

3.2.2. Fuzzy Gain Scheduling

Although the static feedback control strategy suffices to meet the requirements of vehicle lateral control, it is sensitive to the parameters of the system, such as vehicle mass, cornering stiffness, and road curvature, and thus solid reflected by feedback signals. The desire to steer the vehicle in a more human fashion and to provide a smooth automated steering control process, motivates the adoption of a fuzzy inference scheme as part of the lateral controller designing strategy. Based on fuzzy set theory, an adaptation scheme using fuzzy gain scheduling (FGS) is proposed to improve the lateral controller of the vehicle.

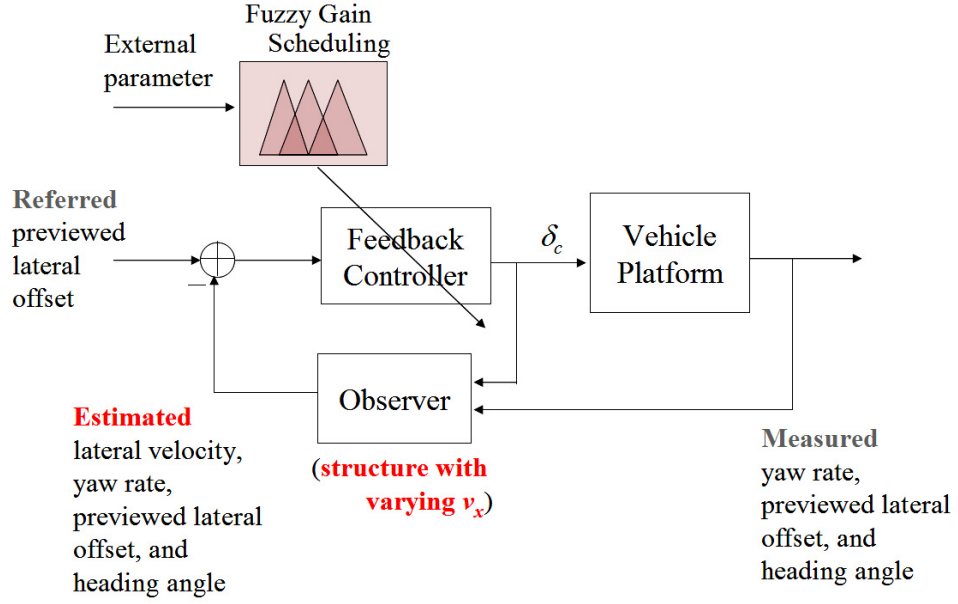


Fig. 3-6. Block diagram of the proposed auto-tuning lateral control system.

As presented in Fig. 3-6, FGS is designed to auto-tune the lateral controller. The kernel of the proposed FGS is the inference rule base, which constitutes a natural environment in which engineering judgment and human knowledge can be applied to the vehicle steering controller. FGS supports more human-like driving behavior during the process of keeping to the lane. The system mimics humans' driving more aggressively at low speeds, and more gently at high speed, even when the deviation between the vehicle and the centerline of the road is large. Accordingly, the linguistic input variables are the immediate velocity of the vehicle and the lateral offset from the centerline at the look-ahead distance. FGS yields the proper tuning gain, based on the following rules

$$i\text{-th rule: If } v_x \text{ is } \tilde{A} \text{ and } y_{Ld} \text{ is } \tilde{B}, \text{ then } \Delta_i \text{ is } \tilde{C} \quad (3-18)$$

where \tilde{A} , \tilde{B} , and \tilde{C} are corresponding linguistic terms,

$$\tilde{A} = \{LOW, MED, HIGH\}$$

$$\tilde{B} = \{NB, NS, ZO, PS, PB\}$$

$$\tilde{C} = \{S, M, L\}$$

where the notation *NB*: negative big, *NS*: negative small, *ZO*: zero, *PS*: positive small, *PB*: positive big, *S*: small, *M*: medium, *L*: large.

Table 3-1 shows the rule base of FGS. These parameters of the membership functions for prior and consequent expressions are tuned manually to ensure satisfactory steering performance. The shapes chosen in FGS are trapezoidal for v_x , and triangular for y_{Ld} and Δ_{fg} ,

respectively, as shown in Fig. 3-7. In the defuzzification strategy, the center of area (COA) method is adopted to determine the gain

$$\Delta_{fg} = \frac{\sum_{i=1}^{15} \mu_i \times \Delta_i}{\sum_{i=1}^{15} \mu_i} \quad (3-19)$$

$$\mu_i = \min(\mu_A(v_x), \mu_B(y_{Ld})) \quad (3-20)$$

Finally, the terminal front-wheel steering quantity is thus obtained by

$$\delta_c = -\Delta_{fg} \cdot K_{fb} \underline{x} \quad (3-21)$$

TABLE 3-1. Rule base of FGS.

$v_x \backslash y_{Ld}$	LOW	MED	HIGH
NB	L	L	M
NS	L	M	S
ZO	M	S	S
PS	L	M	S
PB	L	L	M

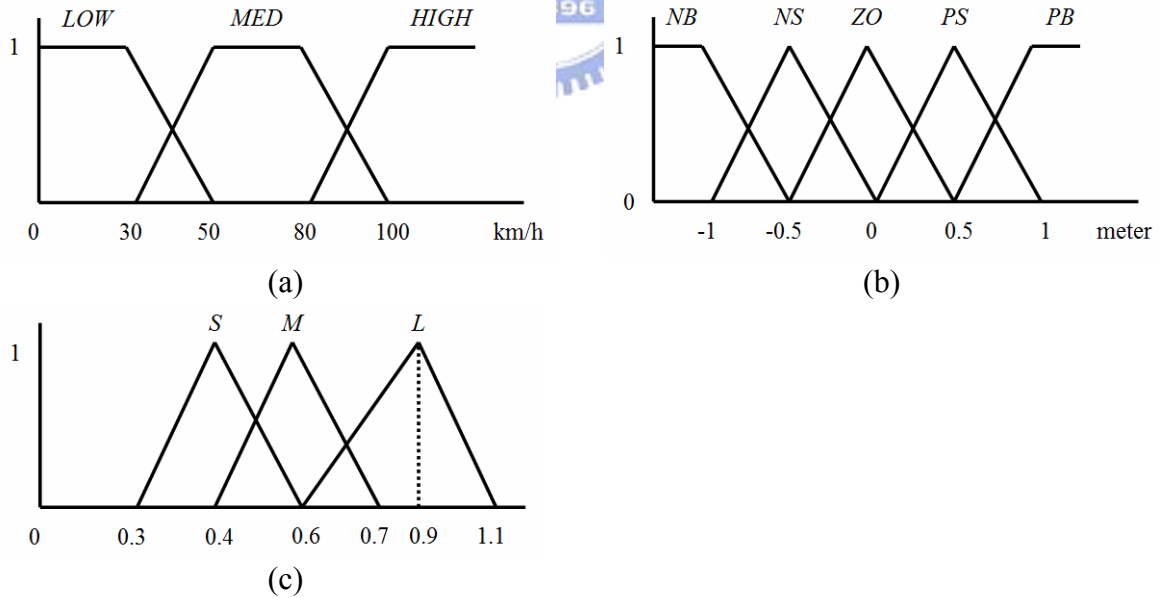


Fig. 3-7. The membership functions for (a) v_x , (b) y_{Ld} , and (c) Δ_{fg} .

As mentioned in Remark 1, during a vehicle steers on curves, the road curvature serves as an exogenous input to the previewed dynamics (3-8)-(3-9). In straight roads (zero curvature) case, both the look-ahead lateral offset and heading angle will be regulated to zero. For the

case of non-zero curvature, these two states will be stabilized to non-zero steady-state values as in Fig. 3-5. Although the curvature information at a look-ahead distance is useful to improve the steering performance while entering/exiting curves, it is difficult to obtain the correct information of road curvature in practice. An additional curvature estimator is proposed for feedforward control [16] to improve the transient behavior as the vehicle enters and exits curves. By examining (3-8) and (3-9), changes in curvature ahead can be anticipated by the varying lateral offset ahead. Therefore, FGS is able to compensate the effect from this unknown curvature information: if the lateral offset ahead of the vehicle increases, then the steering control will be increased. Figure 3-8 shows that y_{Ld} response with respect to step change of ρ_{Ld} (300^{-1} m^{-1} within 3 ~ 14 s) at a look-ahead distance 15 m is improved by FGS as compared with the pure feedback design. It can be seen that FGS possesses comparable performance with the curvature feedforward approach in [16].

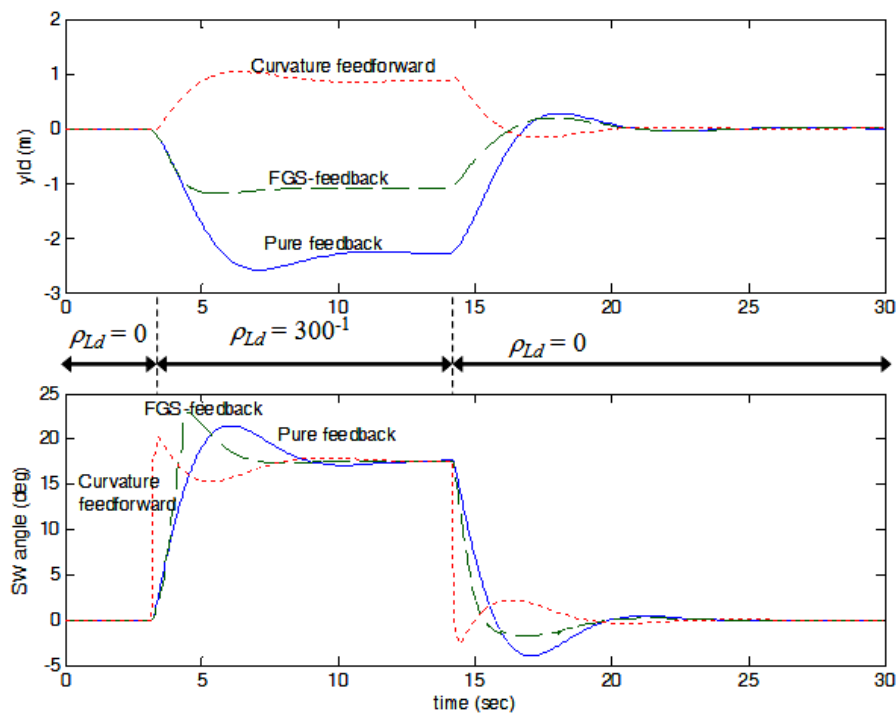


Fig. 3-8. The performance of the proposed pure feedback and FGS-feedback as compared to curvature-feedforward approach in [16].

Another important factor that influences closed-loop performance of the lateral controller is the variation of the cornering stiffness. When the vehicle turns, the mass would transfer onto the external wheels such that the tires pressure increase which leads to variations in the cornering stiffness. Stephant *et al.* have presented that the variations caused by this factor are

normally less than 10% even at speed to 90 km/h [56]. As shown in Fig. 3-9, the comparisons between the nominal value and the 10% variations of the front- and rear-tire cornering stiffness are given. The vehicle velocity is 90 km/h, and turning on a curve with the radius 200 m between 3 s and 16 s. It can be seen that our designed lateral controller still keeps the closed-loop stability and exhibits the robustness against the 10% variation in the cornering stiffness.

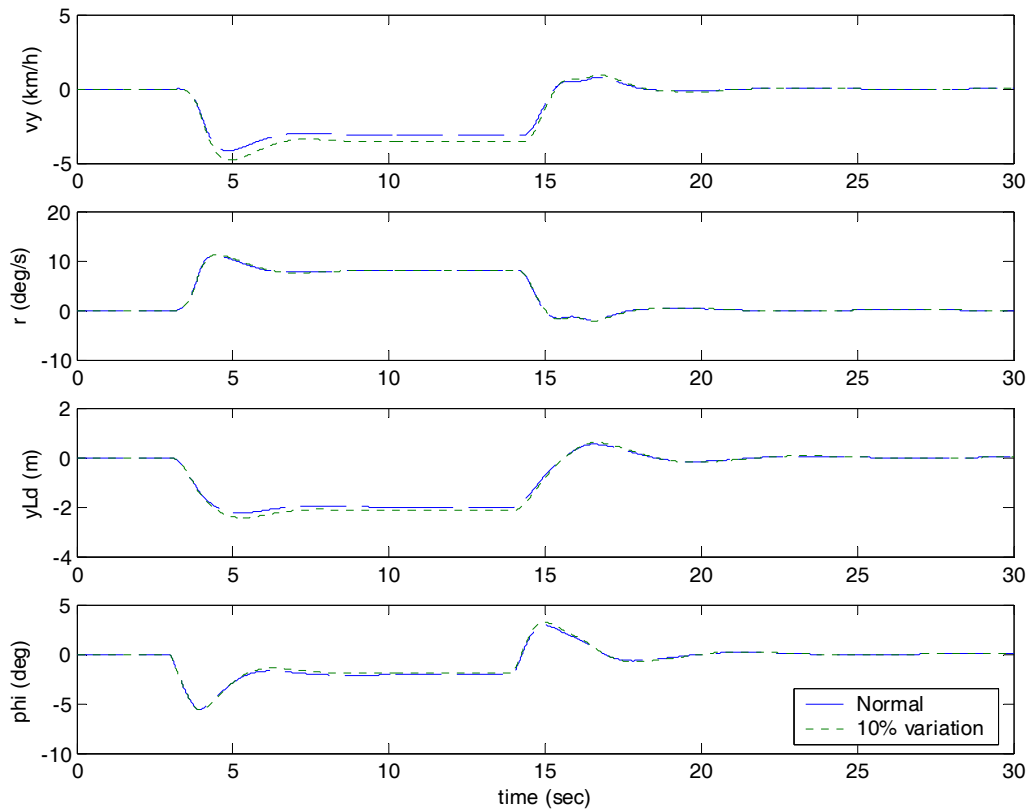


Fig. 3-9. Closed-loop performance for the normal condition and 10% variation in the cornering stiffness.

3.2.3. Analysis for the Lateral Controller with FGS

To achieve the persuasive performance of the steering control, the so-called *crossover model principle* is applied to examine the utility of the designed lateral controller. This principle has been empirically demonstrated to be applicable for driver's steering and any good driver model is expected to yield results that conform to this principle [40]. Therefore, it is expected to achieve the evidence of crossover model principle for our proposed lateral controller. By modifying Fig. 3-6 into a single-loop preview pursuit of lateral position, as

shown in Fig. 3-10, where $G_v(s) = [sI_n - A]^{-1}B$ represents the controlled-element transfer matrix of vehicle dynamics, and $\delta_c(t)$, the servo control, is related to the feedback control $\delta_f^0(t)$ through the FGS and a transport lag. The straight-line regulatory control test for the controller/vehicle system in Fig. 3-10 reveals the direct-loop frequency response, as shown in Fig. 3-11, which relates the output previewed lateral offset y_{Ld} to the error e . This system exhibits a slope of around -20 dB/decade for $\omega \approx \omega_c$, despite low and high vehicle velocities, i.e., the open-loop transfer function of the controller/vehicle system can be approximated as ω_c/s around the crossover frequency ω_c (phase margin = 90°). This result is consistent with the crossover model principle of the human operator. Besides, the included transport lag can be viewed as an “effective” time delay similar to the inherent limitation of human sensing, processing, and actuation to steer, such that the open-loop ratio of the system can be described by the transfer function $(\omega_c/s)e^{-s\tau}$.

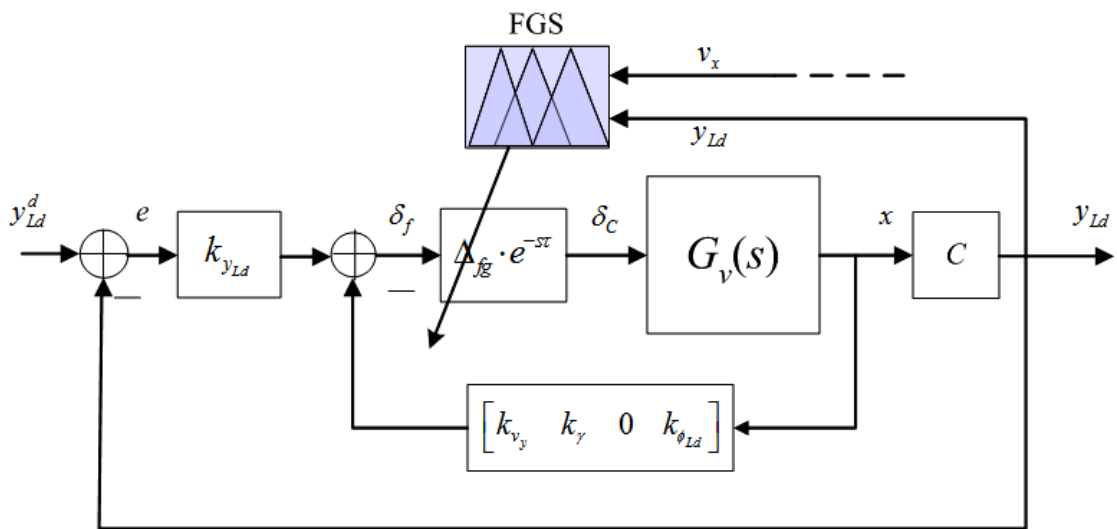
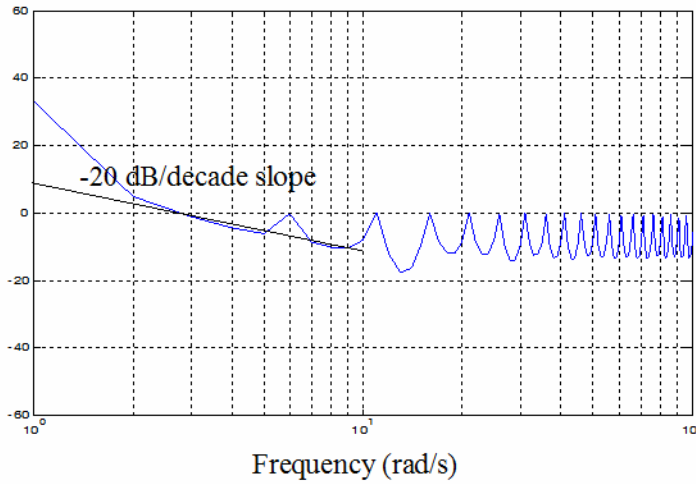


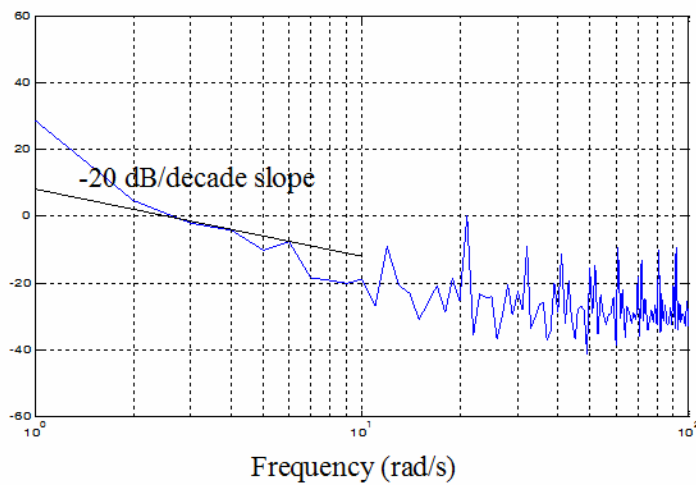
Fig. 3-10. Equivalent block diagram for the single-point previewed pursuit controller/ vehicle system.

By viewing Fig. 3-11, not only the frequency response in the vicinity of the crossover frequency ω_c is determined but also the crossover frequency at high velocity is lower than that at low velocity. This fact is also consistent with the experimental results concerning the crossover model principle [40], which is responsible for the lower crossover frequency and the difficulty of the drive task at higher velocity. For the skilled drivers, the smoother steering behavior will be employed to avoid excessive response especially under high velocities regardless the characteristics of vehicles. In Fig. 3-11, the characteristics of direct loop

response exhibit the smaller magnitude of high frequency at high velocity than that at low velocity. Table 3-2 shows that the crossover frequency is higher especially at a high velocity without FGS compensation. This result certainly meets the originality of FGS compensation design within the lateral controller. As the crossover frequency ω_c increases, the bandwidth of the closed-loop system increases thereby causing unexpected noise that may destabilize the system.



(a) Low velocity (about 60 km/h)



(b) High velocity (about 110 km/h)

Fig. 3-11. Frequency response characteristics for our steering controller/vehicle system.

TABLE 3-2. Crossover frequency of controller/vehicle system.

Diving velocity	W/O FGS	With FGS
About 60 km/h	2.90 rad/s	2.86 rad/s
About 110 km/h	3.94 rad/s	2.78 rad/s

3.3 Lane-change Control Design

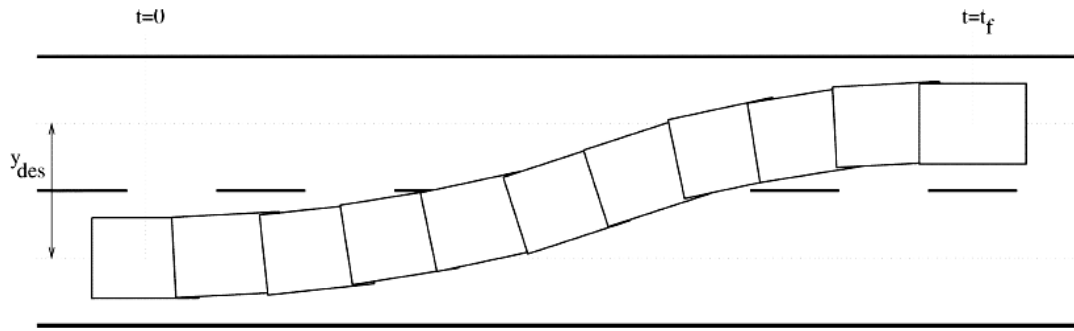


Fig. 3-12. Illustration of the lane-change maneuver.

While maintaining lane-keeping at a driving speed, a lane-change maneuver can be viewed as that the vehicle will travel a specified distance along the lateral axis with respect to its body orientation within a finite time period. After the vehicle aligning itself with the adjacent lane at the end of lane-change maneuver, the lane-keeping maneuver will be resumed smoothly. The lane-change maneuver is illustrated as Fig. 3-12. By considering the vehicle lateral kinematics

$$\begin{aligned} \dot{y}_{cg} &= v_{cg} \\ \dot{v}_{cg} &= a_{cg} \\ \dot{a}_{cg} &= J_{cg} \end{aligned}$$

(3-22)

where y_{cg} denotes the lateral position of the vehicle's CG with respect to the original lane center.

Initially ($t = 0$), $y_{cg}(0) = v_{cg}(0) = a_{cg}(0) = 0$ represents the ideal lane-keeping on the original road segment. At the end of the lane-change maneuver ($t = t_f$), $y_{cg}(t_f) = y_{des}$ should be achieved and $v_{cg}(t_f) = a_{cg}(t_f) = 0$ is required.

Here the proposed autonomous lane-change controller provides the assistance in the generation of the appropriate steering action to achieve the lane-change task without driver interfering. In this controller design, three assumptions are made:

- 1) only yaw rate and the steering angle are measured;
- 2) vehicle parameters are known within a bounded vibration with respect to their nominal values;
- 3) the road curvature does not change significantly throughout the lane-change maneuver.

During the lane-change maneuver, the lateral acceleration should be bounded as well for ride quality consideration. In [41], the most generalized time-optimal control signal that

satisfies the bounds for the lateral acceleration and the lateral jerk is proposed, as shown in Fig. 3-13.

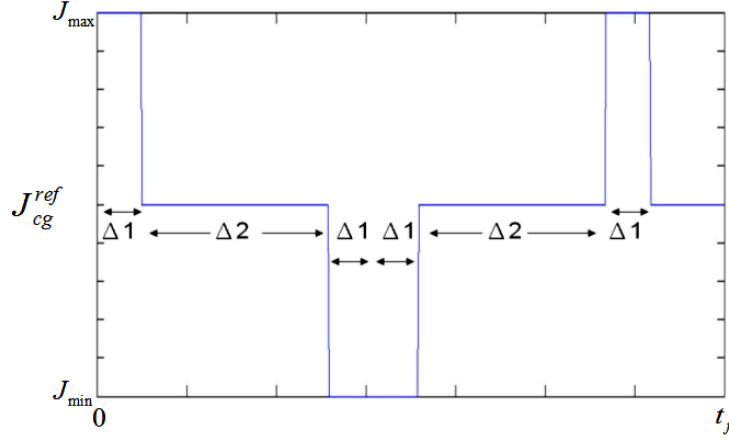


Fig. 3-13. Time optimal lateral jerk reference signal in [41].

According to the lateral jerk reference signal in Fig. 3-13, the final value of y_{des} can be yielded as

$$\begin{aligned}
 y_{des} &= \iiint J_{cg}^{ref}(\tau) d\tau d\alpha_1 d\beta_1 \\
 &= \Delta_1(2\Delta_1^2 + 3\Delta_1\Delta_2 + \Delta_2^2)J_{max}
 \end{aligned} \tag{3-23}$$

Given the desired lateral displacement y_{des} , the absolute bounds on the lateral acceleration A_{max} , and the jerk J_{max} , the above equation can be solved for Δ_1 and Δ_2 . Firstly, Δ_1 can be found by

$$\Delta_1 = \min \left\{ \frac{A_{max}}{J_{max}}, \sqrt[3]{\frac{y_{des}}{2J_{max}}} \right\}, \tag{3-24}$$

and then Δ_2 is the minimum real positive root of Δ_2 found from solving (3-23), or zero if there are no positive real roots.

In Fig. 3-13, it can be observed that the lateral jerk appears sharp variations from 0 to $\pm J_{max}$. There are high-frequency switchings between $\pm|J_{max}|$ while a_{cg} reaches the upper bound. To get smoother response of a_{cg} , therefore, we modify the lateral jerk J_{cg} and propose a modified reference jerk as shown in Fig. 3-14.

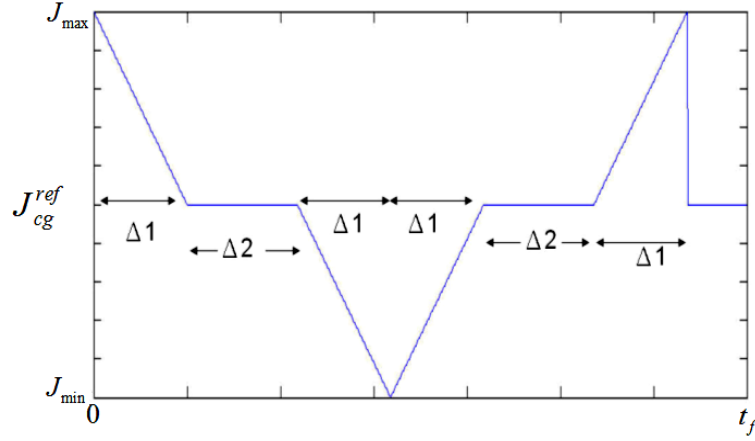


Fig. 3-14. Modified lateral jerk reference signal.

Thus the new final value of y_{des} can be yielded as

$$\begin{aligned}
 \frac{y_{des}}{2} &= \int_0^{\Delta_1} \int \int \left(-\frac{J_{max}}{\Delta_1} \alpha + J_{max} \right) d\alpha_1 d\beta_1 dt + \int_{\Delta_1}^{\Delta_1+\Delta_2} \int \int 0 d\alpha_1 d\beta_1 dt \\
 &+ \int_{\Delta_1+\Delta_2}^{2\Delta_1+\Delta_2} \int \int -\frac{J_{max}}{\Delta_1} (\alpha - (\Delta_1 + \Delta_2)) d\alpha d\beta dt \\
 &= \frac{J_{max}}{24} (16\Delta_1^3 + 20\Delta_1^2\Delta_2 + 6\Delta_1\Delta_2^2)
 \end{aligned} \tag{3-25}$$

Δ_1 is found by

$$\Delta_1 = \min \left\{ \frac{2A_{max}}{J_{max}}, \sqrt[3]{\frac{3y_{des}}{4J_{max}}} \right\} \tag{3-26}$$

and then the minimum real positive root of Δ_2 can be solved from (3-25), or zero if there are no positive real roots.

Now the ideal lateral jerk, acceleration, velocity, and the lateral offset trajectory are provided such that the vehicle can perform a lane-change maneuver and keep the ride comfort constraint. Due to the discontinuous availability of valid previewed data from the vision system during lane-to-lane transition, the control input for autonomous lane-change task is the commanded steering angle. Therefore, a reference SW signal is generated by utilizing the required information mentioned above. According to the lateral jerk reference in Fig. 3-14, the ideal lateral acceleration is obtained as

$$a_{cg}^{ref} = \int J_{cg}^{ref} d\tau \tag{3-27}$$

The changing of lateral offset in the vehicle's CG can be presented as

$$\dot{y}_{cg} = v_x \cdot \beta + v_x \cdot \phi \quad (3-28)$$

By assuming that the front-wheel angle δ_f is small, the vehicle side-slip can be viewed as nearly zero ($\beta \cong 0$) and y_{cg} can be obtained as

$$y_{cg} = \int (v_x \cdot \phi) dt \quad (3-29)$$

From the bicycle model (3-5), the transfer function from the front-wheel angle δ_f to the yaw rate γ can be obtained

$$H_{r-\delta_f}(s) = \frac{\gamma(s)}{\delta_f(s)} = \frac{q(s)}{p(s)} \quad (3-30)$$

where

$$q(s) = b_2 s + (a_3 b_1 - a_1 b_2)$$

$$p(s) = s^2 - (a_1 + a_4) s + a_1 a_4 - a_2 a_3$$

The yaw angle signals ϕ can be determined by using

$$\phi_{cg}(s) = H_{\gamma-\delta_f}(s) \cdot \frac{\delta_f(s)}{s} \quad (3-31)$$

In order to simplify the implementation stage of $H_{\gamma-\delta_f}(s)$, the frequency of this transfer function is studied at various longitudinal velocities. $|H_{\gamma-\delta_f}(s)|$ is plotted with $v_x = [5, 10, \dots, 30]$ m/s in Fig. 3-15(a). It can be observed that the dc-gain of $|H_{\gamma-\delta_f}(s)|$ is flat over a wide range of velocities in the domain of lower frequencies.

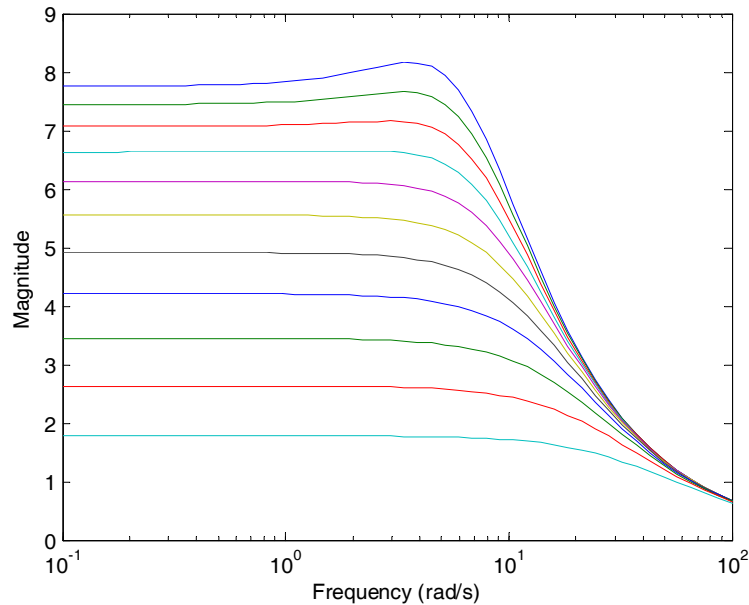


Fig. 3-15(a). Magnitude plot of front-wheel angle to yaw rate $H_{\gamma-\delta_f}(s)$.

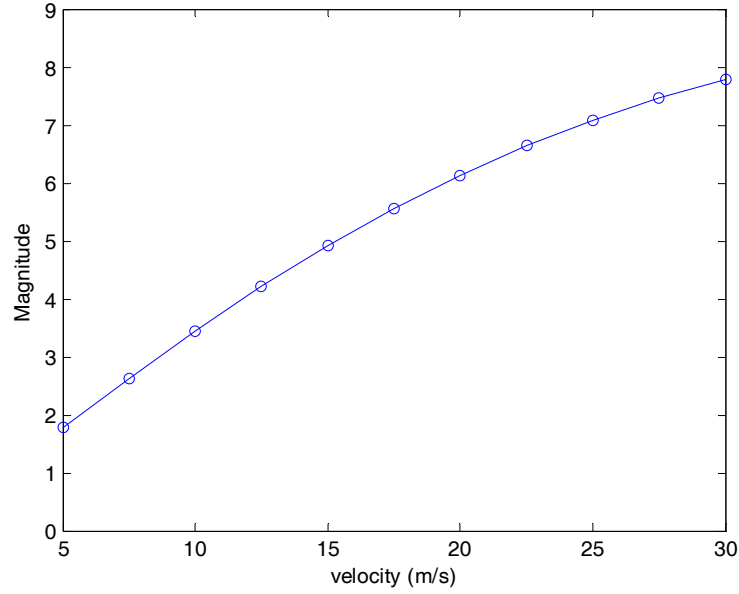


Fig. 3-15(b). Velocity-dependent function $h_{\gamma-\delta_f}(v_x)$ at velocities from 5 to 30 m/s.

A complete signal of front-wheel angle for operating lane-change is in the form of a sine wave. In general, the smooth lane-change will be accomplished within 5 ~ 6 s, and thus the major frequency component will be in the 1.0 ~ 1.2 rad/s range during the transition. Around this frequency, the magnitude of $H_{\gamma-\delta_f}(s)$ is essentially the same as the dc-gain for all longitudinal velocities [5, ..., 30] m/s. This result can be extended by implementing a velocity-dependent function $h_{\gamma-\delta_f}(v_x)$, as shown in Fig. 3-15(b), without any approximation and using it to generate a yaw rate command profile. Consequently, the equation (3-30) can be approximated as

$$\phi_{cg}(t) = h_{\gamma-\delta_f}(v_x) \int \delta_f(\tau) d\tau \quad (3-32)$$

Substitute (3-32) into (3-29), the lateral position of vehicle's CG can be obtained as

$$y_{cg} = h_{\gamma-\delta_f}(v_x) \cdot v_x \iint \delta_f d\tau dt \quad (3-33)$$

From the idea lateral acceleration in (3-27), the desired lateral offset in the lane-change maneuver for the vehicle CG can be generated as

$$y_{cg}^{ref} = \iint a_{cg}^{ref} d\tau dt \quad (3-34)$$

From (3-33) and (3-34), the referred front-wheel angle can be calculated

$$\delta_f = \frac{a_{cg}^{ref}}{h_{\gamma-\delta_f}(v_x) \cdot v_x}, \quad (3-35)$$

and the reference SW angle can be yielded as

$$\delta_{SW_ref} = \frac{i_{sr}}{h_{\gamma-\delta_f}(v_x)} \cdot \frac{a_{cg}^{ref}}{v_x} \quad (3-36)$$

Note that the generation of reference SW angle in (3-36) is adaptive to the vehicle speed, and by the given reference lateral jerk a_{cg}^{ref} , the time of lane-change maneuver will be limited to t_f which is previously defined.

In our proposed lane-change controlling strategy, the road is assumed to be straight during the entire duration of the lane-change maneuver. Therefore, there is no compensation for variations in the road curvature. The open-loop lane-change's feasibility will be easily declined by changes in road curvature and level. In order to improve the feasibility of lane-change control, the free lane-change control is divided into two controlling stages:

- 1) On-set lane-change trajectory: In the first stage, the initial conditions of the lateral data are considered into the generation of reference SW command that the subject-vehicle follows to leave the traveling lane and to perform the free lane-change maneuver. Thus the Eq. (3-36) is modified to

$$\delta_{SW_ref} = \hat{\delta}_{SW0} + \frac{i_{sr}}{h_{\gamma-\delta_f}(v_x)} \cdot \frac{a_{cg}^{ref}}{v_x} \quad (3-37)$$

where $\hat{\delta}_{SW0}$ is the initial condition of SW angle which is computed from (3-21) with the initial conditions $\underline{x}(0)$. The observer in (3-16) and (3-17) can be used for these initial condition estimations.

- 2) Lane-catching trajectory: The difference between the actual road reference and the virtual road reference leads to that the lane-change maneuver is likely to end with a lateral offset from the center of the neighboring lane and possibly with an orientation error. This resulting deviation can be corrected by the lane-keeping control which is resumed as soon as the lane-change maneuver is completed. Thus the second stage is to shorten the eventual period of lane-change maneuver, and let the lane-keeping control lead the subject-vehicle to align itself to the target centerline once the vision system re-catches the target lane data.

Note that the early-switch causes that the lane-change maneuver ends with an offset error (with maximum value of half road width); nevertheless, uncomfortable ride can be evitable for the applied FGS which adjusts the lane-keeping steering according to the current velocity and the lateral offset signal.

Chapter 4

Longitudinal Control System Design

4.1. Modeling for Vehicle Longitudinal Dynamics

The true vehicle dynamics is unfortunately complicated and includes high nonlinearity in the interaction between propulsion, roadway interface, and aerodynamics, ..., et. However, the vehicle longitudinal dynamics under non-braking conditions can be represented by one nonlinear model in the form of third-order transfer function shown in Fig. 4-1 [42]. This model is employed in this chapter to describe the nonlinearity in velocity dependent dynamics between the voltage applied on throttle valve V_i and the forward velocity of the vehicle V .

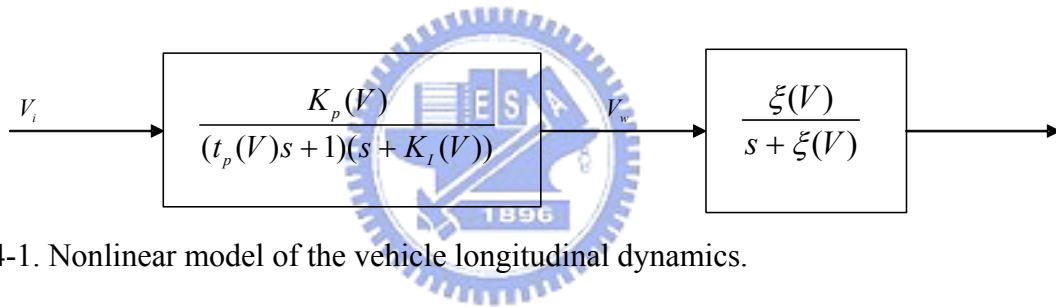


Fig. 4-1. Nonlinear model of the vehicle longitudinal dynamics.

The connection between these velocity-dependent parameters and the forces/drags of vehicle/tire is as follows: $t_p(V)$ is associated with the throttle actuator and propulsion system and their interaction with the roadway interface, $K_l(V)$ is associated with aerodynamic drag and vehicle mass, $K_p(V)$ is associated with the throttle actuator and propulsion system, and $\xi(V)$ is associated with interaction between tires and roadway. Reformulate the model and one can obtain

$$H(s, V) = \frac{V(s)}{V_i(s)} = \frac{\psi(V)}{s^3 + q_1(V)s^2 + q_2(V)s + q_3(V)} \quad (4-1)$$

with the velocity dependent parameters

$$\psi(V) = \frac{K_p(V)\xi(V)}{t_p(V)}, \quad q_1(V) = \frac{1}{t_p(V)} + K_l(V) + \xi(V)$$

$$q_2(V) = \frac{1}{t_p(V)} + K_l(V)\xi(V) + \frac{\xi(V)}{t_p(V)}, \quad q_3(V) = \frac{K_l(V)\xi(V)}{t_p(V)}.$$

The experimental procedure for model parameters identification is similar to the approach in [42]; nevertheless, instead of estimating each velocity dependent variable (t_p , K_I , K_p , and ξ), evidently it is more intuitively to identify those parameters ψ , q_1 , q_2 , and q_3 , under varying velocities of the vehicle. The specification of velocity dependent parameters ψ , q_1 , q_2 , and q_3 , are accomplished via a closed-loop model-matching technique such that the responses of the model are matched to those obtained from corresponding real vehicle wherein the same driving controller $D(s)$ is employed. The configuration of closed-loop simulation model is shown in Fig. 4-2, and note that here the characteristics of throttle actuator is considered into the identification procedure, which are presented by saturation scheme for applied voltage V_i and a transport lag existing in controller command to actuator.

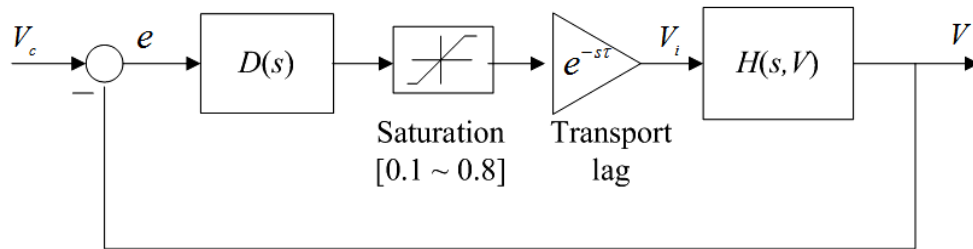


Fig. 4-2. Closed-loop configuration employed in the identification of ψ , q_1 , q_2 , and q_3 .

The identification procedure is repeated several times for each specified command velocity for the vehicle V_c until the consistent response is obtained. Note that the driving controller $D(s)$ set in the configuration of closed-loop model can be chosen different so as to the model parameters are demonstrated to be independent of the specific controller choice [42]. Since the true vehicle dynamics is not known in the beginning, the choice of $D(s)$ must be conservative. In the experiment, it is found that the great amount of gain in the driving controller is inadequate for noise in sensing velocity and bounded input constraint of throttle voltage. Therefore, one simple PI-controller $D_1(s)=(0.5s+0.12)/s$ and filter $D_2(s)=(0.5s+0.2)/(s+2)$, respectively, are determined in the closed-loop configuration. Through the recorded throttle voltage V_i and the velocity of vehicle V in these tests, the quantities of velocity dependent parameters ψ , q_1 , q_2 , and q_3 , are appropriately adjusted and assigned values for each condition of driving controller and velocity of the vehicle, so as to match the response of model to the real vehicle. In this way, the velocity dependent parameters ψ , q_1 , q_2 , and q_3 , in the model are all real functions of the longitudinal velocity of the vehicle. The obtained consistent values of these parameters ψ , q_1 , q_2 , and q_3 , independent of condition of

driving controller $D(s)$, and the averaged results verses velocity are plotted in Fig. 4-3.

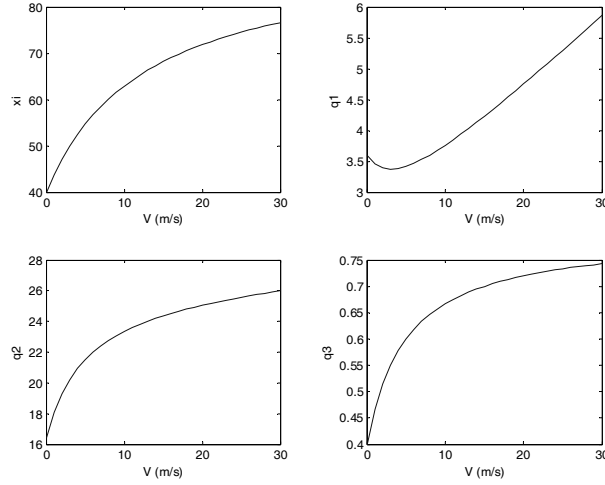


Fig. 4-3. The averaged values of ψ , q_1 , q_2 , and q_3 , verses velocity of the vehicle.

For the interesting range of velocity $0 \leq V \leq 30$ m/s in Fig. 4-3, the parameters may be presented functionally with velocity V as

$$\begin{aligned} \psi(V) &= 2.01 \frac{20 + 3.6V}{1 + 0.078V}, & q_1(V) &= 0.12 \frac{V^2 + 22V + 150}{V + 5} \\ q_2(V) &= 0.04 \frac{V^2 + 660V + 2052}{V + 5}, & q_3(V) &= \frac{0.8V + 2}{V + 5} \end{aligned} \quad (4-2)$$

Thus, it is clear to see that these parameters are varying functionally with velocity of the vehicle and the upper and lower limits over the range of interest for q_1 , q_2 , and q_3 are

$$40.20 \leq \psi \leq 77.03$$

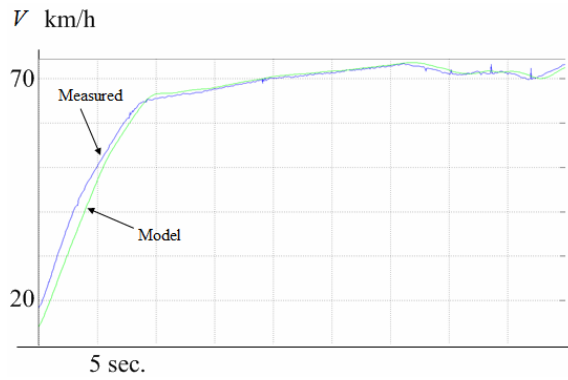
$$3.38 \leq q_1 \leq 5.86$$

$$16.42 \leq q_2 \leq 26.00$$

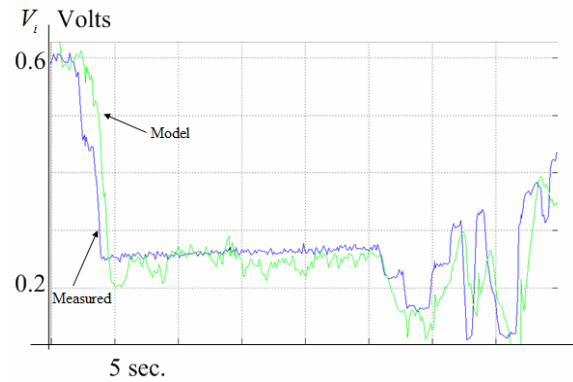
$$0.40 \leq q_3 \leq 0.74.$$

Even though the model is identified for small variation in velocity about a given fixed velocity, it is also valid for the case of large signal provided change in velocity is smooth. This result also agrees with the one in [42]. Here we consider two normal cases of comparison between the response of the real vehicle and the simulation model with the driving controller $D(s) = D_2(s)$. The first case is to accelerate the vehicle from initial velocity 5 to 60 km/h; in the second case, the vehicle is accelerated to a specified velocity (about 70 km/h) and kept this velocity. It can be expected that for smooth acceleration command, the applied voltage on throttle actuator need not be large, while the great quantity of input throttle voltage is required

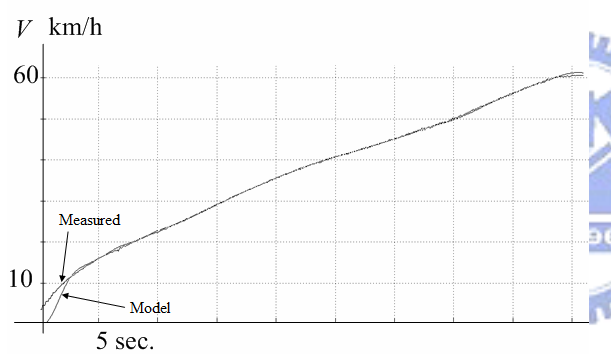
for vehicle in rapid acceleration operation. In Fig. 4-4, two cases show the direct response (open-loop) from the controlled voltage V_i posing to the output velocity of the simulation model and the vehicle platform (Taiwan *i*TS-1), respectively. For each case, the good correlation exists in these comparisons for the values, variations, and the time of occurrence.



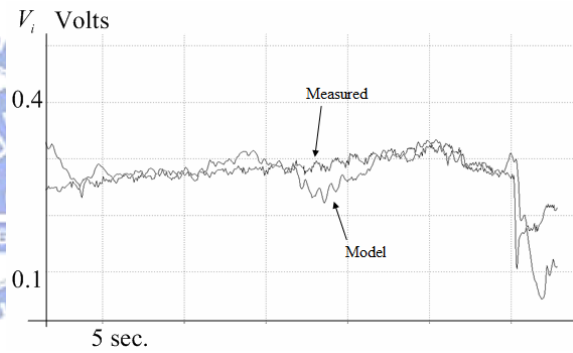
Case 1. Velocity response.



Case 1. Controlled throttle voltage.



Case 2. Velocity response.



Case 2. Controlled throttle voltage.

Fig. 4-4. The I/O responses of the simulation model and its comparison with the real vehicle.

4.2. Longitudinal Automation System Design

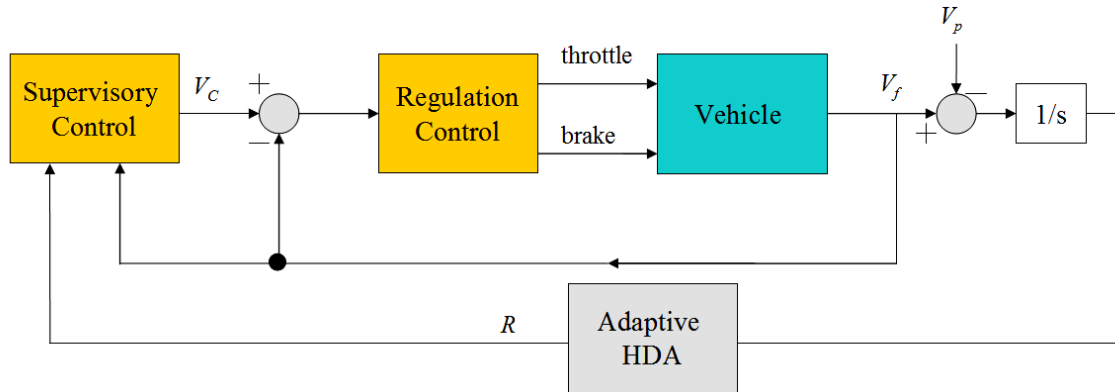


Fig. 4-5. Dual-loop structure of the longitudinal automation system.

As shown in Fig. 4-5, the longitudinal automation system is developed in a dual-loop structure. The adaptive horizontal detection area (HAD) deals with the data from the on-board sensors according to the SW angle and vehicle dynamics. Instead of horizontal detection in a fixed pattern, the adaptive detection area performs the adaptive action in order to guarantee that the preceding vehicle is detected on both straight and curved roads. A main loop supervisory control determines the reference velocity based on the recognized distance from the adaptive HDA and the current velocity of vehicle. A sub-loop regulation control then manipulates the throttle and brake actuators to achieve the desired velocity. By recalling Fig. 2-3, the supervisory control is the role of reference velocity calculation in the upper-level control, and the regulation control keeps this reference velocity by generating the throttle and brake controlling signal to actuators.

4.2.1. Adaptive HDA

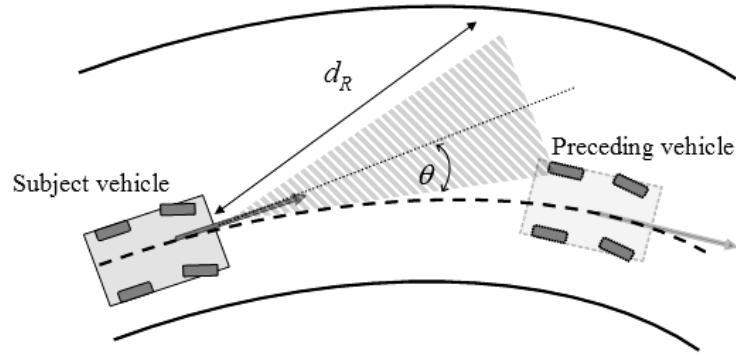


Fig. 4-6. Illustration of the scenario of a vehicle following on curves.

On straight roads, the headway distance can be measured from the forward-looking sensor (FLS) if it can be assumed that there is no failure in the sensor. However, failure to detect a vehicle ahead could be due to curves in the road. In the specification of [43], ACC systems are required to be provided with curve capability; i.e., the system should enable steady-state vehicles to follow with an appropriate headway distance on curves. As illustrated in Fig. 4-6, the preceding vehicle can not be detected by the FLS of the following vehicle if the detection area is too narrow. Such a failure might result in instant acceleration. However, if the detection area is too broad, some unexpected objects near the road might be detected which may cause the throttle to be off. The issue of curve capability, nonetheless, is being considered at present in other longitudinal control systems.

The turning behavior of a bicycle model as depicted in Chapter 3 has been considered using the formula below in which the lateral dynamic from steering angle δ_f to lateral velocity v_y and yaw rate γ is presented as

$$\begin{bmatrix} \dot{v}_y \\ \dot{\gamma} \end{bmatrix} = A_s \begin{bmatrix} v_y \\ \gamma \end{bmatrix} + B_s \delta_f \quad (4-3)$$

$$\text{with } A_s = \begin{bmatrix} \frac{-(C_f + C_r)}{mV_f} & -V_f + \frac{-aC_f + bC_r}{mV_f} \\ \frac{-aC_f + bC_r}{I_z V_f} & \frac{-(a^2 C_f + b^2 C_r)}{I_z V_f} \end{bmatrix}, \quad B_s = \begin{bmatrix} \frac{C_f}{m} \\ \frac{aC_f}{I_z} \end{bmatrix}$$

In addition to detect the existence of the preceding vehicle, the look-ahead information of the

subject vehicle (also referred to as the following vehicle) must be considered. By assuming the vehicle traveling on a curve with a radius R_f , the equations (similar to (3-8) and (3-9)) capturing the evolution of the point at a look-ahead distance L_d due to the motions of the vehicle and changes in the road geometry are the following

$$\dot{y}_{Ld} = v_y + L_d \cdot \gamma + V_f \cdot \varepsilon_{Ld} \quad (4-4)$$

$$\dot{\varepsilon}_{Ld} = \gamma - V_f \cdot R_f \quad (4-5)$$

It should be noted that here the road curvature is assumed to be constant due to the assumption of a steady-state analysis. The reason is that the vehicle will not reach a steady-state condition while traveling on a road with varying curvatures and this makes it difficult to investigate the static relation. By considering a steady-state motion in which the subject vehicle tracks the curved road perfectly at a constant velocity V_f , the variations of the vehicle lateral dynamics (4-3) and the look-ahead motion (4-4) and (4-5) can be set to zero, i.e., $\dot{v}_y = \dot{\gamma} = \dot{y}_{Ld} = \dot{\varepsilon}_{Ld} = 0$. In the following, the subscript of *ss* denotes the value in the steady-state condition. By calculating the direction, the steady-state steering angle can be obtained

$$\delta_{fss} = \frac{1}{R_f} \left(a + b - \frac{mV_f^2(aC_f - bC_r)}{(a+b)C_f C_r} \right) \quad (4-6)$$

The steady-state look-ahead lateral offset can be adopted as [44]

$$y_{Ldss} = h_{ss} - R_f \quad (4-7)$$

where $h_{ss} = \sqrt{R_f^2 + L_d^2 + 2R_f L_d (-v_{yss} / V_f)}$.

Furthermore, at steady-state the lateral dynamics (4-3) can be represented as

$$A_s \begin{bmatrix} v_{yss} \\ \gamma_{ss} \end{bmatrix} = -B_s \delta_{fss} \quad (4-8)$$

and this holds if and only if

$$v_{yss} = -r_{ss} T \quad (4-9)$$

$$\text{with } T = \frac{-b + amV_f^2}{(a+b)C_r}.$$

In Equation (4-8) the term on the left-hand side is in the range space of matrix B_s . It should be noted that the fixed values of the yaw rate during the steady-state turning maneuver can be obtained by using

$$\gamma_{ss} = V_f / R_f \quad (4-10)$$

By substituting (4-9) and (4-10) into (4-5), the steady-state look-ahead lateral offset can be

rewritten as

$$y_{Ldss} = \sqrt{R_f^2 + L_d^2 + 2L_dT} - R_f \quad (4-11)$$

From (4-6) and (4-11), one obtains

$$\frac{y_{Ldss}}{\delta_{fss}} = \frac{R_f \sqrt{R_f^2 + L_d^2 + 2L_dT} - R_f^2}{(a + b - mV_f^2(aC_f - bC_r))/(a + b)C_fC_r} \quad (4-12)$$

It is also reasonable to assume that

$$|L_d^2 + 2L_dT| / R_f^2 \ll 1 \quad (4-13)$$

and the following approximation via Taylor's expansion can be obtained as

$$\sqrt{R_f^2 + L_d^2 + 2L_dT} = R_f + \frac{L_d^2 + 2L_dT}{2R_f} \quad (4-14)$$

Through (4-14), relation (4-12) becomes

$$\frac{y_{Ldss}}{\delta_{fss}} = \frac{L_d^2 + 2L_dT}{2(a + b - V_f^2 P)} \quad (4-15)$$

where $P = m(aC_f - bC_r)/(a + b)C_fC_r$.

It should be noted that P is also the under-steer coefficient of the vehicle [45]. By recalling Fig. 4-6, the following approximation can be applied

$$y_{Ldss} \cong d_R \cdot \theta \quad (4-16)$$

By substituting (4-15) into (4-16), one can obtain the relation from the steering angle to the adaptive detection angle

$$\frac{\theta}{\delta_{fss}} = \frac{L_d^2 + 2L_dT}{2d_R(a + b - V_f^2 P)} =: \frac{K_\theta}{d_R} \quad (4-17)$$

The steering angle can be substituted with the steering wheel (SW) angle using a constant ratio $\delta_{SW} = i_{sr} \cdot \delta_f$ [32, 46]. Normally the value of i_{sr} is between 18 and 22 for passenger vehicles. In (4-17), the resulting feature is an adaptive ratio between the adaptive detection angle and the steering angle which is independent of the road curvature. It can be observed that the adaptive ratio is updated as the vehicle velocity changes. The calculated y_{Ldss} refers to the offset between the point at the look-ahead distance and the position through which the vehicle will pass. When the vehicle is turning at a higher velocity, the look-ahead lateral offset increases such that the detection area expands in the same direction as the SW. Moreover, with respect to a reduced road curvature (or a longer radius), the look-ahead lateral offset decreases in that the detection area expands less. Table 4-1 depicts this result when $L_d = 42$ m and $d_R = 40$ m are given (as specified in the experiments).

TABLE 4-1. (δ_{sw} , θ) with varying velocities and radiuses of curves.

$R_f \backslash V_f$	200 m	300 m	400 m	500 m
40 km/h	(19.6°, 6.9°)	(14.5°, 5.1°)	(10.9°, 3.8°)	(8.7°, 3.1°)
60 km/h	(23.9°, 9.2°)	(15.5°, 6.1°)	(11.6°, 4.6°)	(9.3°, 3.7°)
80 km/h	(25.1°, 11.9°)	(16.8°, 7.9°)	(12.6°, 5.9°)	(10.1°, 4.7°)
100 km/h	(27.6°, 16.6°)	(18.4°, 11.1°)	(13.8°, 8.3°)	(11.1°, 6.6°)

Two calculations given in ISO 15622 are applied to verify the feasibility of the developed algorithm in (4-17). The HDA formula of ISO 15622 is introduced in Appendix B. The two vehicles cruise on a curve radius of 500 m and 125m with a constant velocity of 31.67 m/s and 16.94 m/s, respectively. The comparative results (the steady-state look-ahead lateral offset and the detection angle) between ISO 15622 and the proposed algorithm are presented in Table 4-2. The evaluation criterion for the curves in ISO 15622 is dependent on the vehicle velocity and the lateral acceleration constraints. Furthermore, this criterion is a minimum requirement for the detection of the forward vehicle on the specified range of curves. The developed maneuver in (4-17) involves the major coefficients of the subject vehicle since they are derived from the lateral dynamics which determine the turning behavior of the vehicle. As a result, the proposed algorithm certainly satisfies the minimum requirement of ISO 15622 and provides a more confident detection range.

TABLE 4-2. Comparative results between ISO 15622 and adaptive HDA.

		ISO 15622	Adaptive HDA
Example 1 ($R_f = 500$ m)	y_{Ldss}	4.00 m	5.07 m
	θ	$\pm 3.70^\circ$	$\pm 4.61^\circ$
Example 2 ($R_f = 125$ m)	y_{Ldss}	4.60 m	4.83 m
	θ	$\pm 7.80^\circ$	$\pm 8.92^\circ$

4.2.2. Supervisory control

After detecting road environment and determining the operation modes, we estimate the desired velocity by a two-stages approach. The desired acceleration of each operation mode is determined in the first stage, and then is converted to the desired velocity in the second stage. This velocity is then issued to vehicle-body control. We here use a desired velocity, instead of acceleration, due to that the subject-vehicle's velocity can be measured directly. Moreover, high-frequency noise problems from sensed velocity differential can be avoided.

In the first stage, we adopt the sliding mode control (SMC) technique to design the corresponding control laws for various driving modes. A proper surface S is defined as the function of the system states, and the sliding manifold $S=0$ defined on the closed-loop system is asymptotically stable. To satisfy the reachable and sliding condition, we choose S such that $\dot{S} < 0$ while $S \neq 0$ ($\dot{S} = C(S)$ is a continuous function of S). One conventional method of the sliding surface design is as [47]

$$S = \left[\frac{d}{dt} + \lambda \right]^{n-1} e \quad (4-18)$$

where n is the relative degree of the system, λ is the chosen sliding surface gain, and e presents system error which is desired to drive to zero. In this way the state trajectory is forced to a stable manifold state ($S=0$) in a finite time interval, and then slides toward equilibrium state. We define the control law as the first derivative of the surface S .

In the CC mode, the desired acceleration is determined such that the subject-vehicle can track any assumed velocity under comfort situation. We define the velocity tracking error as $e_V = V_f - V_{des}$. The sliding surface is chosen as $S_{CC} = e_V$ and the control law is defined as

$$\dot{S}_{CC} = -K_{CC} S_{CC} \quad (4-19)$$

with constant parameter $K_{CC} > 0$ for S_{CC} to approach zero. This control law satisfies globally asymptotical stable and $S_{CC} \dot{S}_{CC} < 0$ criteria. We note that in SMC-related literatures the control law always includes a discontinuous sign function; for example, $C(S_{CC}) = -K_{CC} S_{CC} + k_0 \text{sgn}(S_{CC})$. This will result in unexpected chattering phenomena and high-frequency noise. Besides, the proposed continuous function in (4-19) is a feasible choice for implementation due to its simplicity. Furthermore, we constrain the acceleration command within one $a_{f\max}$ for ride-comfort consideration, especially when the initial value of e_V is large. Therefore, the sliding surface is modified as

$$S_{VT} = -a_f + a_{f\max} \text{sat}\left(\frac{a_f + e_V}{a_{f\max}}\right), \quad (4-20)$$

where $\text{sat}(x) = \begin{cases} x, & \text{as } |x| < 1 \\ \text{sign}(x), & \text{as } |x| \geq 1 \end{cases}$.

In case of $|a_f + e_V| < a_{f\max}$, the sliding surface is $S_{VT} = e_V$ and the desired acceleration is

$$a_{CC} = \dot{V}_{des} - K_{CC}e_V. \quad (4-21)$$

For the case $|a_f + e_V| \geq a_{f\max}$, the sliding surface becomes

$$S_{CC} = -a_f \pm a_{f\max}, \quad (4-22)$$

and the desired acceleration is

$$a_{CC} = \frac{-\dot{a}_f}{K_{CC}} \pm a_{f\max}. \quad (4-23)$$

The jerk in (4-23) can be neglected in practice since it may constrain the achievement of the desired acceleration. So we have $a_{CC} = \pm a_{f\max}$. The proposed control laws in (4-21) and (4-23) are simple, and contains vehicle velocity only. Therefore, the implementation and the realization of ride comfort are achievable.

In the ACC mode, we propose the control law based on the desired acceleration such that a safety following-distance from the preceding-vehicle is maintained. The constant headway time policy is commonly suggested as a safe practice for human drivers and is frequently used in ACC systems design. In this policy, the desired inter-vehicle range is $R_{des} = \sigma V_f + L$, and the spacing error between the desired and relative headway distances is defined as

$$e_R = R - R_{des} = R - (\sigma V_f + L), \quad (4-24)$$

where the relative distance $R = X_p - X_f$.

The sliding surface is chosen as

$$S_{ACC} = -a_f + a_{f\max} \text{sat}\left(\frac{a_f + e_R}{a_{f\max}}\right). \quad (4-25)$$

In case of $|a_f + e_R| < a_{f\max}$, the sliding surface is stable obviously since $S_{ACC}=0$ as $e_R=0$. By choosing the control law as

$$\dot{S}_{ACC} = -K_{ACC}S_{ACC} \quad (4-26)$$

with $K_{ACC} > 0$, the desired acceleration can be derived as

$$a_{ACC} = \frac{1}{\sigma} (K_{ACC}e_R + \dot{R}). \quad (4-27)$$

For $|a_f + e_R| \geq a_{f\max}$, the sliding surface becomes

$$S_{ACC} = -a_f \pm a_{f\max}, \quad (4-28)$$

and the desired acceleration is

$$a_{ACC} = \frac{-\dot{a}_f}{K_{ACC}} \pm a_{f\max}. \quad (4-29)$$

We note that the jerk of the following vehicle in (4-29) is negligible ($a_{ACC} = \pm a_{f\max}$).

Remark 1: For ride-quality consideration, the estimated acceleration of the subject-vehicle in conventional approaches is constrained. If $|a_{ACC}| \geq a_{f\max}$, then $a_{ACC} = \pm a_{f\max}$. However, this can not be guaranteed for the real acceleration of a vehicle. We use the saturation function of the sliding surface to constrain the actual acceleration from reaching the desired value. In other words, our control law can limit the real acceleration of controlled vehicle. With respect to $a_{f\max}$, the value of 2.0 m/s² and -3.0 m/s² can be set for acceleration and deceleration, respectively, in accordance with the specification [43].

As far as the supervisory control is concerned, the transport lag in the servo-loop should be analyzed in the performance of ACC design. The servo-loop can be approximated by a first-order lag system

$$a_i = \frac{1}{\tau_{lag}s + 1} a_{i,des} \quad (4-30)$$

where a_i is the subject-vehicle's actual acceleration, $a_{i,des}$ is the desired acceleration from the ACC mode design (4-27), and τ_{lag} is the servo-loop time constant. The vehicle's velocity and position can be obtained through integration.

By considering a platoon of identical ACC-controlled vehicles running on highway in a string, the string stability refers to a property in which spacing errors are guaranteed not to amplify as they propagate toward the tail of the platoon [2]. The errors e_{Ri} and e_{Ri-1} are denoted as the spacing deviation from the desired safety-distance as in (4-24) for the subject-vehicle and the preceding-vehicle, respectively, and the objective for the string stability can be stated as follows [2]:

$$1) \quad e_{Ri-1} \rightarrow 0 \Rightarrow e_{Ri} \rightarrow 0 \quad (4-31a)$$

$$2) \quad \|H(s)\|_{\infty} = \left\| \frac{e_{Ri}}{e_{Ri-1}} \right\|_{\infty} \leq 1 \quad (4-31b)$$

The control laws for two consecutive vehicles are

$$\dot{a}_{i-1} = \frac{1}{\tau_{lag}} \left[\frac{K_{ACC}}{\sigma} e_{R_{i-1}} + \frac{1}{\sigma} \dot{R}_{i-1} - a_{i-1} \right] \quad (4-32)$$

$$\dot{a}_i = \frac{1}{\tau_{lag}} \left[\frac{K_{ACC}}{\sigma} e_{R_i} + \frac{1}{\sigma} \dot{R}_i - a_i \right] \quad (4-33)$$

After considerable algebraic computation, the string stability conditions of (4-31) can be guaranteed as long as

$$\sigma > 2\tau_{lag} \quad (4-34)$$

where τ_{lag} is the time constant of the servo-loop as in (4-30).

In other words, the string stability condition in (4-34) means that the headway time must be chosen above the critical value of $2\tau_{lag}$. The time constant τ_{lag} arises due to lag in actuators, the bandwidth of the lower level control, and filtering of the range finder. Typically, experimental work shows that τ_{lag} has a value which varies between 0.5 and 1.0 s. In the specification of [43], the spacing policy allows a headway time between 1.0 and 2.2 s. At highway the vehicle velocity can be in the range of 60–100 km/h. In our system, the headway time is set as 1.0 s for ACC mode and thus the spacing between cars can be translated into 17–28 m which is adequate to achieve the safe car-following.

Besides, for consideration of increasing highway capacity, the subject-vehicle may keep a fixed spacing from the preceding-vehicle, that is, $\sigma = 0$ and $R_{des} = L$. Therefore, the desired acceleration can not be derived according to the sliding surface in (4-25) and the control law in (4-26). We choose the following sliding surface defined on the error and error-variation as

$$S_{FT} = -a_f + a_{f\max} \text{sat}\left(\frac{a_f + \dot{e}_R + \lambda e_R}{a_{f\max}}\right). \quad (4-35)$$

In case of $|a_f + \dot{e}_R + \lambda e_R| < a_{f\max}$, the sliding surface becomes

$$S_{FT} = \dot{e}_R + \lambda e_R. \quad (4-36)$$

The stability of the sliding surface in (4-36) is examined by setting $S_{FT} = 0$, and the error dynamics $e_R(t) = e^{-\lambda t}$ is asymptotically stable for all positive λ . By differentiating (4-36), the acceleration of the subject-vehicle can be obtained by $\dot{S}_{FT} = \ddot{e}_R + \lambda \dot{e}_R$. We then choose the control law as

$$\dot{S}_{FT} = -K_{FT} S_{FT}, \quad (4-37)$$

where $K_{FT} > 0$ is to guarantee the desired condition and asymptotic stability. By (4-36) and (4-37), the desired acceleration is derived as

$$a_{FT} = K_{FT} (\dot{e}_R + \lambda e_R) + a_p + \lambda \dot{R}. \quad (4-38)$$

The sliding surface is

$$S_{FT} = -a_f \pm a_{f\max} \quad (4-39)$$

for $|a_f + \dot{e}_R + \lambda e_R| \geq a_{f\max}$, and the desired acceleration is

$$a_{FT} = \frac{-\dot{a}_f}{K_{FT}} \pm a_{f\max}. \quad (4-40)$$

We note that the jerk of the subject-vehicle in (4-40) is still negligible ($a_{FT} = \pm a_{f\max}$). In this mode, only the fixed-distance tracking for two cars is discussed instead of the control for a platoon. Equation (4-37) ensures that the vehicle states converge to the sliding surface S_{FT} , and the subject-vehicle can track the preceding-vehicle with a constant spacing. To verify the asymptotic stability for the car-following controller (4-33), a necessary condition [5] for such stability is

$$\left| \frac{V_f(s)}{V_p(s)} \right|_{s=j\omega} \leq 1, \quad \forall \omega, \quad (4-41)$$

where $V_p(s)$ and $V_f(s)$ are the Laplace transform of the velocity of the preceding-vehicle and the subject-vehicle, respectively. To analyze the stability of the system, the following transfer function can be obtained from (4-38)

$$\frac{V_f(s)}{V_p(s)} = 1 - \frac{K_{FT} \lambda L s}{V_p(s) \cdot (s^2 + (K_{FT} + \lambda)s + K_{FT} \lambda)}. \quad (4-42)$$

The parameters K_{FT} and λ are chosen so that the system can satisfy the condition (4-42) for asymptotic stability. By choosing

$$K_{FT} = \omega_n (\xi + \sqrt{\xi^2 - 1}), \quad \lambda = \frac{\omega_n}{\xi + \sqrt{\xi^2 - 1}},$$

the control law (4-38) becomes

$$a_{FT} = a_p + 2\xi\omega_n \dot{e}_R + \omega_n^2 e_R, \quad (4-43)$$

where the gain ξ can be regarded as a damping ratio and set at 1 for critical damping, and ω_n is the bandwidth of the controller.

That is, the control law in (4-43) is to ensure not only the spacing error e_R to converge to zero, but also the spacing errors not to amplify down a two-car platoon [2, 5].

In the stop-and-go mode, the subject-vehicle has to keep spacing from the preceding-vehicle with a quicker response than that of ACC mode. Therefore, the desired control law in (4-27) which is derived from the sliding surface in (4-25) seems to be inadequate. We choose the following sliding surface defined on the error and error-variation

as

$$S_{S\&G} = -a_f + a_{f\max} \text{sat}\left(\frac{a_f + \dot{e}_R + \lambda e_R + \dot{R}_{des}}{a_{f\max}}\right) \quad (4-44)$$

In case of $|a_f + \dot{e}_R + \lambda e_R + \dot{R}_{des}| < a_{f\max}$, the sliding surface becomes

$$S_{S\&G} = \dot{e}_R + \lambda e_R + \dot{R}_{des} \quad (4-45)$$

The stability of the sliding surface in (4-45) is examined by setting $S_{S\&G}=0$, and the error dynamics is $e_R(t) = e^{-\lambda t} - \dot{R}_{des} / \lambda$. Thus, $S_{S\&G}$ is stable but not asymptotically since $e_R(t) \rightarrow \dot{R}_{des}(t) / \lambda$ as $t \rightarrow \infty$ which is bounded and can be reduced by choosing larger positive value of λ . Moreover, for steady-state car-following, the subject-vehicle maintains a constant speed or stops as the same as the preceding-vehicle such that $\dot{R}_{des} = \sigma a_f = 0$; the spacing error will approach zero, that is, $e_R \rightarrow 0$. We then choose the control law as

$$\dot{S}_{S\&G} = -K_{S\&G} S_{S\&G} \quad (4-46)$$

where $K_{S\&G} > 0$ is to guarantee the desired condition and asymptotic stability.

By virtue of (4-45) and (4-46), the desired acceleration is derived as

$$a_{S\&G} = \frac{1}{(1 + \lambda \sigma)} \left[K_{S\&G} (\dot{e}_R + \lambda e_R + \sigma a_f) + a_p + \lambda \dot{R} \right] \quad (4-47)$$

The sliding surface is

$$S_{S\&G} = -a_f \pm a_{f\max} \quad (4-48)$$

for $|a_f + \dot{e}_R + \lambda e_R + \dot{R}_{des}| \geq a_{f\max}$, and the desired acceleration is

$$a_{S\&G} = \frac{-\dot{a}_f}{K_{S\&G}} \pm a_{f\max} \quad (4-49)$$

We note that the jerk of the subject vehicle in (4-49) is still negligible ($a_{S\&G} = \pm a_{f\max}$). The acceleration of the preceding vehicle can be accessed by the double differential of the relative distance, i.e., $a_p = \ddot{R} + a_f$.

In the stop-and-go mode, the vehicle velocity is usually within 40 km/h. As a result, the headway time is chosen as 2.0 s such that the desired inter-vehicle distance will be sufficient to achieve the smooth response in maneuvering throttle and brake control.

In the second stage, the conversion from the desired acceleration into the desired velocity takes the form

$$\dot{V}_C = a_{fdes} - k_t (V_f - V_C), \quad (4-50)$$

where $k_t > 0$ is chosen to avoid sudden velocity-change from sensor noise in the measurement of spacing and vehicle velocity. To achieve real-time conversion, the differential equation in (4-50) is approximated by Euler's method,

$$V_C(k+1) = (1 - T_s k_t) V_C(k) + T_s (k_t V_f(k) + a_{f_{des}}(k)), k \geq 0 \quad (4-51)$$

The conversion (4-51) is able to adjust the aggressiveness of desired velocity from the desired acceleration by depending on the current velocity. A smooth reference trajectory of V_C can be generated. Note that the set-point of V_C is determined from the current velocity V_f and prohibited by the larger value of k_t , therefore the exceeding error between V_C and V_f can be prevented.

The autonomous switching scheme chooses the desired mode by min-operation

$$V_C(k+1) = \min \left\{ \begin{array}{l} (1 - T_s k_{CC}) V_C(k) + T_s (k_{CC} V_f(k) + a_{CC}(k)) \\ (1 - T_s k_{CF}) V_C(k) + T_s (k_{CF} V_f(k) + a_{CF}(k)) \end{array} \right. , a_{CF} = a_{ACC/FT} \text{ or } a_{S\&G} \quad (4-52)$$

The filtering gain k_t can be chosen differently, namely $k_t = k_{CC}$ for CC mode and $k_t = k_{CF}$ for car-following situation including both ACC and stop-and-go mode. The subject-vehicle drives in CC mode in general. It will automatically switch to ACC mode or stop-and-go mode once a valid-target vehicle is detected. This concept is identical to the Gipps model (see Appendix C) which is demonstrated to be capable of longitudinal human driving characteristics [48]. The Gipps model (C.1) determines the subject-vehicle's velocity by two halves of the equation: the first half tends to accelerate to the desired velocity, while the second half tends to keep a safe distance from the preceding-vehicle.

4.2.3. Regulation control

The objective of the regulation control is to execute the commanded speed from the supervisory control. Under different types of engine, automatic transmission in the gear box and brake system in each vehicle, a normal driver can still operate the throttle and brake systems easily to reach the suitable speed. In view of this, the design concept to the regulation brings from the human-driving behavior. By importing the human-driving experience into fuzzy rule, not only avoid the difficulty for control designing based on such complicated mathematical model, but we also make the system satisfy the humanlike driving behavior.

In constructing the fuzzy inference rules, we usually make different inference rules for every input variable. By choosing two fuzzy inputs as the speed error ($V_C - V_f$) and the error-change, if we set 5 membership functions for each input variable, then there will be 25 fuzzy rules in the whole fuzzy rule table. There will be a drawback that building many fuzzy rules will increase the computation load for implementation loop. Conventionally, we usually use a look-up-table to approximate a fuzzy rule table in programming. However, the method not only needs more storage space on the memory of device, but also causes discontinuous outputs which will worsen the controlling performance of original FLC. Therefore, a PD-based single-input fuzzy logic control (SFLC) is employed in the regulation control design.

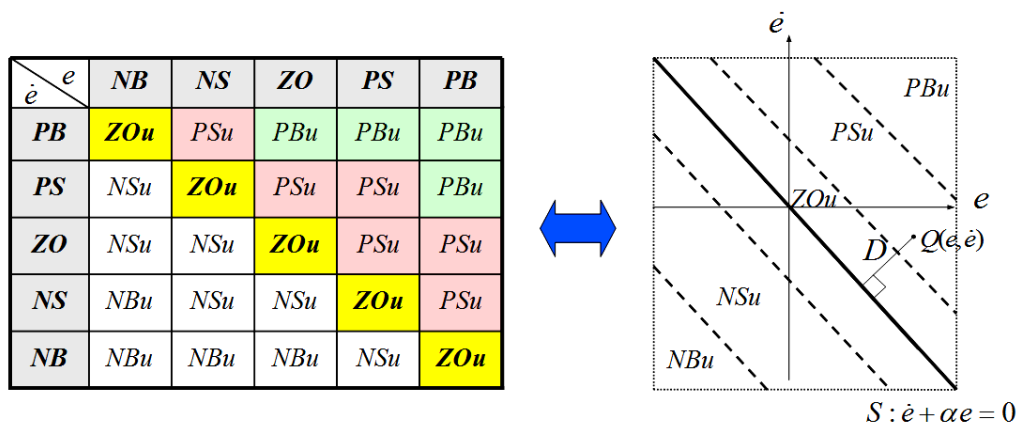


Fig. 4-7. Derivation of the signed distance.

For conventional FLC's, the fuzzy rule base is constructed in a two-dimension (2-D) space for using the error and error change phase-plane, i.e. (e, \dot{e}) . It can be inspected that most 2-D fuzzy rule bases have the so-called *skew-symmetric property* as shown in Fig. 4-7; thus, the

switching line which represents the main hyperplane of 2-D fuzzy rule table can be defined as:

$$S: \dot{e} + \alpha e = 0 \quad (4-53)$$

where α is the slope of the switching line.

The original fuzzy inputs of the error and error change can be replaced by one signed distance, which is defined as the perpendicular distance from an operating point $Q(e, \dot{e})$ to the projection point on the switching line S . As illustrated in Fig. 4-7, a new fuzzy input of the signed distance can be calculated as

$$\begin{aligned} D_s &= \text{sgn}(s) \cdot D \\ &= \text{sgn}(s) \cdot \frac{|\dot{e} + \alpha e|}{\sqrt{1 + \alpha^2}} = \frac{\dot{e} + \alpha e}{\sqrt{1 + \alpha^2}} \end{aligned} \quad (4-54)$$

where the sign function is

$$\text{sgn}(s) = \begin{cases} 1 & \text{for } s > 0 \\ -1 & \text{for } s \leq 0 \end{cases}$$

Now the fuzzy input D_s is a combination of speed error and error change with a proportional gain and a derivative gain, respectively,

$$D_s = k_p e + k_d \dot{e} \quad (4-55)$$

with $k_p = \alpha / \sqrt{1 + \alpha^2}$ and $k_d = 1 / \sqrt{1 + \alpha^2}$.

The associated fuzzy rule form is

$$R_k : \text{If } D_s \text{ is } LD_k, \text{ then } u \text{ is } LU_k. \quad (4-56)$$

where LD_k and LU_k are the linguistic term sets for the fuzzy input and output in the k th rule, respectively.

The fuzzy rule table of SFCLC is established as in Table 4-3. The membership functions of SFCLC are shown in Fig. 4-8. The total numbers of the fuzzy rules on throttle and brake control of the regulation control are only 5, which are much fewer than 25 fuzzy rules of 2-D fuzzy control such that the generation and tuning of rules are much easier. Especially, control effect of the PD-based SFCLC is equivalent to that of 2-D fuzzy control (details can be referred to [49]). In the defuzzication operation, the center of mass (COM) method is applied to calculate the control output

$$u^* = \frac{\sum_k^5 \mu_k(D_s) \times u_k}{\sum_k^5 \mu_k(D_s)} \quad (4-57)$$

where μ_k represents the weighting value of each rule k , and u_k is the crisp value of each rule consequence.

TABLE 4-3. Rule table of the SFLC.

D_s	NB	NS	ZO	PS	PB
u	NBu	NSu	ZOu	PSu	PBu

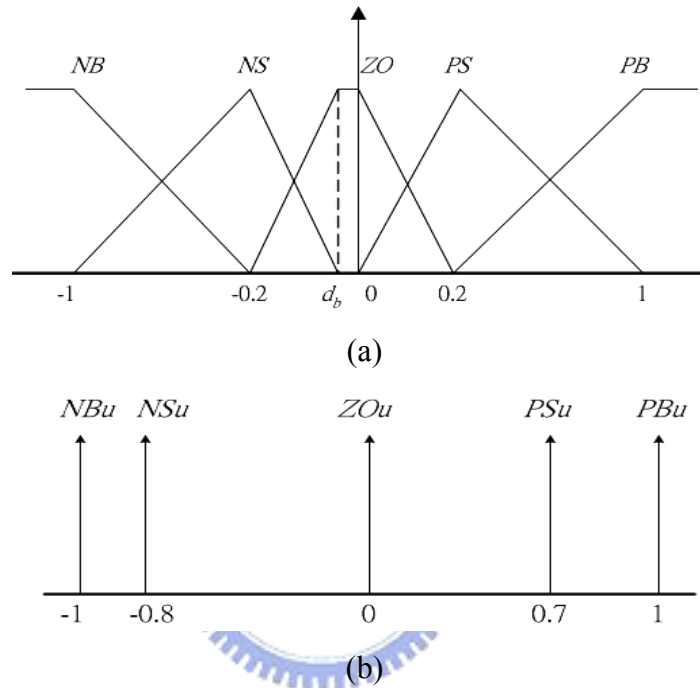


Fig. 4-8. Membership functions of (a) the fuzzy input and (b) the fuzzy output.

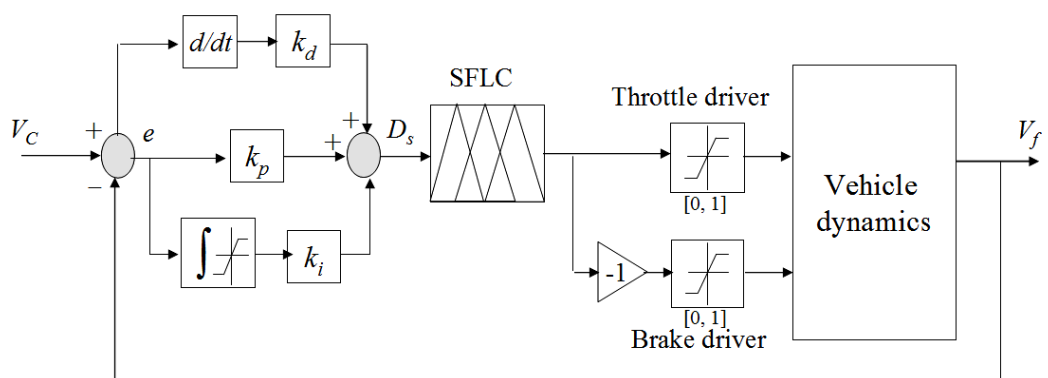


Fig. 4-9. Overall structure of the proposed regulation control structure.

Figure 4-9 shows the overall structure of the regulation control. To test the performance of our PD-based FLC, we consider the constant velocity-tracking case. We find that there always

exists a steady-state error (around 2.5 km/h) for the desired velocity-tracking (80 km/h), as shown in Fig. 4-10(a). This is possibly due to the grad of uphill-road and the friction between vehicle's rubber-tires and asphalt roads. Therefore, we add an integral controller with limited saturation [1, -1] to compensate this error. Figure 4-10(b) shows the improved performance of the proposed PID-based FLC.

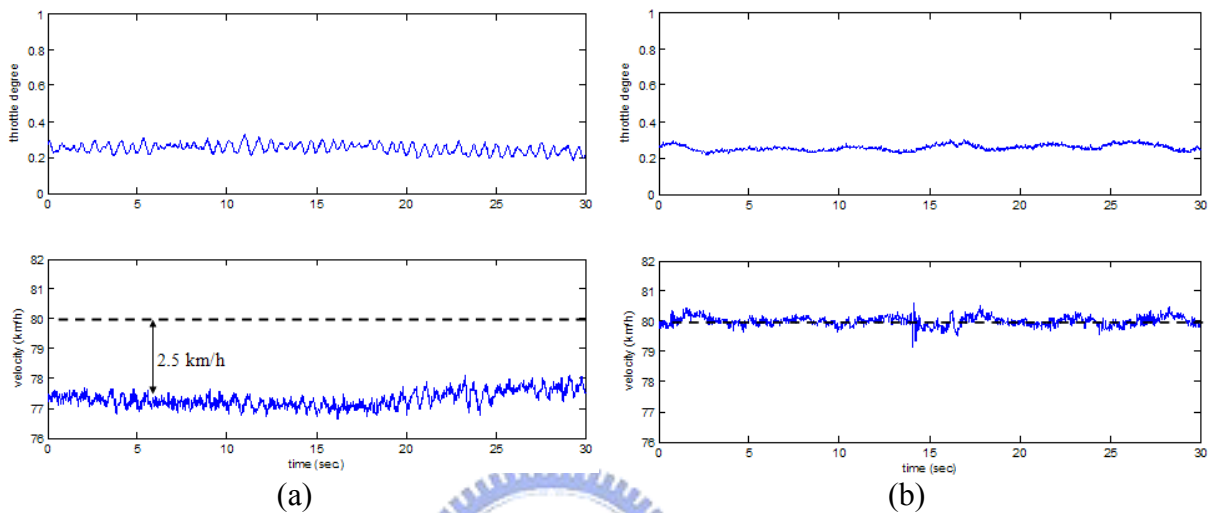


Fig. 4-10. Constant velocity-tracking performance for the proposed PD-based FLC (a) and PID-based FLC (b).

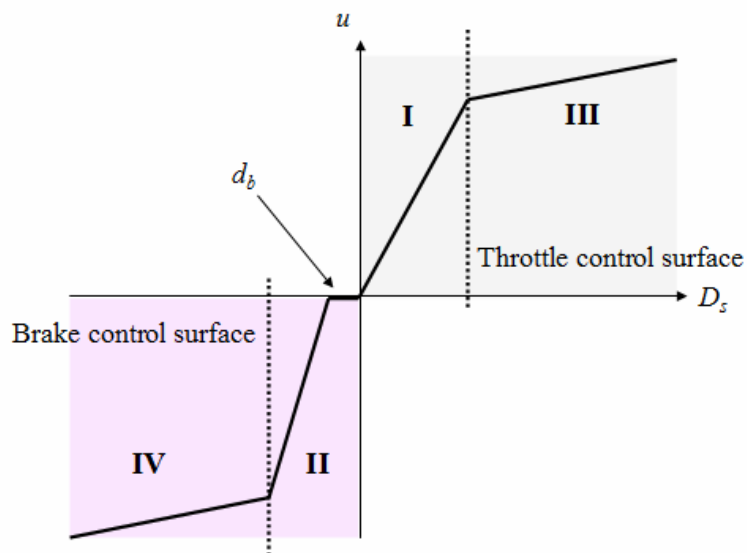


Fig. 4-11. Control surface of the single-input fuzzy control.

Further, the SFLC of the regulation control can be simplified into 5 linear equations from mapping between D_s and u . We can exploit the control-surface concept of SFLC, as shown in Fig. 4-11, which is the one-to-one mapping between the fuzzy inputs and outputs. Even if the

5 fuzzy inference rules and other process of fuzzy logic control such as fuzzifier and defuzzifier are substituted, the performance equals that of original SFCL. In this way, we can decrease a considerable quantity in the programming complexity of fuzzy inference. Note that the offset d_b (corresponding to the negative membership of ZO of Fig. 4-8(a)) presents the reachable deceleration for the vehicle due to the rolling resistance and the engine inertia, and can be obtained experimentally by

$$d_b = k_p \cdot T_s \cdot \Delta V_{ave} + k_d \frac{\Delta V_{ave}}{\Delta t} \quad (4-58)$$

where $\Delta V_{ave} < 0$ is the average speed variation during a interval Δt with throttle and brake being off.

Remark: The term of integral control is neglected in (4-58) due to the small values which are limited within [1, -1].

As to the switching strategy to implement the integrated control between throttle and brakes, it should be noted that the normalized universe of discourse of the driving voltage is limited to the range [0, 1] and negative voltages can not provide inverse torques from the throttle motor. Therefore, the negative voltage can be output into the brake driver for deceleration control. In other words, the SFCL is designed to provide a positive voltage (phase I and III in Fig. 4-11) with regard to acceleration for the throttle driver while provide a negative voltage (phase II and IV in Fig. 4-11) with regard to deceleration for the brake motor. By using an inverse operation, the negative voltage can be inverted to the brake motor. Due to this nature of input voltage to motor drivers, the switch between the throttle and the brake control can be directly constructed. As shown in Fig. 4-11, the switching strategy is summarized as follows:

— **Throttle control region.** For the case of $D_s > 0$, the summation of speed error and error change is positive and it implies that the throttle should be acted to achieve the desired speed.

— **Switching control region.** For the case of $0 < D_s < d_b$, the summation of speed error and error change is slightly negative. Only by engine brake, the speed can be decreased to the desired speed. In this region, neither throttle nor brake should be acted.

— **Brake control region.** For the case of $D_s < d_b$, the summation of speed error and error change is more negative and thus the brake should be acted to decrease the speed to achieve the lower desired speed.

As a result, only the throttle will be acted if the requested speed is greater than the current speed; otherwise, only the brake will be acted whenever the vehicle is required to be

decelerated ($D_s < d_b$). The situation of both throttle and brake being active can be prevented by the switch control region. Besides, the error change in D_s can improve the controlling response for instant variance in vehicle speed. A normal driver operates the brake pedal more rapidly than the throttle pedal, and thus in the design of SFLC the brake control surface (in phase II) is more sloping than that of throttle control surface (in phase I). In addition, the foot action for pressing the throttle/brake pedal initially is quick and then smooth in deeper position, and therefore the slopes in phase III and IV are smaller than that in phase I and II.



4.3. Collision Warning/Avoidance Maneuver

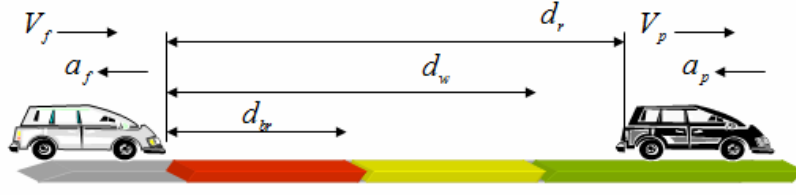


Fig. 4-12. Headway distance for car-following.

There are two stages in the CW/CA strategy. The first stage is the computation of warning distance for the normal warning situation. The second stage is the computation of braking distance for the guarantee of collision avoidance. It is possible for a driver to begin a driving collision avoidance maneuver earlier than a braking collision avoidance maneuver. Therefore, the CW/CA strategy should employ a non-conservative warning distance before that the driver begins the steering maneuver, and a conservative braking distance that if less than this distance, then the emergency steering maneuvers is started.

In Fig. 4-12, the dynamics of car-following is illustrated. Initially the headway distance between the preceding vehicle and the following vehicle is d_r . The preceding vehicle starts to brake with the deceleration a_p and its traveling distance to stop is $V_p^2/2a_p$. After the reaction time T_c of the driver and the brake actuator of the following vehicle, the traveling distance to stop with the deceleration a_f is $V_f T_c + V_f^2/2a_f$. Therefore, the anti-collision distance can be obtained as

$$d_w = V_f T_c + \left(\frac{V_f^2}{2a_f} - \frac{V_p^2}{2a_p} \right) \quad (4-59)$$

Note that the warning distance (4-59) is also definition of anti-collision distance in ISO 15263 [50] which is specified to CW/CA systems. As to the computation of the braking distance, the time-to-collision (TTC) braking distance is applied. The relative distance d_r dynamics at any time t between two vehicles can be presented as

$$d_r(t) = d_r(t_0) + (V_p(t_0) - V_f(t_0))(t - t_0) + \int_{t_0}^t \int_{t_0}^{\tau} (a_p(s) - a_f(s)) ds d\tau \quad (4-60)$$

where t_0 denotes the time at which the measurement of TTC is required.

When the time $t > t_0$ and $d_r(t)=0$, TTC can be obtained as $T_c = t - t_0$. Since the computation of TTC requires the profiles of deceleration for both preceding and following vehicle, here the assumptions of the maximum deceleration for the preceding vehicle and zero deceleration for the following vehicle are made, i.e., $a_p(t) = a_{\max}^-$, $a_f(t) = 0$. In the computation of d_{br} , TTC

can be viewed as the total delay which composes of the driver reaction time and the braking system actuation time, i.e., $T_c = \tau_{total} = \tau_{hum} + \tau_{sys}$. The braking distance can then be determined by the initial distance $d_r(t_0)$, and presented as

$$d_{br} = V_{rel} \tau_{total} + \frac{1}{2} a_{max}^- \tau_{total}^2 \quad (4-61)$$

where $V_{rel} = V_f - V_p$ are the relative velocity at initial time t_0 .

To avoid the discontinuity which exists in the switch between the warning distance and the braking distance, an evaluate signal based on the rational form is given as

$$I_w = \frac{d_r - d_{br}}{d_w - d_{br}} \quad (4-62)$$

Remark 1: The accelerations of the preceding and the following vehicle are both assumed with the same maximum values, and V_p is replaced by V_{rel} , then the warning distance defined in Eq. (4-59) can be rewritten as

$$d_w = V_f \tau_{total} + \left(\frac{V_f^2}{2a_{max}^-} - \frac{(V_f - V_{rel})^2}{2a_{max}^-} \right) + d_0 \quad (4-63)$$

The augmented offset d_0 is essential to be sure that $d_w - d_{br} > 0$; otherwise, the value of I_w will be positive for indicating safety while $d < d_{br}$. By examining the braking distance in (4-61) and the modified warning distance in (4-63), the low bound of d_0 shall be reasonably constrained to the value $a_{max}^- \tau_{total}^2 / 2$ such that $d_w > d_{br}$ is guaranteed.

Remark 2: The values for all parameters used in the CW/CA strategy can be referred to [50] in which the statistics are specified from many practical tests. The maximum deceleration for the preceding and the following vehicle are both given as 6 m/s^2 , and the delay time for the human and the braking system is chosen as 0.6 s and 0.2 s , respectively.

The evaluate signal in (4-62) can give a graded display about the event likelihood for the driver. The condition of $I_w > 1$ corresponds to $d_r > d_w$, and it denotes that the headway distance is safe for driving. The condition of $0 < I_w < 1$ corresponds to $d_{br} < d_r < d_w$, and this range can be divided into several graded degrees for warnings. If $I_w \leq 0$, then this condition corresponds to $d_r \leq d_{br}$ and the emergency braking should immediately be acted.

The next issue is to define the graded degrees for condition $0 < I_w < 1$. In research on traffic conflicts techniques, TTC has proven to be an effective measure for rating the severity of

collision [51]. In general, only encounters with a minimum TTC less than 2 s are considered as a critical situation for drivers. Therefore, here we can compute the I_w corresponding to TTC while the critical situation is encountered. By substituting (4-61) and (4-63) into (4-62), and considering the critical braking for the preceding vehicle ($V_p \rightarrow 0$), the warning evaluate signal can be rewritten as

$$I_w = \frac{d_r - V_f \tau_{total} - a_{max}^- \tau_{total}^2 / 2}{V_f^2 / 2a_{max}^-} \quad (4-64)$$

By arranging (4-64) into the following equation,

$$\frac{d_r}{V_f} = \tau_{total} + \frac{a_{max}^- \tau_{total}^2}{2V_f} + \frac{V_f}{2a_{max}^-} I_w \quad (4-65)$$

The left term is the definition for TTC (as $V_p = 0$), and we can obtain the relation between TTC and I_w under different velocities, as shown in Fig. 4-13.

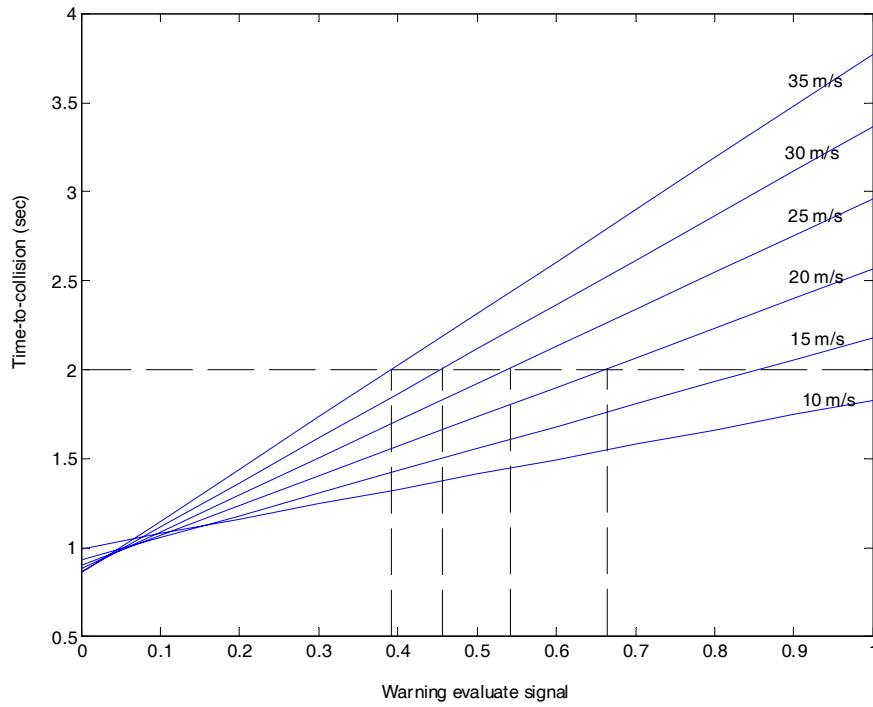


Fig. 4-13. The relation between the TTC and the warning evaluate signal with respect to different velocities.

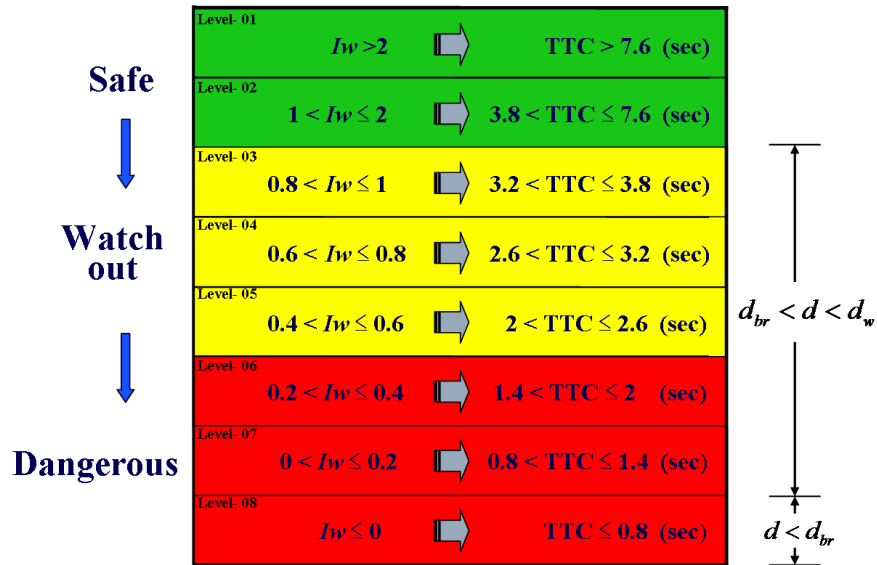


Fig. 4-14. Warning degree in three zones.

With the increased driving velocity, $TTC=2$ s corresponds to less order of the warning evaluate signal. The order 0.4 which represents $TTC=2$ s at the high velocity 35 m/s (=126 km/h) is then chosen as the indication from normal situation to critical situation. In order to characterize different warning levels, three zones in Fig. 4-14 are defined as

- *Green zone*: $I_w > 1$: the current inter-distance d is larger than the warning distance d_w . This is safe range for car-following operation.
- *Yellow zone*: $0.4 < I_w \leq 1$: the current inter-distance d_r is smaller than d_w . This range indicates the driver that the following distance is not safe and the vehicle should be decelerated.
- *Red zone*: $I_w \leq 0.4$: the current inter-distance d_r reaches the braking distance d_{br} . In this range, the braking should be immediately applied to avoid collision with the preceding vehicle.

Chapter 5

Combined Longitudinal and Lateral Control Design

5.1. Nonlinear Vehicle Longitudinal and Lateral Coupling Dynamics

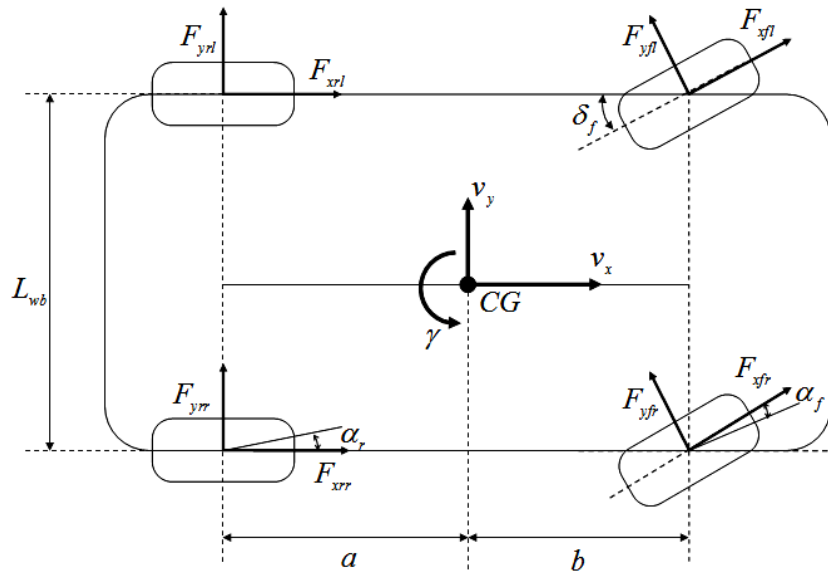


Fig. 5-1. 3-DOF vehicle model.

By considering a vehicle moving over a flat and level road surfaces, the 3 degrees-of-freedom (DOF) vehicle dynamics is represented by the longitudinal velocity v_x , the lateral velocity v_y , and the yaw rate γ , as shown in Fig. 5-1. The 3 DOF dynamics, including aerodynamic terms in the vehicle dynamics, is depicted as

$$m\dot{v}_x = F_{xr} + F_{xf} \cos \delta_f - F_{yf} \sin \delta_f + m\gamma v_y - k_D v_x^2 \quad (5-1)$$

$$m\dot{v}_y = F_{yr} + F_{xf} \sin \delta_f + F_{yf} \cos \delta_f - m\gamma v_x \quad (5-2)$$

$$I_z \dot{\gamma} = aF_{xf} \sin \delta_f + aF_{yf} \cos \delta_f - bF_{yr} + \frac{L_{wb}}{2} (\Delta F_{xr} + \Delta F_{xf} \cos \delta_f) \quad (5-3)$$

with

$$F_{xf} = F_{xfr} + F_{xfl}, \quad F_{xr} = F_{xrr} + F_{xrl}$$

$$\Delta F_{xf} = F_{xfr} - F_{xfl}, \quad \Delta F_{xr} = F_{xrr} - F_{xrl}$$

Although not shown, the model (5-1)-(5-3) used here also includes quasi-static compensation for the effect of roll and pitch on tire vertical forces [52]. Compensation for roll and pitch effects can be calculated as a function of center of gravity height with lateral acceleration, and longitudinal acceleration, respectively. For simplicity of control design, it is assumed that the vehicle body is symmetric about the longitudinal plane such as the differential forces of tires can be eliminated, i.e., $\Delta F_{xf} = \Delta F_{xr} = 0$, and equal slip angles on the left and right tires can be approximated as

$$\alpha_f = \tan^{-1} \left(\frac{v_y + \gamma a}{v_x} \right) - \delta_f \quad (5-4)$$

$$\alpha_r = \tan^{-1} \left(\frac{v_y - \gamma b}{v_x} \right) \quad (5-5)$$

By using a linear tire model, the lateral forces are given as

$$F_{yf} = -C_f \alpha_f \quad (5-6)$$

$$F_{yr} = -C_r \alpha_r \quad (5-7)$$

In addition, the longitudinal forces of tires can be written as

$$F_{xf} = F_T - \frac{b}{a+b} f(mg - k_L v_x^2) \quad (5-8)$$

$$F_{xr} = -\frac{a}{a+b} f(mg - k_L v_x^2) \quad (5-9)$$

Substituting the expressions in (5-4) through (5-9) and making small angle approximation can yield

$$\begin{aligned} m\dot{v}_x = & m\gamma v_y + \left(F_T - \frac{b}{a+b} f(mg - k_L v_x^2) \right) \cos \delta_f \\ & - \frac{a}{a+b} f(mg - k_L v_x^2) + C_f \left(\frac{v_y + \gamma a}{v_x} - \delta_f \right) \sin \delta_f - k_D v_x^2 \end{aligned} \quad (5-10)$$

$$\begin{aligned} m\dot{v}_y = & -m\gamma v_x + \left(F_T - \frac{b}{a+b} f(mg - k_L v_x^2) \right) \sin \delta_f \\ & - C_f \left(\frac{v_y + \gamma a}{v_x} - \delta_f \right) \sin \delta_f - C_r \left(\frac{v_y - \gamma b}{v_x} \right) \end{aligned} \quad (5-11)$$

$$\begin{aligned} I_z \dot{\gamma} = & a \left(F_T - \frac{b}{a+b} f(mg - k_L v_x^2) \right) \sin \delta_f \\ & - a C_f \left(\frac{v_y + \gamma a}{v_x} - \delta_f \right) \cos \delta_f + b C_r \left(\frac{v_y - \gamma b}{v_x} \right) \end{aligned} \quad (5-12)$$

By assuming a vehicle has throttle, brake, and steer-by-wire capabilities so that steering,

braking and two driving wheels can be controlled, the equations then can be rewritten as

$$M\dot{q} = \dot{h}(q) + g(q, u_c) \quad (5-13)$$

where $q = [v_x \ v_y \ \gamma]^T$ and the control vector $u_c = [F_T \ \delta_f]^T$; M is the positive definite mass matrix, $\dot{h}(q)$ contains the terms without influence of control inputs, and $g(q, u_c)$ has the remaining controlled terms as follows

$$M = \text{diag}(m, m, I_z) \quad (5-14)$$

$$\dot{h}(q) = \begin{bmatrix} mv_y \gamma + \left(\frac{a}{a+b} f k_L - k_D \right) v_x^2 \\ -mv_x \gamma - C_r \left(\frac{v_y - b\gamma}{v_x} \right) \\ bC_r \left(\frac{v_y - b\gamma}{v_x} \right) \end{bmatrix} \quad (5-15)$$

$$g(q, u_c) = \begin{bmatrix} \left(F_T - \frac{b}{a+b} f(mg - k_L v_x^2) \right) \cos \delta_f + C_f \left(\frac{v_y + a\gamma}{v_x} - \delta_f \right) \sin \delta_f - \frac{afmg}{a+b} \\ \left(F_T - \frac{b}{a+b} f(mg - k_L v_x^2) \right) \sin \delta_f - C_f \left(\frac{v_y + a\gamma}{v_x} - \delta_f \right) \cos \delta_f \\ a \left(F_T - \frac{b}{a+b} f(mg - k_L v_x^2) \right) \sin \delta_f - aC_f \left(\frac{v_y + a\gamma}{v_x} - \delta_f \right) \cos \delta_f \end{bmatrix} \quad (5-16)$$

The controlled terms, $g(q, u_c)$ are set equal to the desired control forces, and this set of equations can then be used to solve for the control vector, u_c .

The dynamics in (5-14) through (5-16) are in terms of absolute states which are defined with respect to a fixed world reference coordinate. However, the interesting aspect of vehicle automation control is the forward velocity, relative lateral offset and heading angle between the vehicle's CG and the road centerline. The yaw error ψ_e is the deviation between the heading angle ψ and the desired heading ψ_d of the local tangent to the roadway with respect to an arbitrary reference direction. The rate of change of ψ_d can be approximated by the multiplication of longitudinal velocity of vehicle with the reference curvature, that is, $\dot{\psi}_d = v_x \rho_r$. Note that a straight road is represented as a road with zero curvature ($\rho_r = 0$).

Thus, the rate of change of yaw error can be given by

$$\dot{\psi}_e = \gamma - v_x \rho_r \quad (5-17)$$

The lateral displacement y_e is the distance from the road center to the sensor mounted at a distance d_s ahead of the mass center of the vehicle, and can be approximated by

$$y_e = y_{cg} + d_s \psi_e \quad (5-18)$$

where y_{cg} is the lateral distance between the vehicle's CG and the centerline of the road.

By differentiating (5-18) and substituting $\dot{\psi}_e$ from (5-17), we can obtain

$$\begin{aligned} \dot{y}_e &= \dot{y}_{cg} + d_s (\gamma - v_x \rho_r) \\ &= v_y + v_x \psi_e + d_s (\gamma - v_x \rho_r) \end{aligned} \quad (5-19)$$

Here we assume the forward velocity is approximately the longitudinal velocity, and both v_y/v_x (this is the sideslip angle of the vehicle CG) and ψ_e are small. In this chapter, except for the longitudinal velocity v_x , the other output measurements of interest are the yaw rate γ and the lateral displacement y_e of vehicle.



5.2. T-S Fuzzy Modeling for Nonlinear Vehicle Dynamics

The approach of using sector nonlinearity guarantees an exact T-S fuzzy model construction. Figure 5-2 illustrates the idea of the global sector nonlinearity approach, in which the aim is to find the sector such that $x = f(x) \in [a_1 \ a_2]x$.

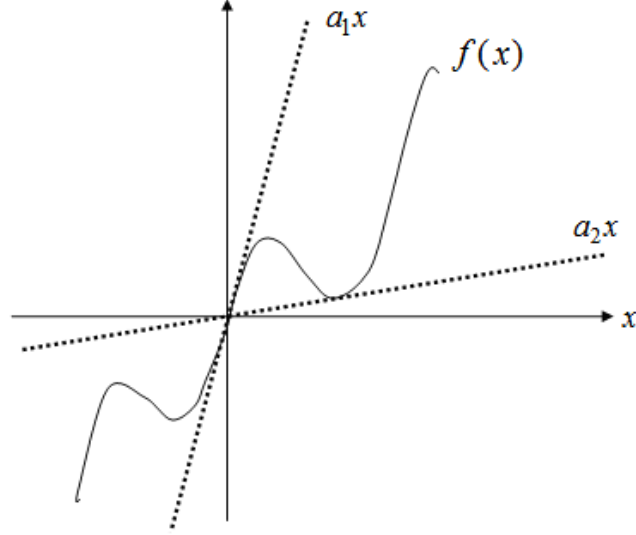


Fig. 5-2. Global sector nonlinearity.

Sometimes it is difficult to find global sectors for general nonlinear systems, therefore, the local sector nonlinearity is considered reasonably as the variables of physical systems are always bounded. Besides, the coupling effect between the inputs of traction force and steering angle is also an arduous problem to the modeling procedure. To overcome this difficult, here we adopt a decomposition transformation so called *virtual-inputs* instead of real inputs of vehicle dynamics as presented as

$$\delta_T = \left(F_T - \frac{b}{a+b} f(mg - k_L v_x^2) \right) \cos \delta_f + C_f \left(\frac{v_y + a\gamma}{v_x} - \delta_f \right) \sin \delta_f - \frac{afmg}{a+b} \quad (5-20)$$

$$T_\delta = \left(F_T - \frac{b}{a+b} f(mg - k_L v_x^2) \right) \sin \delta_f - C_f \left(\frac{v_y + a\gamma}{v_x} - \delta_f \right) \cos \delta_f \quad (5-21)$$

By considering the nonlinear vehicle dynamics (5-13) with the virtual inputs and the augmented sensory kinematics, equations (5-13) with (5-17) through (5-20) can be rewritten as

$$\dot{q}_s = h_s(q_s) + g_s(\delta_T, T_\delta) + D\rho_r \quad (5-22)$$

where $q_s = [q^T, y_e, \psi_e]^T \in R^{5 \times 1}$, is the augmented fifth order state vector,

$$\begin{aligned} \hat{h}_s(q_s) &= \begin{bmatrix} M^{-1}\hat{h}(q) \\ v_y + d_s \gamma + v_x \psi_e \\ \gamma \end{bmatrix}, \\ g_s(\delta_r, T_\delta) &= \begin{bmatrix} m^{-1} & 0 & 0 & 0 & 0 \\ 0 & m^{-1} & a/I_z & 0 & 0 \end{bmatrix}^T \begin{bmatrix} \delta_r \\ T_\delta \end{bmatrix}, \\ D &= [0 \ 0 \ 0 \ -d_s v_x \ -v_x]^T, \end{aligned}$$

and the remaining terms are defined the same as in the previous section. Here the road curvature in (5-22) can be viewed as an external disturbance to the vehicle system.

To obtain the corresponding T-S fuzzy model to the vehicle model (5-22) without consideration of disturbance, the three premise fuzzy variables are defined as

$$\begin{aligned} z_1(t) &= v_x(t) \\ z_2(t) &= \gamma(t) \\ z_3(t) &= v_x^{-1}(t) \end{aligned}$$

where $v_x(t) \in [U_{\min}, U_{\max}]$ m/s and $\gamma(t) \in [R_-, R_+]$ rad/s. From the maximum and minimum values of z_1, z_2 , and z_3 , each membership function can be presented as

$$h_{11}(z_1(t)) = \frac{z_1(t) - U_{\min}}{U_{\max} - U_{\min}}, \quad h_{12}(z_1(t)) = \frac{U_{\max} - z_1(t)}{U_{\max} - U_{\min}} \quad (5-23)$$

$$h_{21}(z_2(t)) = \frac{z_2(t) - R_-}{R_+ - R_-}, \quad h_{22}(z_2(t)) = \frac{R_+ - z_2(t)}{R_+ - R_-} \quad (5-24)$$

$$h_{31}(z_3(t)) = \frac{z_3(t) - U_{\max}^{-1}}{U_{\min}^{-1} - U_{\max}^{-1}}, \quad h_{32}(z_3(t)) = \frac{U_{\min}^{-1} - z_3(t)}{U_{\min}^{-1} - U_{\max}^{-1}} \quad (5-25)$$

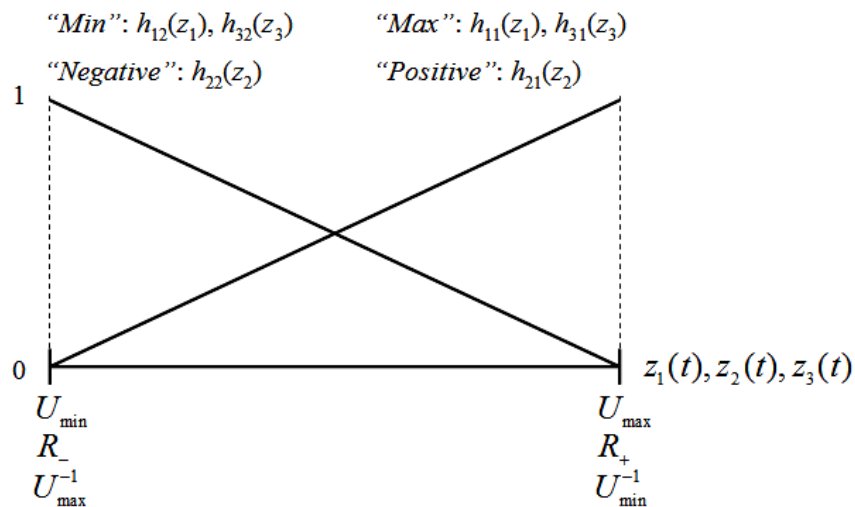


Fig. 5-3. Membership functions for z_1, z_2 , and z_3 .

We name the membership functions “*Max*”, “*Min*”, “*Positive*”, and “*Negative*”, respectively, and Fig. 5-3 shows these membership functions. Thus, the T-S fuzzy model for the vehicle system in (5-22) is given by the following eight-rule fuzzy model:

Plant Rule 1:

If z_1 is “*Max*” and z_2 is “*Positive*” and z_3 is “*Max*”,
then $\dot{X} = A_1X + B_1U$
 $Y = CX$,

Plant Rule 2:

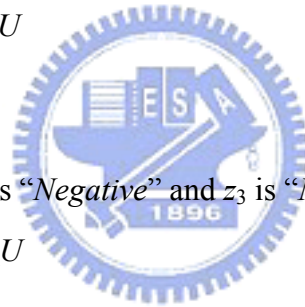
If z_1 is “*Min*” and z_2 is “*Positive*” and z_3 is “*Max*”,
then $\dot{X} = A_2X + B_2U$
 $Y = CX$,

Plant Rule 3:

If z_1 is “*Max*” and z_2 is “*Negative*” and z_3 is “*Max*”,
then $\dot{X} = A_3X + B_3U$
 $Y = CX$,

Plant Rule 4:

If z_1 is “*Min*” and z_2 is “*Negative*” and z_3 is “*Max*”,
then $\dot{X} = A_4X + B_4U$
 $Y = CX$,



Plant Rule 5:

If z_1 is “*Max*” and z_2 is “*Positive*” and z_3 is “*Min*”,
then $\dot{X} = A_5X + B_5U$
 $Y = CX$,

Plant Rule 6:

If z_1 is “*Min*” and z_2 is “*Positive*” and z_3 is “*Min*”,
then $\dot{X} = A_6X + B_6U$
 $Y = CX$,

Plant Rule 7:

If z_1 is “*Max*” and z_2 is “*Negative*” and z_3 is “*Min*”,
then $\dot{X} = A_7X + B_7U$
 $Y = CX$,

Plant Rule 8:

If z_1 is “Min” and z_2 is “Negative” and z_3 is “Min”,

$$\begin{aligned} \text{then } \dot{X} &= A_8 X + B_8 U \\ Y &= CX. \end{aligned} \quad (5-25)$$

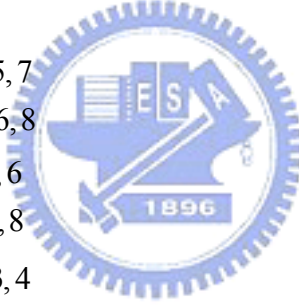
where $X = [v_x, v_y, \gamma, y_e, \psi_e]^T$, $U = [\delta_r, T_\delta]^T$, $Y = [v_x, \gamma, y_e]^T$,

$$A_i = \begin{bmatrix} \frac{1}{m} \left(\frac{afk_L}{a+b} - k_D \right) \bar{z}_1 & \bar{z}_2 & 0 & 0 & 0 \\ -\bar{z}_2 & -\frac{C_r}{m} \bar{z}_3 & \frac{C_r b}{m} \bar{z}_3 & 0 & 0 \\ 0 & \frac{bC_r}{I_z} \bar{z}_3 & -\frac{b^2 C_r}{I_z} \bar{z}_3 & 0 & 0 \\ 0 & 1 & d_s & 0 & \bar{z}_1 \\ 0 & 0 & 1 & 0 & 0 \end{bmatrix}, \quad B_i = \begin{bmatrix} \frac{1}{m} & 0 \\ 0 & \frac{1}{m} \\ 0 & \frac{a}{I_z} \\ 0 & 0 \\ 0 & 0 \end{bmatrix},$$

$$C = \begin{bmatrix} 1 & 0 & 0 & 0 & 0 \\ 0 & 0 & 1 & 0 & 0 \\ 0 & 0 & 0 & 1 & 0 \end{bmatrix},$$

and

$$\begin{aligned} \bar{z}_1 &= \begin{cases} U_{\max}, & i = 1, 3, 5, 7 \\ U_{\min}, & i = 2, 4, 6, 8 \end{cases} \\ \bar{z}_2 &= \begin{cases} R_+, & i = 1, 2, 5, 6 \\ R_-, & i = 2, 3, 7, 8 \end{cases} \\ \bar{z}_3 &= \begin{cases} U_{\min}^{-1}, & i = 1, 2, 3, 4 \\ U_{\max}^{-1}, & i = 5, 6, 7, 8 \end{cases} \end{aligned}$$



By the defuzzification process, the overall fuzzy model is inferred as

$$\dot{X}(t) = \sum_{i=1}^8 h_i(z(t)) (A_i X + B_i U) \quad (5-26)$$

$$Y(t) = \sum_{i=1}^8 h_i(z(t)) CX(t), \quad (5-27)$$

where h_i is the weight of the i -th rule and is calculated by the membership values as

$$\begin{aligned} h_1(t) &= h_{11}(z_1(t)) \times h_{21}(z_2(t)) \times h_{31}(z_3(t)) \\ h_2(t) &= h_{21}(z_1(t)) \times h_{21}(z_2(t)) \times h_{31}(z_3(t)) \\ h_3(t) &= h_{11}(z_1(t)) \times h_{22}(z_2(t)) \times h_{31}(z_3(t)) \\ h_4(t) &= h_{21}(z_1(t)) \times h_{22}(z_2(t)) \times h_{31}(z_3(t)) \\ h_5(t) &= h_{11}(z_1(t)) \times h_{21}(z_2(t)) \times h_{32}(z_3(t)) \\ h_6(t) &= h_{21}(z_1(t)) \times h_{21}(z_2(t)) \times h_{32}(z_3(t)) \end{aligned}$$

$$h_7(t) = h_{11}(z_1(t)) \times h_{22}(z_2(t)) \times h_{32}(z_3(t))$$

$$h_8(t) = h_{21}(z_1(t)) \times h_{22}(z_2(t)) \times h_{32}(z_3(t)).$$

Note that the values of h_i is in the range of $[0, 1]$.



5.3. Fuzzy Automated Driving Control Design

Before designing the automated driving controller, it should be noted that the order of the inputs (δ_T, T_δ) in the vehicle fuzzy model is too larger than states X . Thus it is necessary to scale the order of state vector and input vector appropriately so that which elements have similar numerical variations. Referring to the T-S fuzzy system (5-25), we define

$$X' = S_x X \quad \text{and} \quad U' = S_U U$$

and choose $S_x = \text{diag}\{0.1, 1, 1, 1, 1\}$ and $S_U = 1e-5$. Substituting the amplitude-scaling relations into the fuzzy system (5-25), it yields each subsystem

Plant Rule i :

If z_1 is F_{1i} and z_2 is F_{2i} and z_3 is F_{3i} ,

then $\dot{X}' = A'_i X' + B'_i U'$

$$Y' = C X', \quad (5-28)$$

where $A'_i = S_x^{-1} A_i S_x$, $B'_i = S_x B_i S_U^{-1}$, $i = 1, \dots, 8$.



5.3.1. Fuzzy Controller Design

The problem of optimal fuzzy vehicle tracking control is to design a rule-based nonlinear fuzzy inference form of

R_i : If z_1 is F_{1i} and z_2 is F_{2i} and z_3 is F_{3i} ,

then $U(t) = r_i(t)$, $i=1, \dots, 8$. (5-29)

such that the quadratic cost function,

$$J(u(\cdot)) = \int_{t_0}^{\infty} [U^T(t) S U(t) + X^T(t) L_1 X(t) + (Y(t) - Y_d(t))^T L_2 (Y(t) - Y_d(t))] dt \quad (5-30)$$

can be minimized; where $L_1 = [I_n - C^T (C C^T)^{-1} C]^T L_3 [I_n - C^T (C C^T)^{-1} C]$; S , L_2 , and L_3 is $n \times n$ nonnegative symmetric matrix with appropriate dimensions; $X^T(t) L_1 X(t)$ is the state trajectory penalty to produce smooth response; $U^T(t) S U(t)$ is fuel consumption; and the last term in (5-30) is related to tracking error cost.

Moreover, the performance index in (5-30) can be rewritten as

$$J(u(\cdot)) = \int_{t_0}^{\infty} [U^T(t) S U(t) + (X(t) - X_d(t))^T L (X(t) - X_d(t))] dt \quad (5-31)$$

where $L=L_1 + C^T L_2 C$ and the desired state trajectory $X_d(t)=C^T(CC^T)^{-1}Y_d(t)$.

By defining the error state $e_X = X-X_d$, its variation with regard to the fuzzy subsystem can be obtained as

$$\begin{aligned}\dot{e}_X(t) &= \dot{X}(t) - \dot{X}_d(t) \\ &= (A_i X(t) + B_i U(t)) - \dot{X}_d \\ &= A_i(X(t) - X_d(t)) + B_i U(t) + A_i X_d(t) - \dot{X}_d(t) \\ &= A_i e_X(t) + B_i U(t) + (A_i X_d(t) - \dot{X}_d(t))\end{aligned}\quad (5-32)$$

Here the desired states X_d is assumed to be the solution of

$$\dot{X}_d(t) = \sum_{i=1}^8 h_i(z(t)) A_i X_d(t) \quad (5-33)$$

Therefore, the tracking problem to the desired states can be converted into the regulation problem of the error state. Note that this assumption is based on that the vehicle dynamics should be taken into account of the specification of the desired states. If the given desired states cannot satisfy the condition of (5-33), it would be improper for the tracking targets.

The optimal global decisions $U^*(t)$ from $t = t_0$ to $t = \infty$ can be regarded as a series of optimal global decision based on the following successively on-going local quadratic optimal issue with the initial state resulting from the previous decision. Given the fuzzy system as

R_i : If z_1 is F_{1i} and z_2 is F_{2i} and z_3 is F_{3i} ,

$$\text{then } \dot{e}_X(t) = A_i e_X(t) + B_i r_i(t), \quad i = 1, \dots, 8 \quad (5-34)$$

with the initial error state resulting from the previous decision, i.e., $e_X(0)=e_X^*(0)$,

(1) find the optimal local decision $r_i^*(t)$, for minimizing the cost function,

$$J(u(\cdot)) = \int_{t_0}^{\infty} (r_i^T(t) S r_i(t) + e_X(t)^T L e_X(t)) dt \quad (5-35)$$

(2) obtain the optimal global decision $u^*(t)$, for minimizing the cost function $J(u(\cdot))$ in (5-31) by fuzzily blending each local decision, i.e.,

$$u^*(t) = \sum_{i=1}^8 h_i(z(t)) r_i^*(t) \quad (5-36)$$

Note that the next decision initial state is obtained by

$$\dot{e}_X^*(t) = \sum_{i=1}^8 h_i(z(t)) (A_i e_X^*(t) + B_i r_i^*(t)) \quad (5-37)$$

since there exists the one-to-one relationship between each fuzzy subsystem and the corresponding fuzzy controller. Furthermore, solving the optimal fuzzy control problem for each fuzzy subsystem can be achieved by simply generalizing the classical linear quadratic

theorem from the deterministic case to fuzzy case. Therefore, the following optimal fuzzy control design for the T-S fuzzy system (5-34) can be employed.

For the T-S fuzzy system in (5-34) and the fuzzy controller in (5-29), if (A_i, B_i) is C.C. and (A_i, C_i) is C.O., for $i=1, \dots, 8$, then fuzzy controller is designed as

Controller Rule i :

$$\begin{aligned} & \text{If } z_1 \text{ is } F_{1i} \text{ and } z_2 \text{ is } F_{2i} \text{ and } z_3 \text{ is } F_{3i}, \\ & \text{then } r_i^*(t) = -B_i^T \bar{\pi}_i^c e_X^*(t), i = 1, \dots, 8 \end{aligned} \quad (5-38)$$

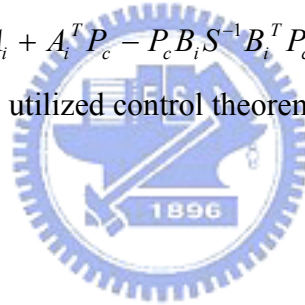
then, fuzzily blending global optimal fuzzy controller is formed as

$$\begin{aligned} U^*(t) &= \sum_{i=1}^8 h_i(z(t)) [-B_i^T \bar{\pi}_i^c e_X^*(t)] \\ &= \sum_{i=1}^8 h_i(z(t)) [-K_i^c e_X^*(t)] \end{aligned} \quad (5-39)$$

which minimizes $J(u(\cdot))$ in (5-30), where $\bar{\pi}_i^c$ is the unique symmetric positive semi-definite solution of the steady-state Riccati equation (S.S.R.E.)

$$P_c A_i + A_i^T P_c - P_c B_i S^{-1} B_i^T P_c + L = 0 \quad (5-40)$$

The detailed description for the utilized control theorem can be referred to [26, 27].



5.3.2. Fuzzy Observer Design

The fuzzy control design introduced above requires all states feedback in each local linear controller. In practice, all states of the system can not be directly measured, lateral velocity and yaw error especially, such that a fuzzy observer is developed to observe states of T-S vehicle fuzzy model.

The objective of fuzzy observer requires

$$X(t) - \hat{X}(t) \rightarrow 0, \quad t \rightarrow \infty$$

where $\hat{X}(t)$ denotes the state vector which is estimated by a fuzzy observer.

For the fuzzy observer design, it is assumed that the fuzzy system (5-28) is locally observable, i.e., (A_i, C_i) is C.O., for $i=1, \dots, 8$. The fuzzy observer is designed as

Observer Rule i :

$$\begin{aligned} & \text{If } z_1 \text{ is } F_{1i} \text{ and } z_2 \text{ is } F_{2i} \text{ and } z_3 \text{ is } F_{3i}, \\ & \text{then } \dot{\hat{X}}(t) = A_i \hat{X}(t) + B_i U(t) + L_i^o (Y(t) - \hat{Y}(t)), \end{aligned}$$

$$\hat{Y}(t) = C\hat{X} \quad i = 1, \dots, 8 \quad (5-41)$$

where L_i^o ($i = 1, 2, \dots, 8$) are the local gains to be determined by the design of the fuzzy observer, Y and $\hat{Y}(t)$ are the final output of the fuzzy system and the fuzzy observer, respectively.

By applying the separation property, the fuzzy observer can be designed in a way similar to the fuzzy control for each rule of the T-S fuzzy system to provide an optimal estimate of the state $\hat{X}(t)$. The T-S fuzzy system is supposed to be a plant with a known control input $U(t)$, a measured output, $Y(t)$, and white process noise and measurement noise, $w(t)$ and $v(t)$, with known power spectral densities, W (positive semi-definite matrix) and V (positive definite matrix). The fuzzy observer gain can be obtained as

$$L_i^o = \bar{\pi}_i^o C^T V^{-1} \quad (5-42)$$

where $\bar{\pi}_i^o$ is the covariance matrix which satisfies the following steady-state Riccati equation (S.S.R.E.)

$$P_o A_i^T + A_i P_o - P_o C^T V^{-1} C P_o + F W F^T = 0 \quad (5-43)$$

where F is the noise coefficient matrix.

As shown in (5-41), the fuzzy observer has the linear state observer's laws in each consequent rule. The overall fuzzy observer is presented as

$$\dot{\hat{X}}(t) = \sum_{i=1}^8 h_i(z(t)) \left[A_i \hat{X}(t) + B_i U(t) + L_i^o (Y(t) - \hat{Y}(t)) \right] \quad (5-44)$$

and the final output of the fuzzy observer is

$$\hat{Y}(t) = \sum_{i=1}^8 h_i(z(t)) C \hat{X}(t) \quad (5-45)$$

Note that the same weight h_i as the weight of i -th rule of the fuzzy system (5-26) and controller (5-38) is used.

With the final estimated state $\hat{X}(t)$, the fuzzy controller in (5-38) and (5-39) can be rewritten as

Controller Rule i :

If z_1 is F_{1i} and z_2 is F_{2i} and z_3 is F_{3i} ,

$$\text{then } r_i(t) = -K_i^c (\hat{X}(t) - X_d(t)), i = 1, \dots, 8 \quad (5-46)$$

By setting $\hat{e}_x(t) = \hat{X}(t) - X_d(t)$ and substituting (5-46) into (5-38) and (5-41), the observer-based fuzzy controller can be represented as

$$\begin{cases} U(t) = \sum_{i=1}^8 h_i(z(t))[-B_i^T \bar{\pi}_i \hat{e}_X] \\ \dot{\hat{X}}(t) = \sum_{i=1}^8 h_i(z(t))[(A_i - B_i K_i^c - L_i^o C)\hat{X}(t) + B_i K_i^c X_d(t) + L_i^o Y(t)] \end{cases} \quad (5-47)$$

The actual control inputs to the vehicle system are the net force F_T of traction/braking extended on four tires and the steering angle δ_f . Given $U = [\delta_T, T_\delta]^T$, the actual controlling vector $u_c = [F_T \ \delta_f]^T$ can be solved by Eqs. (5-20) and (5-21) which can be rewritten as

$$\delta_T = F_{xf} \cos \delta_f - F_{yf} \sin \delta_f - \frac{afmg}{a+b} \quad (5-48)$$

$$T_\delta = F_{xf} \sin \delta_f + F_{yf} \cos \delta_f \quad (5-49)$$

From (5-49) $\times \cos \delta_f$ - (5-48) $\times \sin \delta_f$, it yields

$$T_\delta \cos \delta_f - \delta_T \sin \delta_f = F_{yf} + \frac{afmg}{a+b} \sin \delta_f \quad (5-50)$$

By substituting Eq. (5-6) into above equation, and applying small angle approximation ($\cos \delta_f \approx 1$ and $\sin \delta_f \approx \delta_f$), Eq. (5-50) can be yielded as

$$\delta_f = \frac{T_\delta + C_f \frac{v_y + a\gamma}{v_x}}{C_f + \delta_T + \frac{afmg}{a+b}} \quad (5-51)$$

Likewise, from (5-48) $\times \cos \delta_f$ + (5-49) $\times \sin \delta_f$, it yields

$$\delta_T \cos \delta_f + T_\delta \sin \delta_f = F_{xf} - \frac{afmg}{a+b} \cos \delta_f \quad (5-52)$$

After substitution of F_{xf} , we can obtain

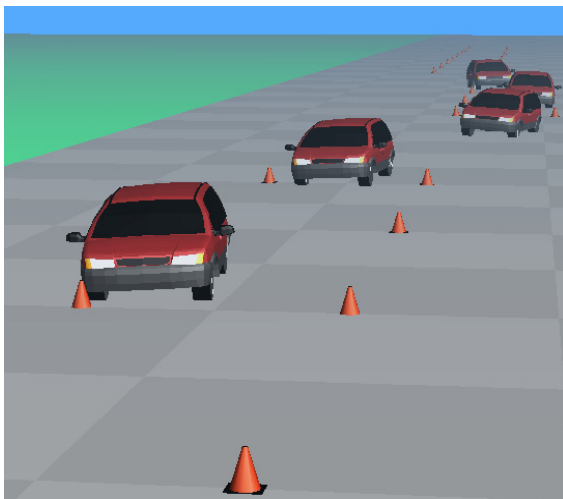
$$F_T = \delta_T + T_\delta \delta_f + f \frac{b}{a+b} (mg - k_L v_x^2) \quad (5-53)$$

Therefore, $u_c = [F_T \ \delta_f]^T$ can explicitly be calculated from using (5-51) and (5-53).

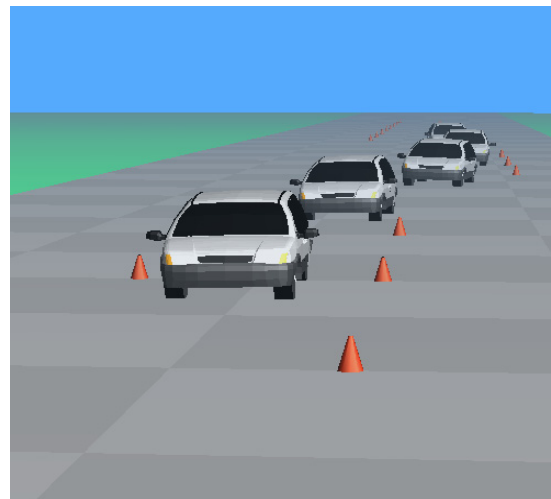
5.4. Numerical Simulations

In this section, simulation results of our proposed TS-fuzzy driving controller under a standard double-lane-change (DLC) maneuver are presented. The software used here is *CarSim*, a general software to simulate the dynamic behavior of a road vehicle and provide the interface programmed by Matlab/Simulink and animation [28]. The nominal values of vehicle parameters which are required in simulation are given as Table A.3 in Appendix A. Two remarkable examples are compared with our control algorithm to highlight the feature of our approach.

Comparison 1: In Autopia program, fuzzy logic control is used to design the steering control and the speed control separately [10-12]. As shown in Fig. 5-4, the left vehicle is controlled by using Autopia approach, while the right vehicle is controlled by our controller. The control objective is to follow the desired lateral offset trajectory (to vehicle's CG, $d_s = 0$ m) of DLC and maintain a reference velocity of 90 km/h. Figures 5-5(a) and 5-5(b) depict the two vehicles' lateral offset and reference velocity response, respectively. The Autopia approach fails to track the desired lateral offset trajectory, and its velocity response varies more promptly than our proposed controller. It can be concluded that even though fuzzy control is applied in vehicle speed and steering controller, the coupling effect still can not be handled due to the separation design of vehicle longitudinal and lateral control.



Autopia approach



T-S fuzzy driving control

Fig. 5-4. Animation window of Comparison 1.

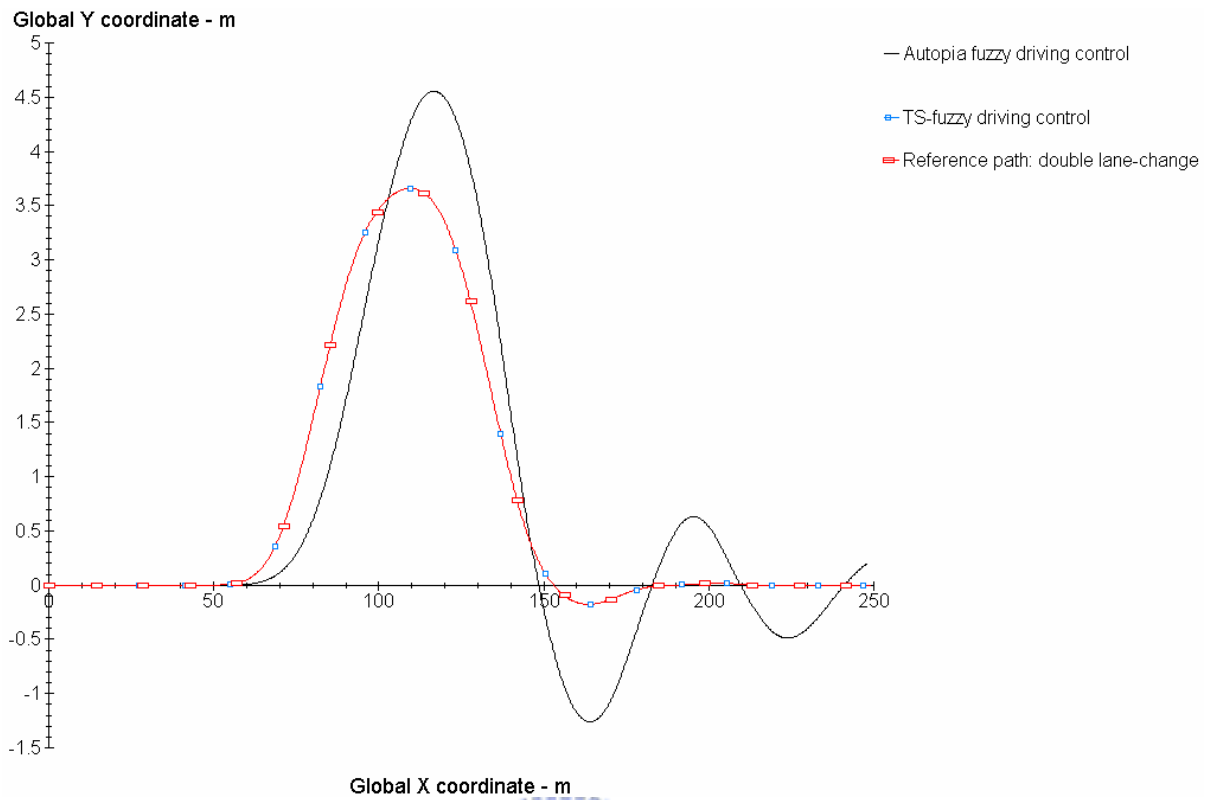


Fig. 5-5(a). Lateral offset comparison of the proposed controller against the Autopia approach.

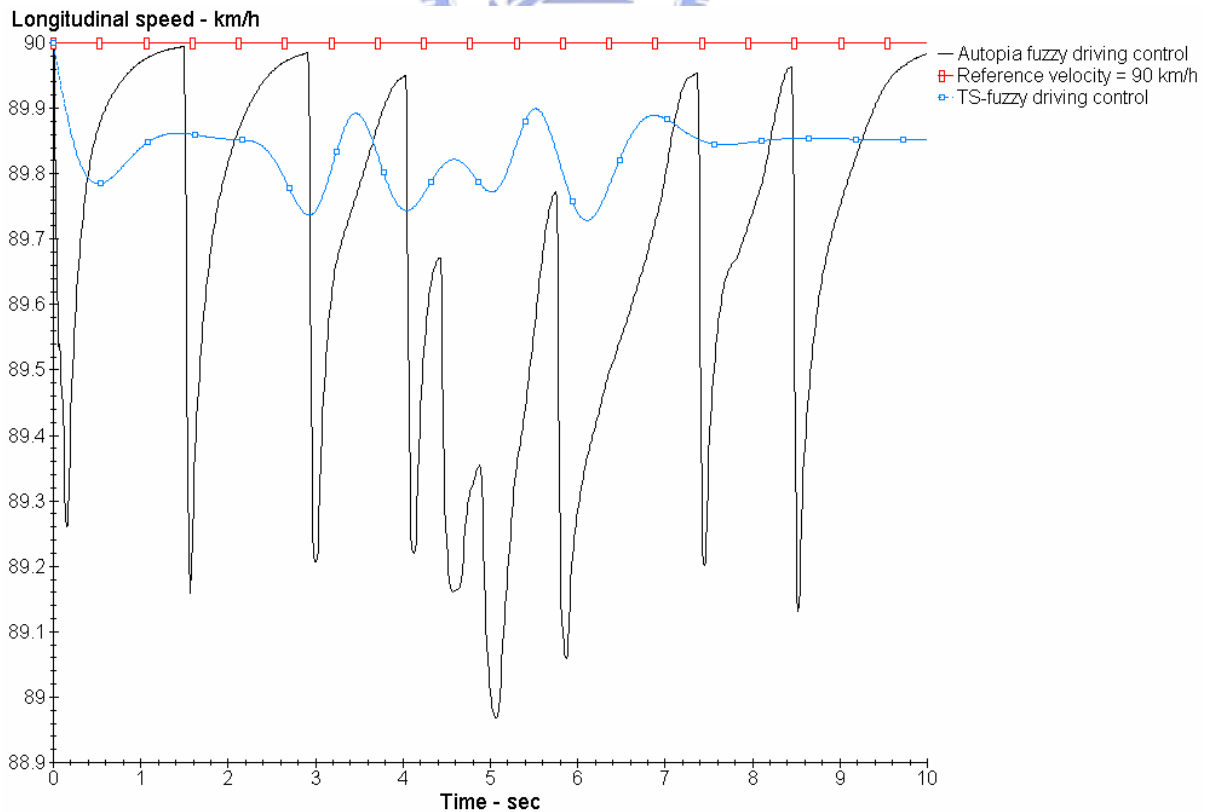
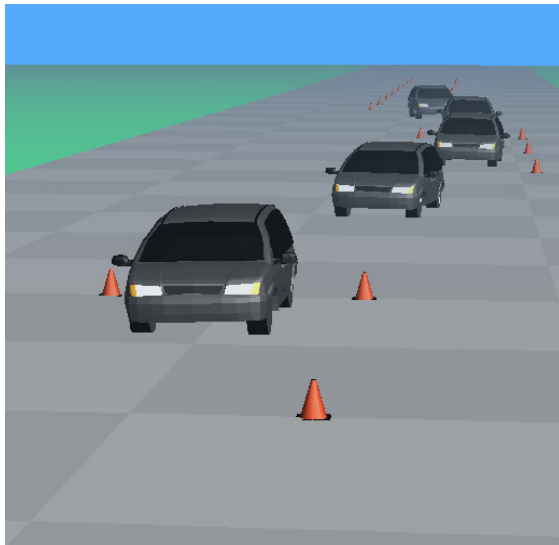
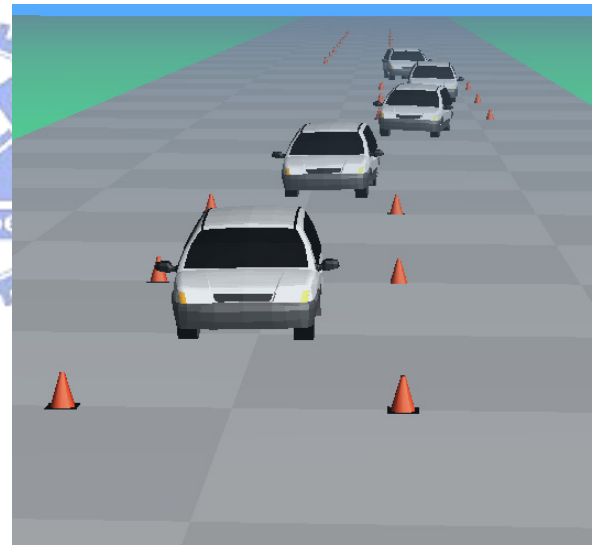


Fig. 5-5(b). Velocity comparison of the proposed controller against the Autopia approach.

Comparison 2: The next comparison is with the MacAdam preview model which is most widely referred human steering model [53], and verified experimentally to predict average human steering motion accurately. The speed control with MacAdam preview model is a PI controller designed by *CarSim*. The animation plot is shown in Fig. 5-6. The control objective is the same as a DLC maneuver. Here the sensor location for the lateral offset is at a fixed preview distance $d_s = 10$ m. This distance corresponds to the preview time 0.4 s while the vehicle velocity is 90 km/h (25 m/s). In Figs. 5-7(a) and 5-7(b), it can be seen that our controller is approximate to the MacAdam model with preview time 1 s in the DLC trajectory tracking performance. This preview time implies that the required previewed distance is 25 m which is difficult to be implemented by vision systems as mentioned previously. As shown in Fig. 5-7(b), the velocity tracking performance of the proposed T-S fuzzy driving system is better than the PI speed controller.



MacAdam model with the preview time = 1 s and PI speed controller.



T-S fuzzy driving with the preview distance = 10 m

Fig. 5-6. Animation window of Comparison 2.

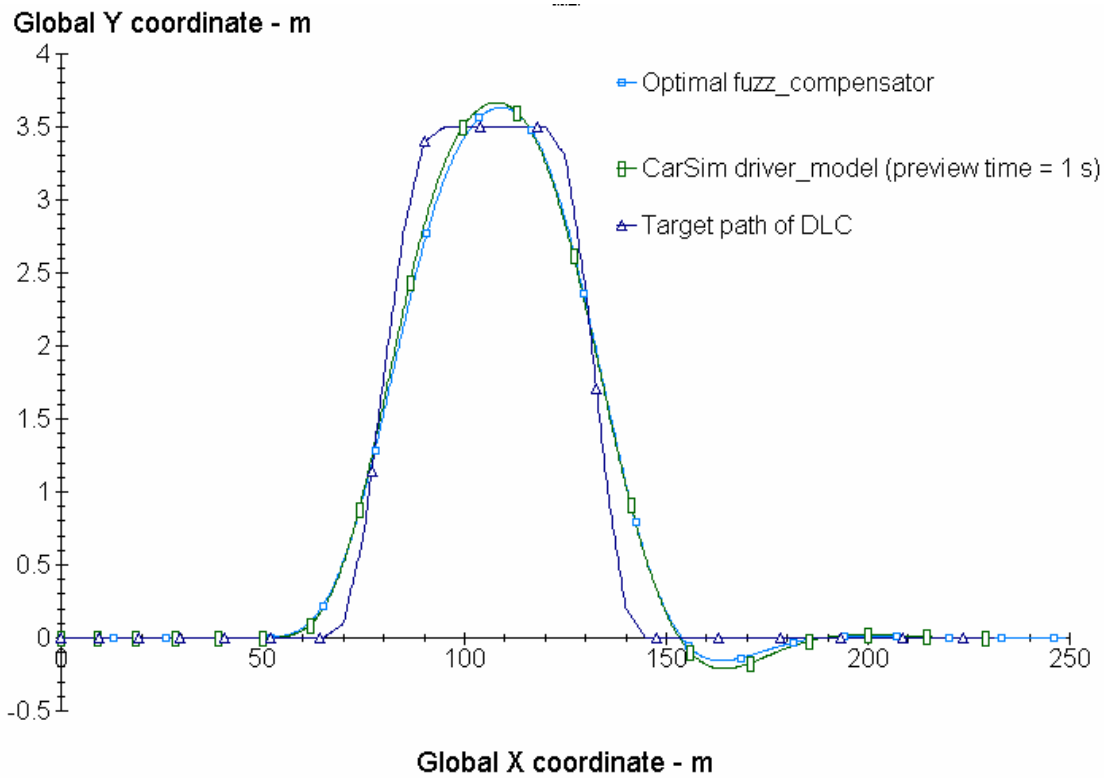


Fig. 5-7(a). Trajectory comparison of the proposed controller against the MacAdam model with preview time 1 s.

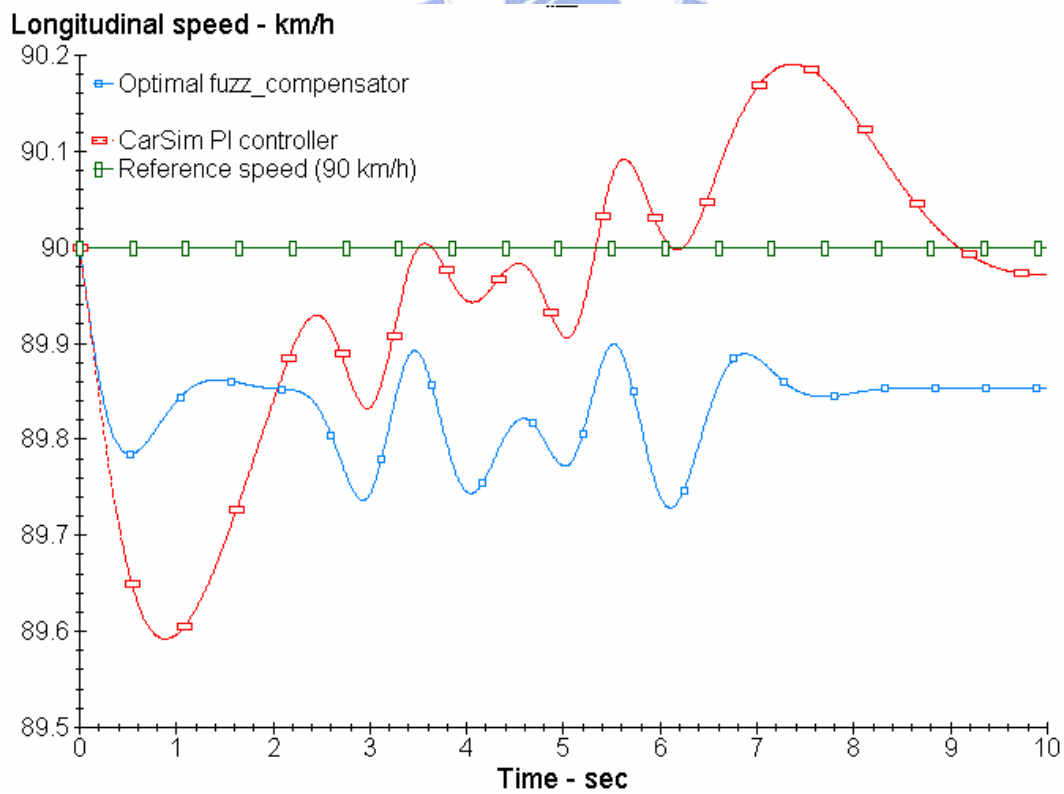
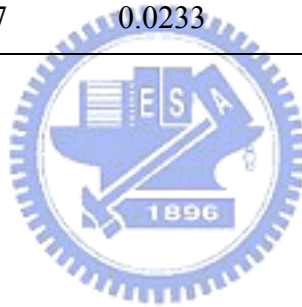


Fig. 5-7(b). Velocity comparison of the proposed controller against the PI speed controller.

Table 5-1 summarizes the DLC performance for the proposed TS-fuzzy automated driving controller with preview distances [0, 5, 10] m. The maximum and average errors of distance between C.G. of the vehicle from the road centerline are denoted as $|e_{y_max}|$ and $|e_{y_ave}|$, respectively. The maximum and average errors of velocity between the referenced and the measured vehicle velocity are denoted as $|e_{vx_max}|$ and $|e_{vx_ave}|$, respectively. The vehicle velocity is at 90 km/h. It can be seen that the longer preview distance improves the tracking accuracy of lateral offset trajectory but does nothing to velocity tracking performance. Consequently, the value 10 m for the preview distance is adequate to be implemented by the vision system.

TABLE 5-1. DLC performance with different preview distances.

d_s	$ e_{y_max} $ (m)	$ e_{y_ave} $ (m)	$ e_{vx_max} $ (m/s)	$ e_{vx_ave} $ (m/s)
0 m	0.2723	0.0652	0.0761	0.0466
5 m	0.1327	0.0328	0.0747	0.0462
10 m	0.0927	0.0233	0.0754	0.0467



Chapter 6

Experimental Results

6.1. Test-track Testing

The system implemented on Taiwan *i*TS-1 was firstly tested at the Automotive Research and Testing Center (**ARTC**) with respect to different weather and lighting conditions. The missions of automated lane-keeping with varying velocities on 2 testing-tracks are summarized in Table 6-1. Some events like rain which can not occur usually are denoted as N/A.

TABLE 6-1. Testing Conditions of Different Environmental Sets.

Weather \ Testing Track	Sunny	Cloudy	Night	Rainy
CDTT	0 ~ 145 km/h	0 ~ 145 km/h	0 ~ 90 km/h	N/A
NVHSTT	0 ~ 130 km/h	0 ~ 120 km/h	0 ~ 90 km/h	N/A

CDTT: Coast down test track.

NVHSTT: Noise vibration & harshness surface test track.

Lane-keeping mode was initially evaluated on the test track at **ARTC**, and the experiments of regulation were undertaken to examine the stability of the overall system at various speeds. Initially the system was tested without FGS compensation. In this case, the automated steering control oscillated when the velocity was increased to around 70 km/h. When the vehicle continued accelerating, the steering action was untamed, worsening the system. Figure 6-1(a) shows sampled experimental results under these testing conditions. In the case of FGS compensation, the vehicle could be automatically steered in the lane of CDTT while the velocity was increased to around 145 km/h, as shown in Fig. 6-1(b). The vehicle also steered well on the NVHSTT with a harsh and vibration surface at a velocity of around 130 km/h, as shown in Fig. 6-1(c). Besides irregular surface, a segment of the NVHSTT only has single-side lane-marking. The performance of lane-keeping was indicated by the lateral offset

at a look-ahead distance ($L_d = 15$ m) measured by the vision system. Thus, one can well imagine that the vehicle tracks the centerline of roads correctly in spite of varying vehicle velocities and vibration surface of the road. The control action of SW (in the right bottom plot) is small even the vehicle was accelerated up to a high velocity. This kind of action is conformed to a human-driver behavior.

Although not shown, the night test for the automated lane-keeping system also has been carried out with the maximum velocity 90 km/h, without any street lamps except the front vehicle lamp.

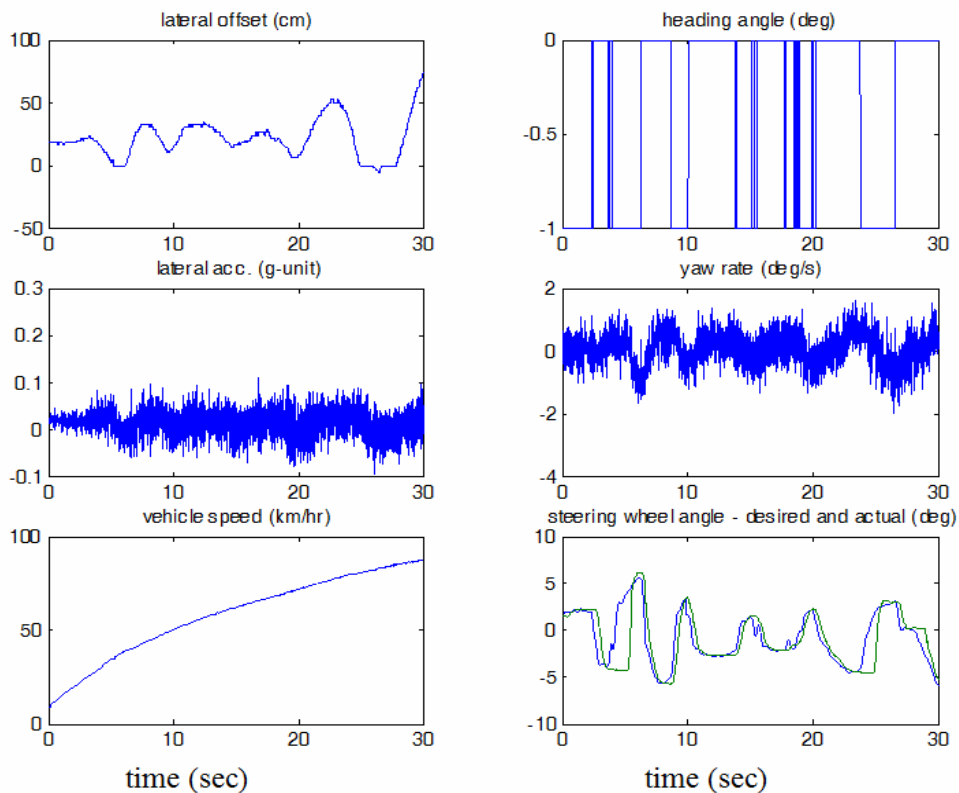


Fig. 6-1(a). The experimental results without FGS on the CDTT (straight lane with flat surface).

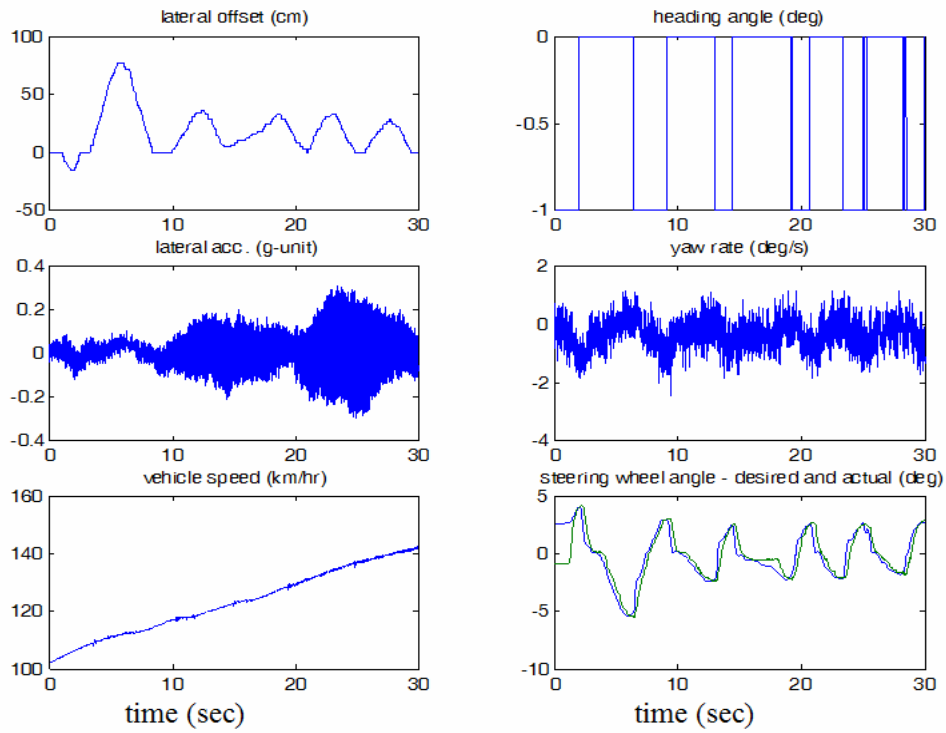


Fig. 6-1(b). The experimental results with FGS on the CDTT (straight lane with flat surface).

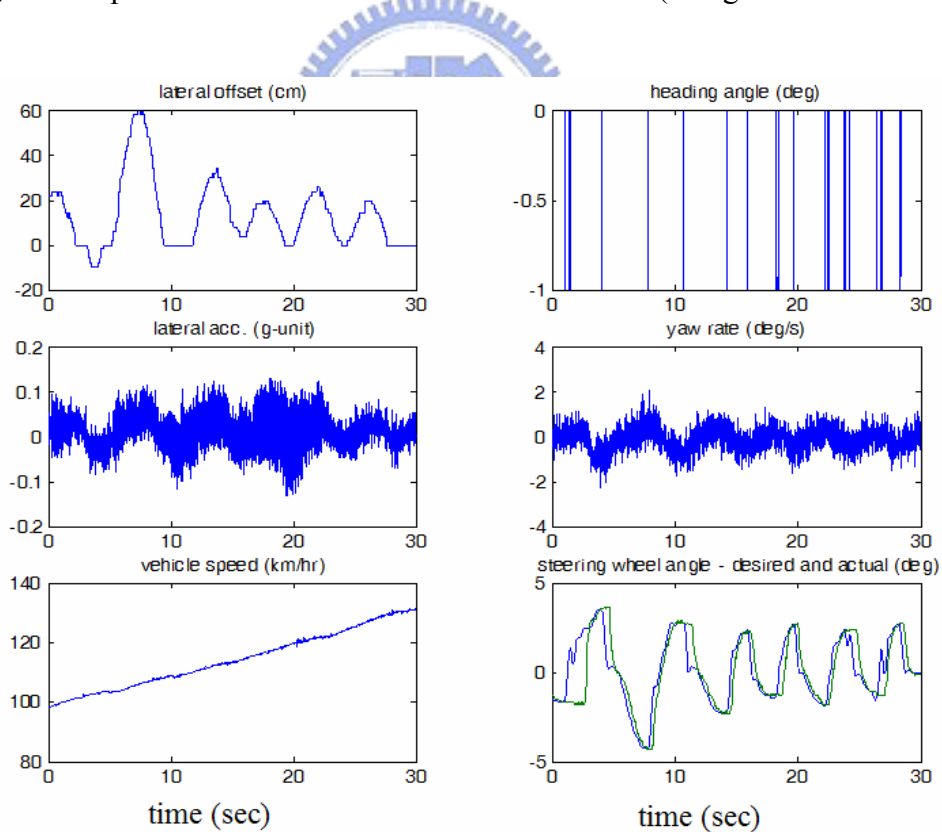


Fig. 6-1(c). The experimental results with FGS on the NVHSTT (straight lane with irregular surface including single-side lane marking segment).

6.2. Expressway/Highway Testing



Fig. 6-2. The snapshot of the experiment on expressway.

The experiments on freeway/highway have two stages. **In the prior stage**, only the throttle is ready to be used in the longitudinal system. The experiments are done at Expressway No. 68 (Chutung-Nanliao segment, Hsinchu, Taiwan) under real-traffic environment. Two vehicles were used to test the system, as shown in Fig. 6-2. The preceding-vehicle drives manually in simulating real traffic conditions (unpredicted cut-in/exist-out and speed-up/speed-down). The subject-vehicle (Taiwan *i*TS-1) is defaulted at hybrid LK and CC mode. Once a valid-target is detected, the switch to hybrid LK and ACC mode will be automatically done. The subject-vehicle adaptively adjusts its speed to maintain a safety-distance which is determined by the following-velocity. If forward traffic is clear or the subject-vehicle reaches its target speed, CC mode will be activated again.

The sample history of the vehicle following experiments without the employment of the adaptive detection area is depicted in Fig. 6-3. Here the headway time σ is set as 1 second, which is the minimum requirement of ISO 15622. Figure 6-3(d) shows the throttle input which is normalized from 0.13 (pedal fully released) to 0.82 (pedal fully pressed). Fig. 6-3(c) displays the desired velocity (dashed line) and current velocity (solid line) of the controlled vehicle. The desired headway distance (broken line) and the measured distance (solid line) from the range finder are shown in Fig. 6-3(b). The desired acceleration (with the bounded $a_{f \max}$ of 2 m/s^2) calculated from the supervisory control is depicted in Fig. 6-3(a).

As evident in Fig. 6-3(b), there are some apparent pulse signals (illustrated in the circled area) which exist at the signal of the inter-vehicle distance measured from the range finder. This is because at this instant, the preceding vehicle is undetected by the range finder due to the fact that the forward vehicle moving outside of detected area (target-missing). This

situation occurs when the two vehicles move on curves with an approximate radius of 400 m, and especially when the following vehicle is driven near the outside edge while the preceding vehicle is driven near the inside edge of the road. In Fig. 6-3(a), it can be seen that the calculated acceleration fluctuates dramatically. In this situation, the system switches to the higher velocity cruise control mode which causes the command of the throttle voltage to become erratic, as shown in Fig. 6-3(d). Consequently, for a vehicle velocity of 80-60-80 km/h, the initial detection angle of $\pm 2^\circ$ is deficient when compared to the required detection angle in the adaptive detection maneuver ($\pm 4.6^\circ$ – 5.9° , refer to Table 4-1 in Chapter 4). Although the human driver can apply the brake to avoid the sudden acceleration of the controlled vehicle, such an action may not be desired due to the simultaneous actuation of both the throttle and the brake.

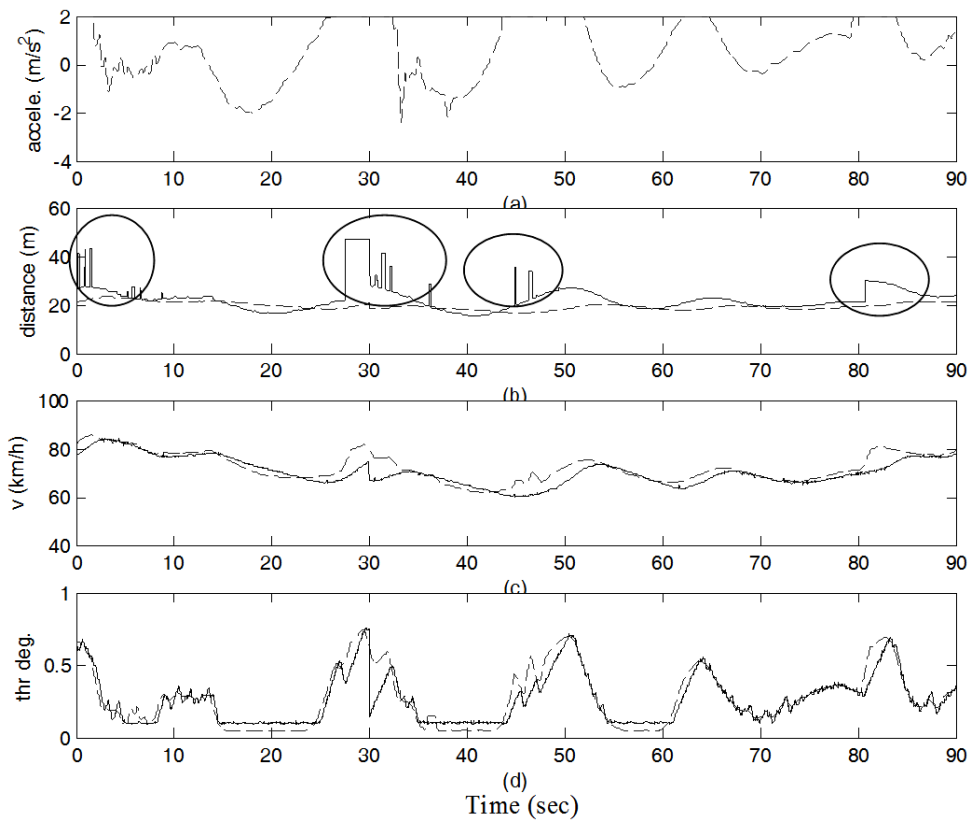


Fig. 6-3. The sampled history of vehicle following experiments without adaptive HDA maneuver (Dashed line: reference signal; solid line: real signal).

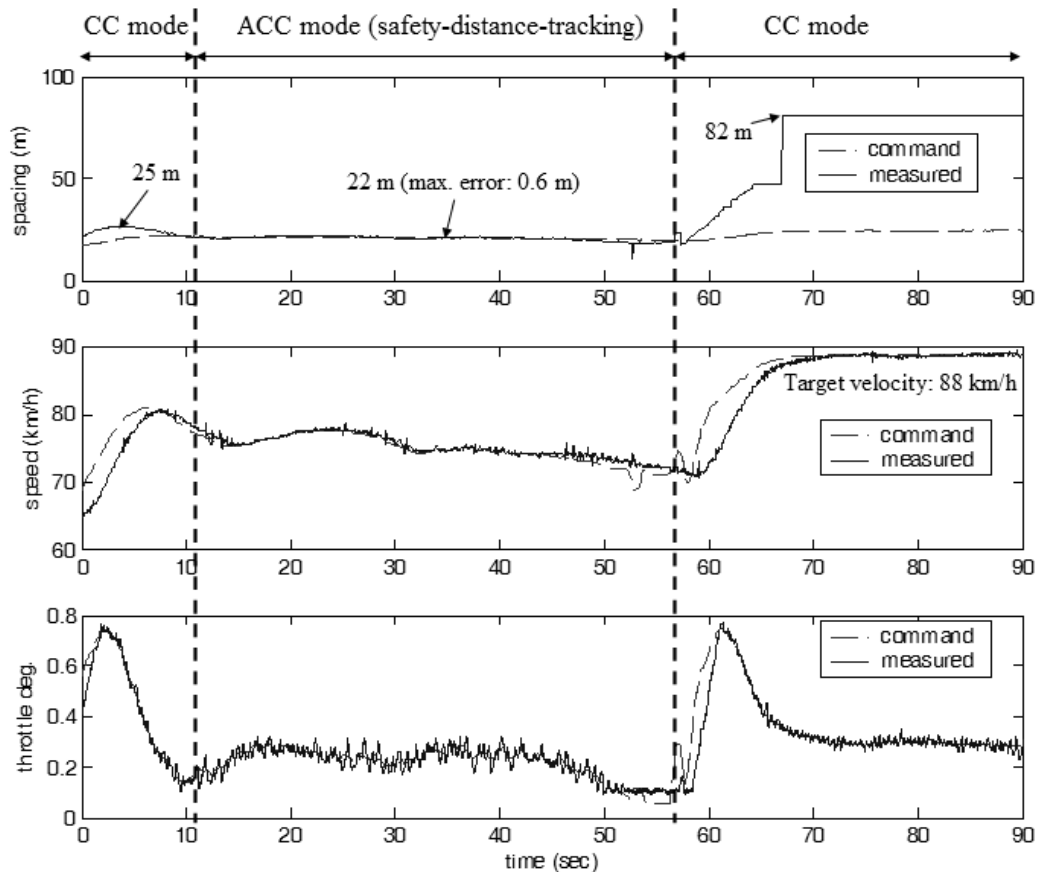


Fig. 6-4. The sampled history of experiments involving the transition between CC and ACC mode (Dashed line: reference signal; solid line: real signal).

Figure 6-4 depicts the sample history of experiments which involved the employment of the adaptive detection area. In contrast to Fig. 6-3(b), there was no pulse signal in Fig. 6-4(b). This indicates that no target-missing detection occurred while the vehicles moved over the same curves with a radius of approximately 400 m. Initially the controlled vehicle moved with a velocity of 65 km/h, and one vehicle ahead is detected at 25 m, but it is outside of the desired operation range (18 m for the headway time $\sigma = 1$ s). Once the controlled vehicle accelerates to nearly 80 km/h and the preceding vehicle is within the operation range of 22 m at time = 10 s as shown in Fig. 6-4(b), the system adjusts the throttle to execute the desired velocity command for the vehicle following control. During the steady-state vehicle following (from 10 s to 50 s), not only does the subject vehicle track the desired velocity successfully as shown in Fig. 6-4(c), it also maintains the desired headway distance (in Fig. 6-4(b)) with respect to the preceding vehicle. It should be noted that the vehicle velocity is not fixed but it varies within the range of [70, 80] km/h. The maximum error in the safety-distance tracking is

0.6 m. When the preceding vehicle changes to the neighboring lane at 60 s, the automation system identifies the condition as one in which there is no vehicle ahead. Thus, the following vehicle automatically switches to the velocity cruise mode and accelerates to the pre-selected velocity of 88 km/h. As illustrated in Fig. 6-4(c), after 60 s point the velocity of the controlled vehicle converges smoothly to the reference velocity profile.

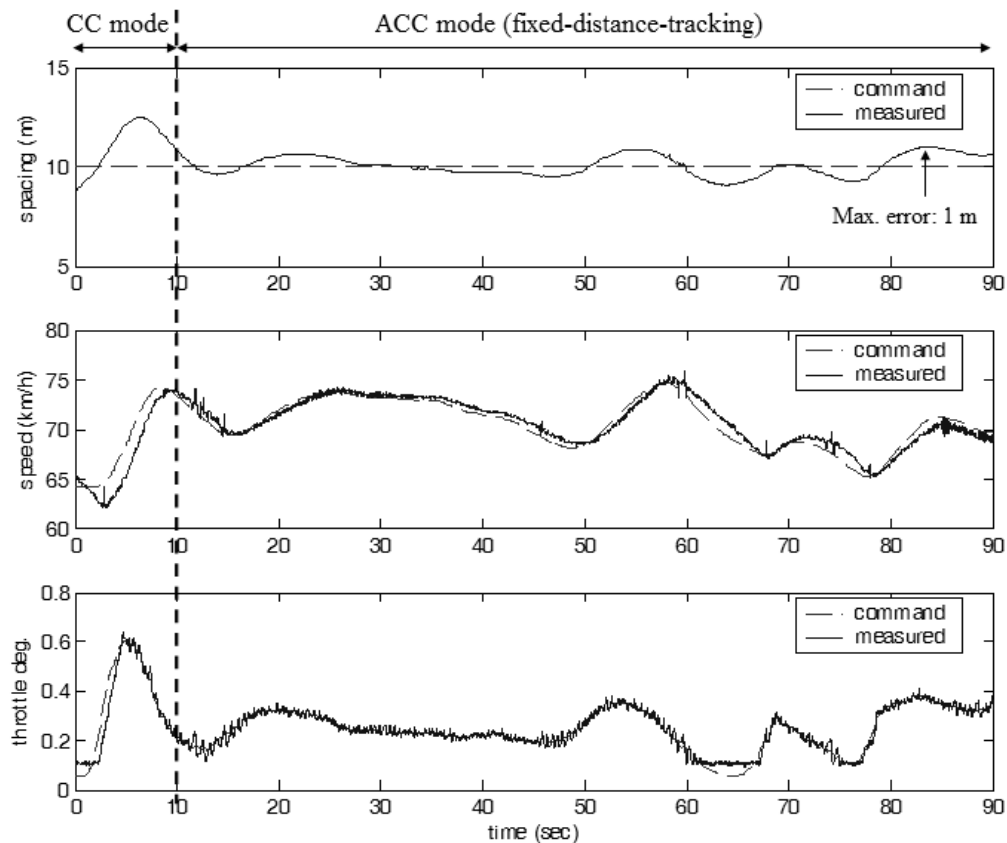


Fig. 6-5. Performance of ACC mode (fixed-distance-tracking) in a real traffic environment.

The experiment for two-car platoon-control scenario, namely fixed-distance-tracking of ACC mode, was demonstrated in the real traffic environment. The experimental results are shown in Figure 6-5. According to traffic condition (traffic-jam), a preceding-vehicle drives at varying velocity (around 70 km/h in the middle plot). The subject-vehicle (initial velocity at 62 km/h) accelerates to about 74 km/h automatically, and then decelerates to 70 km/h for maintaining a fixed headway-distance 10 m (at 12 s in the top plot). In real situation, it is arduous for a human driver in the preceding vehicle to manually drive at a fixed velocity. Therefore, the subject-vehicle will adjust its throttle degree (in the bottom plot) slightly to maintain a fixed inter-vehicle distance 10 m. A good tracking is shown in spacing (in the top

plot of Fig. 6-5). Without braking assistance, the maximum intra-spacing deviation is 1 m only.

In the second stage, the brake actuation is added to assist the system in the vehicle longitudinal motion control. As a result, the subject-vehicle can manage throttle and brake to keep the reference distance or velocity against irregular road conditions such as non-flat, up-gradient, downhill level, and slippery or rough surface. Firstly, we demonstrate the reference velocity tracking, namely CC mode, at velocities from 20 to 90 km/h. The experimental results of CC mode are quantified at different speeds in Table 6-2 which shows the performance of the regulation control. e_v represents the error between the real speed and the desired speed, $|e_v|_{avg}$ is the absolute value of the mean error, and $|e_v|_{max}$ is the absolute value of the mean error.

TABLE 6-2. Performance of CC mode at different velocities.

Speed	$ e_v _{avg}$ (km/h)	$ e_v _{avg}$ (%)	$ e_v _{max}$ (km/h)	$ e_v _{max}$ (%)
20 km/h	0.2037	1.02	0.6018	3.01
30 km/h	0.3313	1.11	0.6717	2.24
40 km/h	0.1503	0.38	0.6174	1.54
50 km/h	0.1086	0.22	0.3991	0.8
60 km/h	0.1450	0.24	0.4532	0.76
70 km/h	0.1913	0.27	0.6936	0.99
80 km/h	0.1815	0.23	0.5571	0.70
90 km/h	0.1751	0.19	0.6167	0.69

The operation from ACC mode to CC mode is the same to the prior stage due to only throttle actuation is required. Therefore, we demonstrate the scenario that the subject-vehicle operates from CC mode to ACC mode. Experimental results of CC to ACC mode are shown in Fig. 6-6. Initially the subject-vehicle speed is at 90 km/h for CC mode. In the same way, the headway time is chosen as 1 s. The headway distance is the solid signal which represents the relative distance between two vehicles, and the safe distance is shown by the dash-dot signal in the top figure. A preceding-vehicle appears in the front of the subject-vehicle at 14 s. Since the headway distance suddenly drops, the system activates the brake control such that the headway distance can converge to the safe distance. At 18 s and 32 s, the

preceding-vehicle goes with higher speed so that the headway distance grows than the safe distance. In these two periods, the subject-vehicle intends to change to CC mode. However, at 27 s and 53 s, the relative distances become shorter than the safe distance. Thus the subject-vehicle decreases its velocity to keep the safe distance again. It can be seen that no matter the preceding vehicle's speed changes severely and frequently, the system can automate the throttle and brake pedal to drive the subject-vehicle to maintain the safe distance and the desired speed.

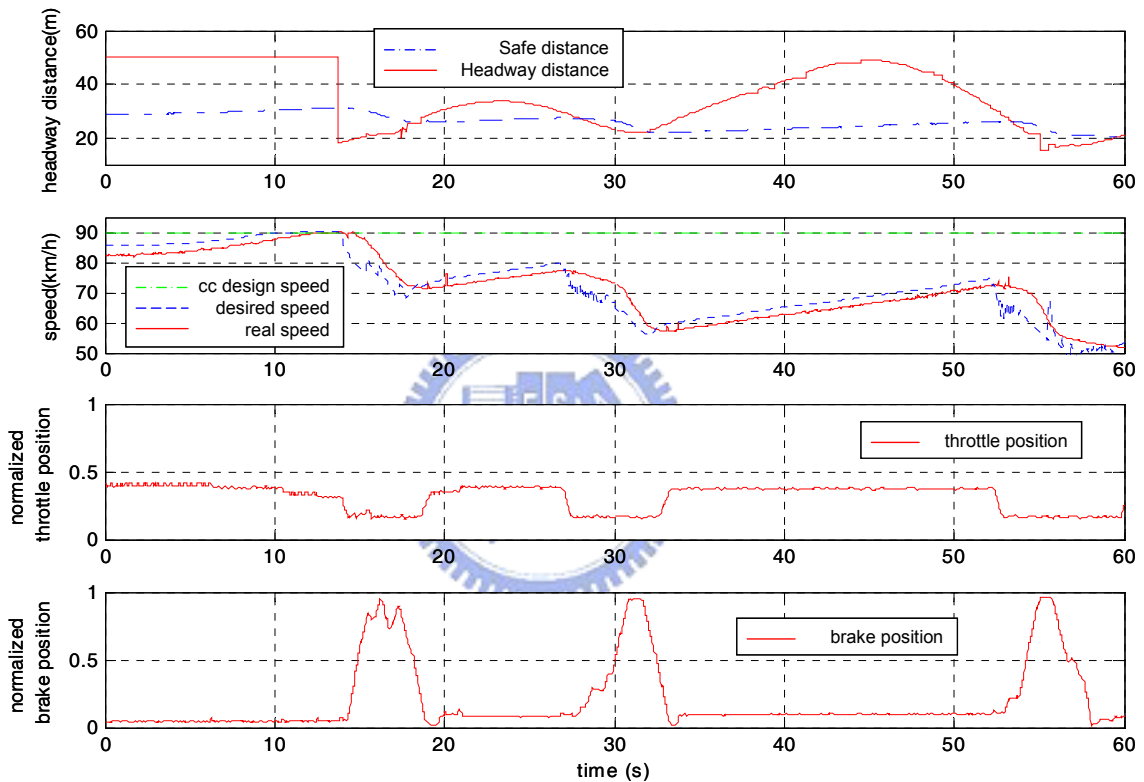


Fig. 6-6. Experimental results of CC mode switching to ACC mode.

The time response of the process in ACC mode is shown in Fig. 6-7. The headway time is set as 1 s again. In the period of [0, 8] s, the system actuates the brake pedal such that the subject-vehicle decelerate its velocity to maintain the safe distance with respect to the preceding-vehicle. After 8 s, the preceding-vehicle runs at varying speeds within [60, 80] km/h and the subject-vehicle keeps well the safe distance. It can be seen that actuating on the throttle during [10, 60] s, if necessary, is enough to assure fine tuning of the headway distance fitting the safe distance. After 60 s, the deceleration from 80 to 60 km/h requires applying brake control. This is similar to human driving condition: the driver applies the brake at the

end of the maneuver only, when it is strictly necessary. Otherwise, the driver just releases the throttle pedal since the vehicle can be decelerated by means of engine brake and tire-road resistance.

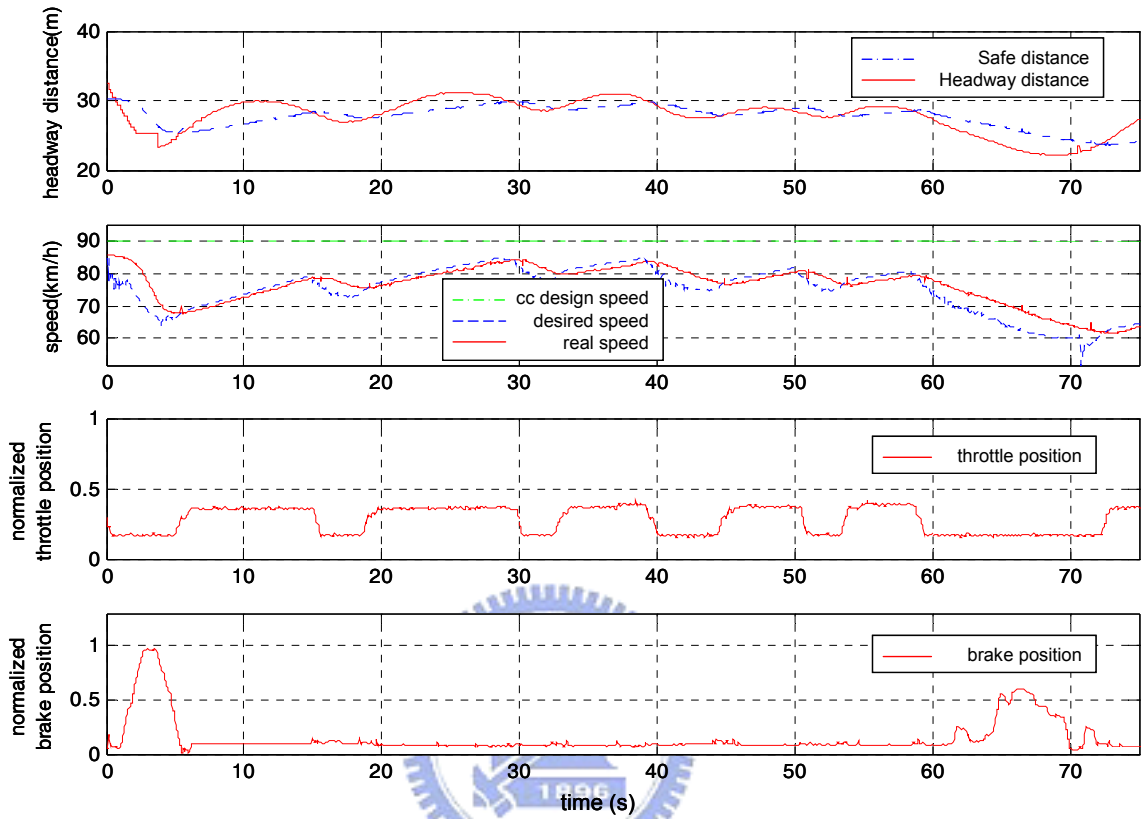


Fig. 6-7. ACC mode operation with throttle and brake actuation.

The performance for the LK mode in real traffic environments is shown in Fig. 6-8, where the subject-vehicle's velocity is determined by CC or ACC mode. We find that more lateral offset (in the right-top graph) exists in the real traffic environments since road-curvature is an unknown external input. But, the measured lateral offset at a look-ahead distance is still within 0.8 m. Besides, the error between the measured and the command SW signals (in the bottom plot) is small enough to keep the subject-vehicle driving along the centerline. Moreover, low lateral acceleration (within $\pm 0.2g$ in the middle plot) indicates driving comfort is ensured.

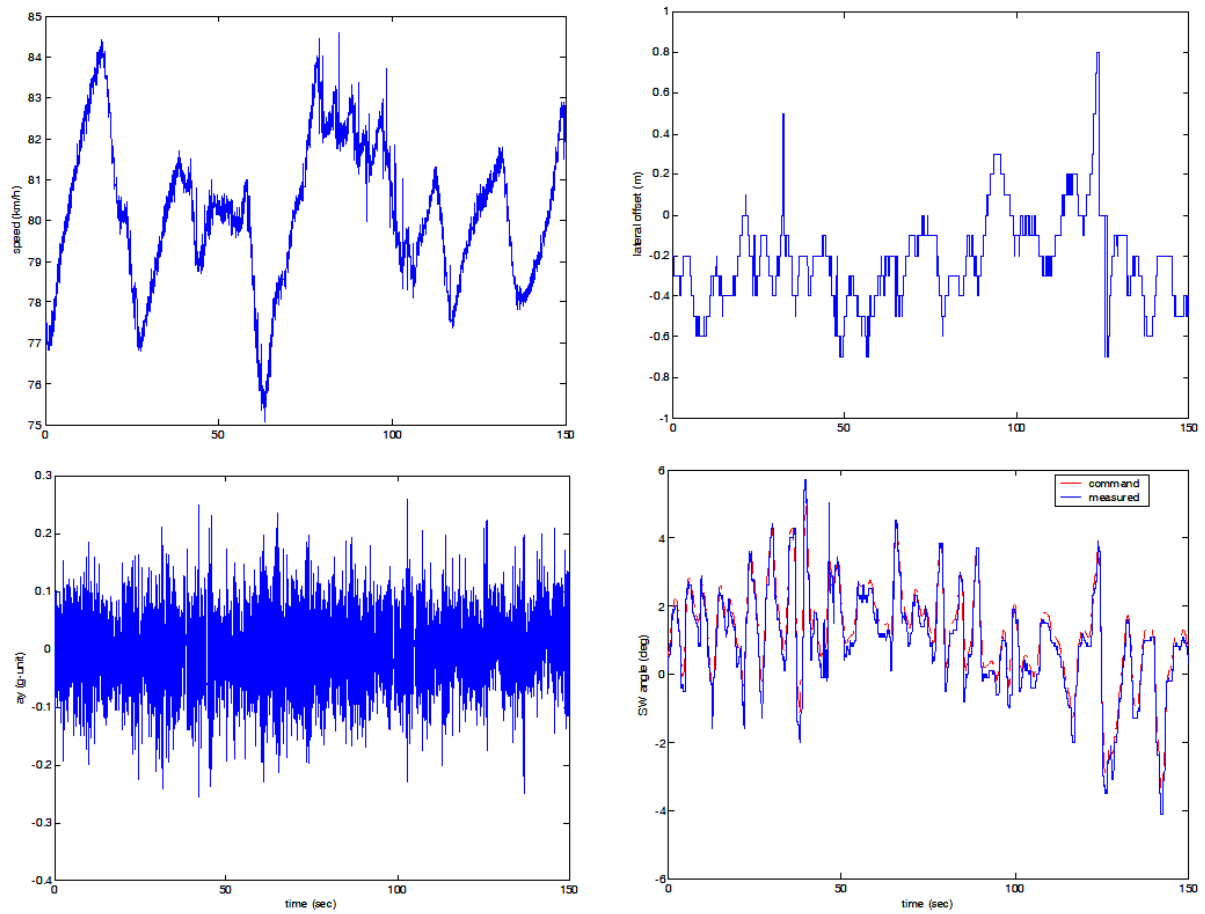


Fig. 6-8. Performance of LK mode operation under real-traffic environment in Highway No. 3.

The persuasive performance for the LK mode in real traffic environments is shown in Fig. 6-9. The subject-vehicle is moving at velocity 70 km/h across crucial curve, where the permissible highest velocity is 50-60 km/h. The curvature data is obtained from the vision system, and the maximum value is about 0.003 (≈ 300 m radius). As can be seen, the curve is with continuous changing and the maximum curvature approaches $1/200 \text{ m}^{-1}$. We find that

more lateral offset (in the top plot) exists in this situation. It can be concluded that the proposed FGS in the lateral control system reveals well capability of the curvature changing. The steering control from the DSP board is almost equal to that of dSPACE MABX, and the SW motor follows the controlling command well to keep the subject-vehicle driving along the centerline of road. Moreover, low lateral acceleration (within $\pm 0.2g$ in the middle plot) indicates that driving comfort is ensured.

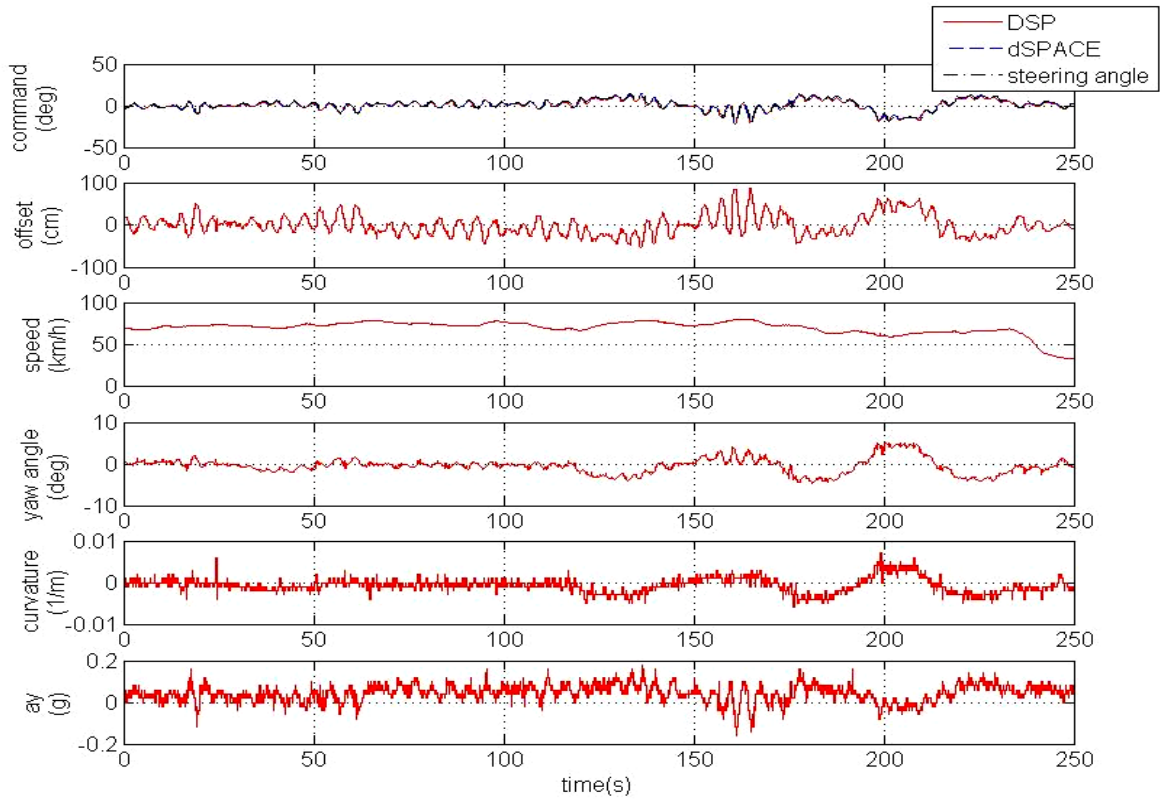


Fig. 6-9. LK mode operation under crucial curves in Expressway No. 68.

Figure 6-10 shows the frame grabbed from the vision system in the operation of LC mode. The lane-marking data will be lost due to the fact that the vision system cannot catch lane-marking in the lane-to-lane transition, as shown in the circled two plots of Fig. 6-10. When the vehicle moved to an adjacent lane, the vision system re-caught the lane-marking and thus the system returned to LK mode. The example lane-change control at speed around 56 km/h is shown in Fig. 6-11. The LC mode started at 12 s, and the SW was then controlled by the lane-change controller instead of the lane-keeping controller. During the period of lane-change (from 12 s to 18 s), initially the lateral offset will increase since the vehicle steered to the boundary of road. While the vision system cannot catch the lane-marking, the lateral offset data hold a maximum value of 200 cm (between 14 s and 16 s). After the lane-change command was completed at 18 s, the SW returned to the lane-keeping controller and the subject-vehicle kept the centerline of road. Here the command signal from dSPACE MABX is in LK mode and it provides the comparison with the controlling of LC mode. Figure 6-11 depicts the turn-left LC mode. The turn-right LC mode is shown in Fig. 6-12, and the velocity of subject-vehicle approximates 70 km/h. The overall lane-change maneuver is complete within 5~6 s which is according to our lane-change controller as designed in Chapter 3.

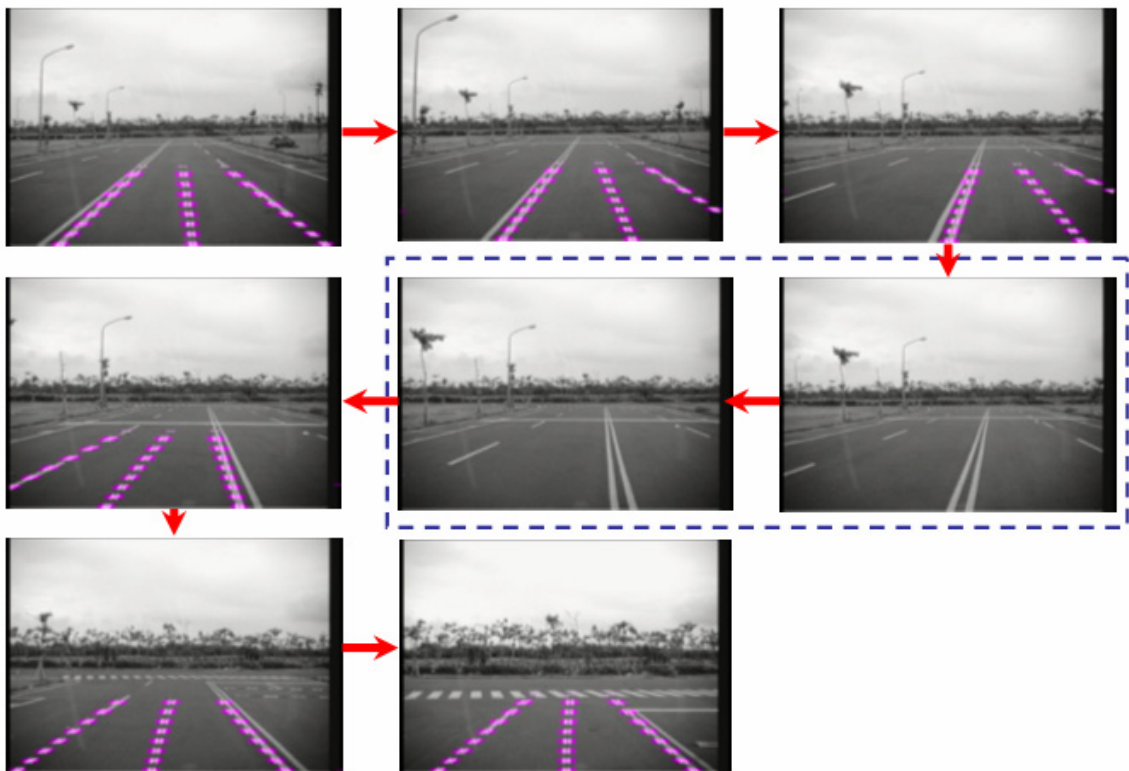


Fig. 6-10. Lane-marking detection in the lane-change scenario from the display of vision system.

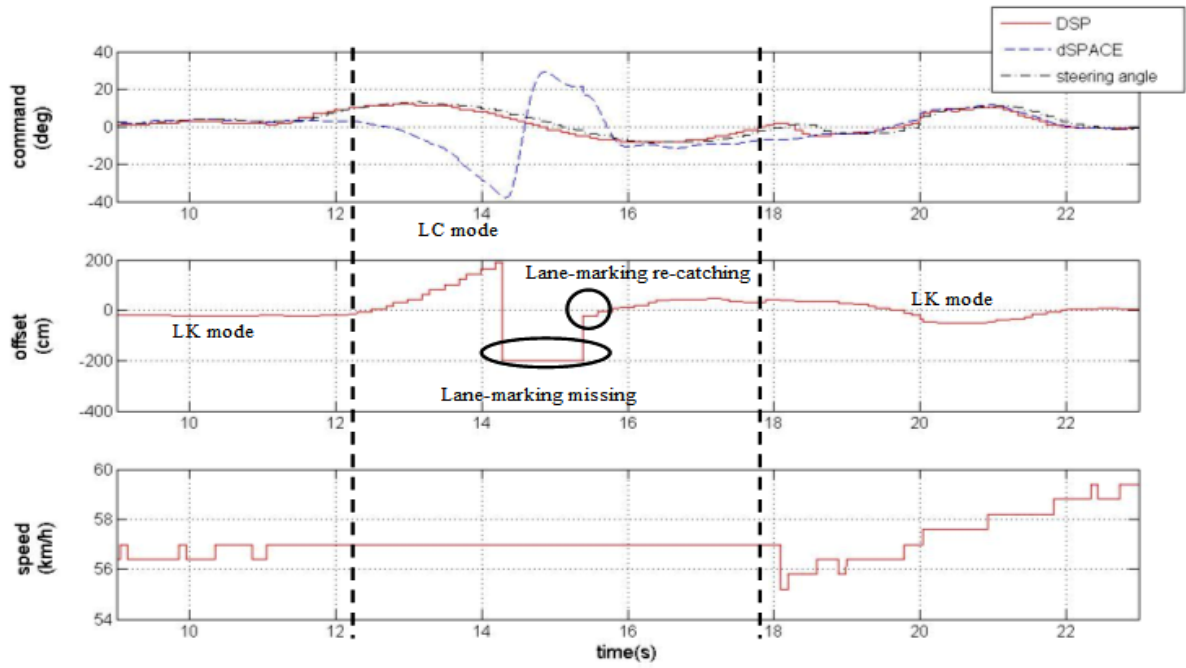


Fig. 6-11. The transition between LK mode and turn-left LC mode.

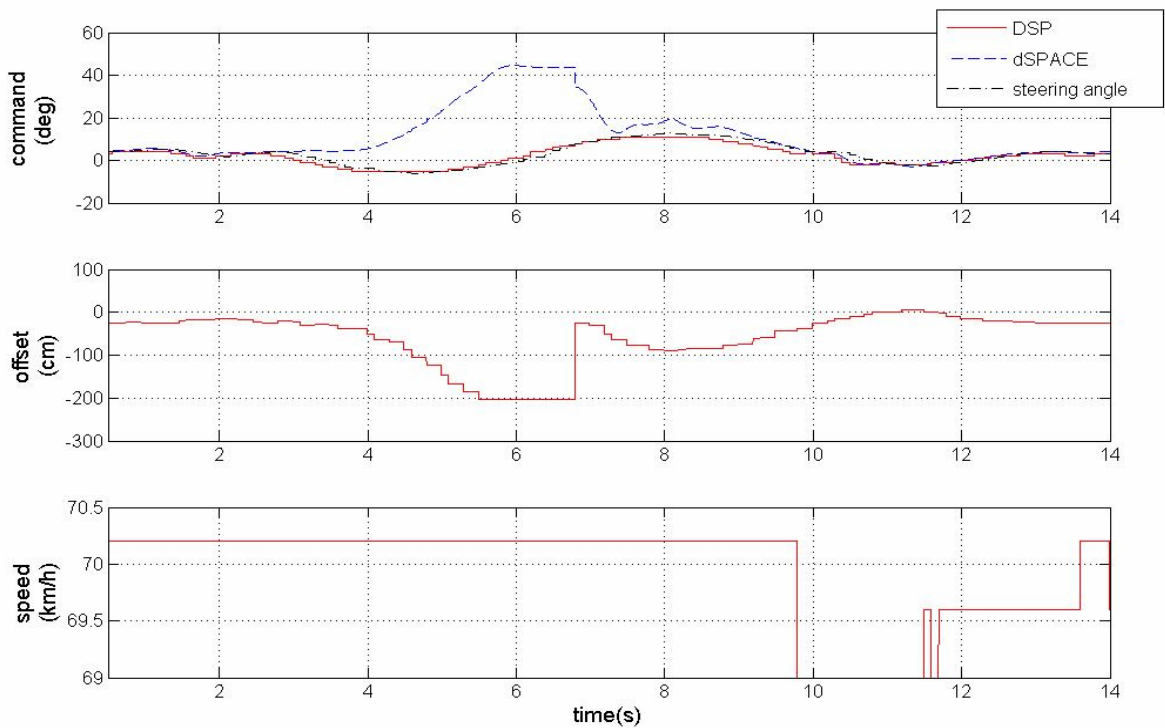


Fig. 6-12. Turn-right LC mode operation with the velocity 70 km/h.

To improve the free lane-change's feasibility, early-switch allows the lane-keeping control to intervene before LC mode completes. As shown in Figs. 6-13, once the vision system re-catches the neighboring lane-markings, the lane-keeping controller takes over the steering control to steer the subject-vehicle to the centerline of road. The intervention of LK mode is

illustrated in the red circle area, and it can be seen that the period of open-loop lane-change is shortened (about trisection) such that the disturbances from road surface and level can be reduced. In addition, the lateral acceleration during the lane-change is within the 0.2 g even the early-switch is applied. The required passenger comfort can be achieved through LK mode to LC mode, and back to LK mode.

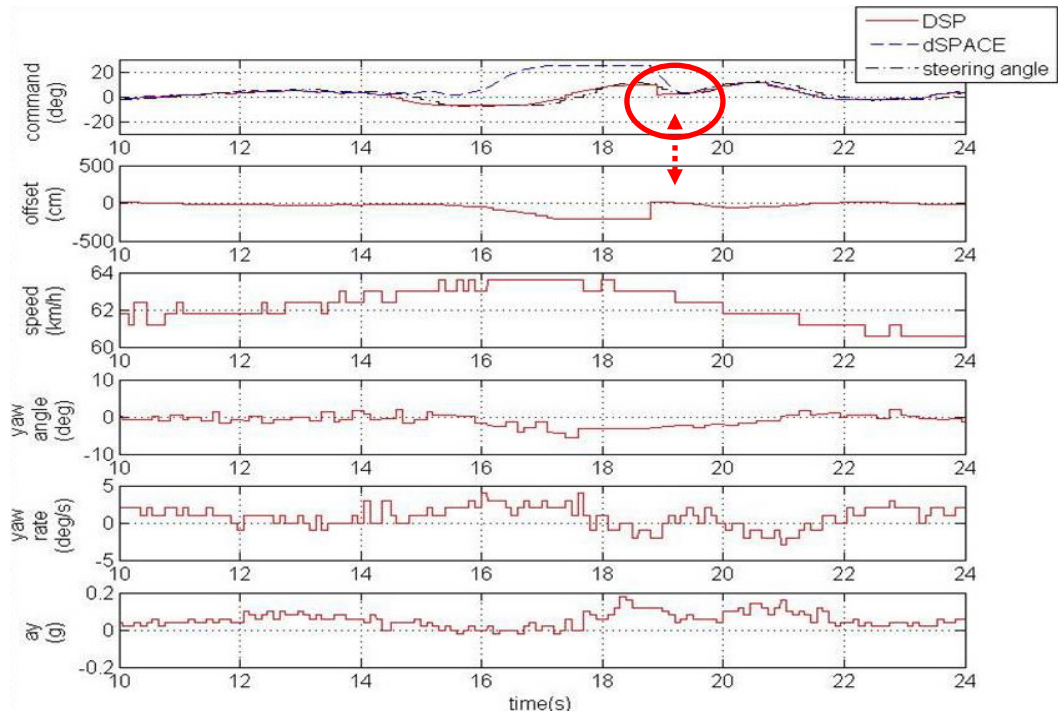


Fig. 6-13(a). Turn-right LC mode at 62 km/h with early-switch maneuver.

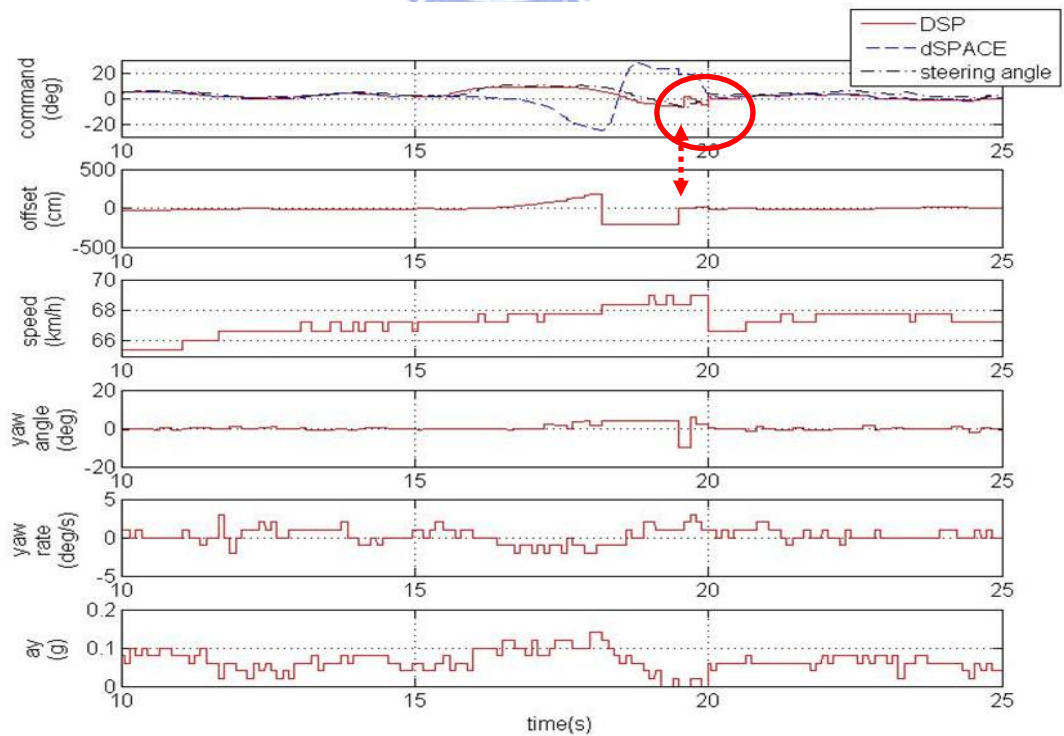


Fig. 6-13(b). Turn-left LC mode at 67 km/h with early-switch maneuver.

6.3. Urban-road Testing

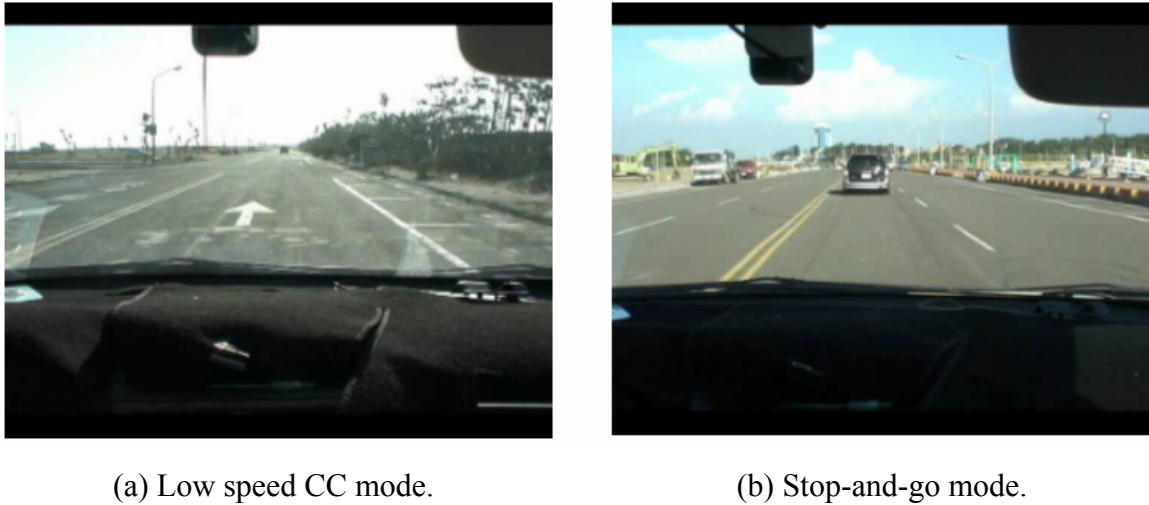


Fig. 6-14. The in-vehicle view for stop-and-go maneuver in the Nanliao Harbor Park.

In Fig. 6-14, the in-vehicle view represents typical traffic conditions at low speed in urban-road environment. Figure 6-14(a) represents that no preceding-vehicle in the front of the subject-vehicle and the system activates CC mode initially. The subject-vehicle will keep the reference velocity which can be chosen by the driver or the maximum velocity of urban-road. If a preceding-vehicle with lower speed appears in the same lane and finally stops ahead, the subject-vehicle reduces its speed to approach the preceding-vehicle gradually until it comes to a halt at a safe distance behind the preceding one. When the preceding-vehicle restarts moving, the subject-vehicle also moves and keeps a safe headway distance at any speed. Figure 6-14(b) represents the typical traffic jam scenario in which the vehicle continuously stopping and starting. The system adapts the subject-vehicle's speed to follow the preceding vehicle which is driven manually, stopping when necessary and keeping a safe distance even when circulating at low speeds.

As shown in Fig. 6-15, the initial condition of this scenario is that both the preceding- and subject-vehicles are stationary in the same lane with over 50 m apart and facing in the same direction. Here the maximum speed of CC mode is set as 30 km/h, 2 s for the headway time, and 4 m for the minimum stopping distance which is the typical length of a vehicle. The subject-vehicle starts driving along its lane at 5 s, with initial CC mode. As the subject-vehicle approaches to a stopping preceding-vehicle, the headway distance decreases, and the system switches to the stop-and-go mode, adjusting the speed to keep a safe distance. As the headway distance decreases, the throttle degree is also gradually released. Around 28 s,

the headway distance begins to be smaller than the safe distance, and thus the desired speed is less than the vehicle speed. At this point, the system applies the brake to slow down the vehicle, and the vehicle continues reducing speed until its headway distance reaches the minimum stopping distance. The second graph shows that the subject-vehicle stops at 4 m behind the preceding-vehicle from 32 s to 38 s. The preceding-vehicle then starts moving, followed by the subject-vehicle. This throttle/brake control behavior is very similar to human driving: The driver accelerates until a front car appears in the driving lane, then releases the degree on the throttle to slightly reduce speed and, if this reduction is not enough, applies the brake until the car stops without collision to the front car. This experiment reproduces the case of typical stop-and-go situation: the preceding vehicle is stationary and the following vehicle approaches the preceding one at high speed; this situation is very common at the tail end of a traffic jam and causes a lot of rear-end crashes.

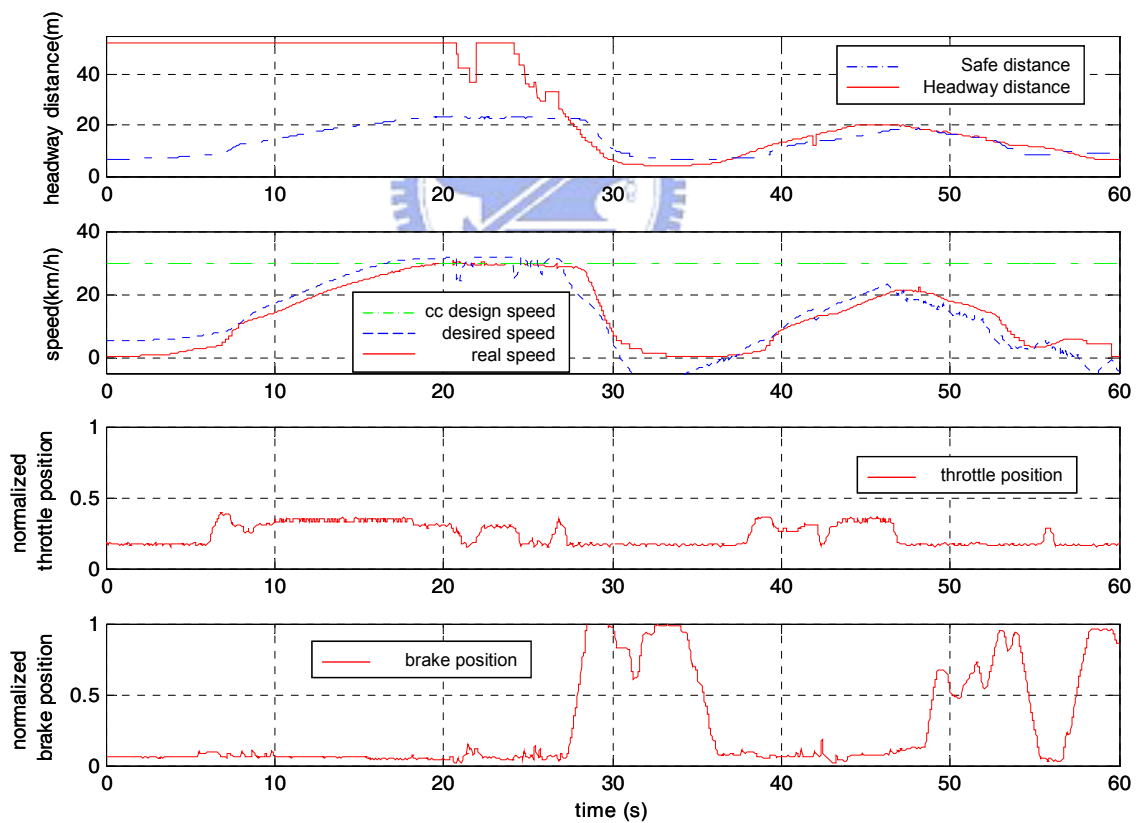


Fig. 6-15. Low speed CC mode switches to stop-and-go mode.

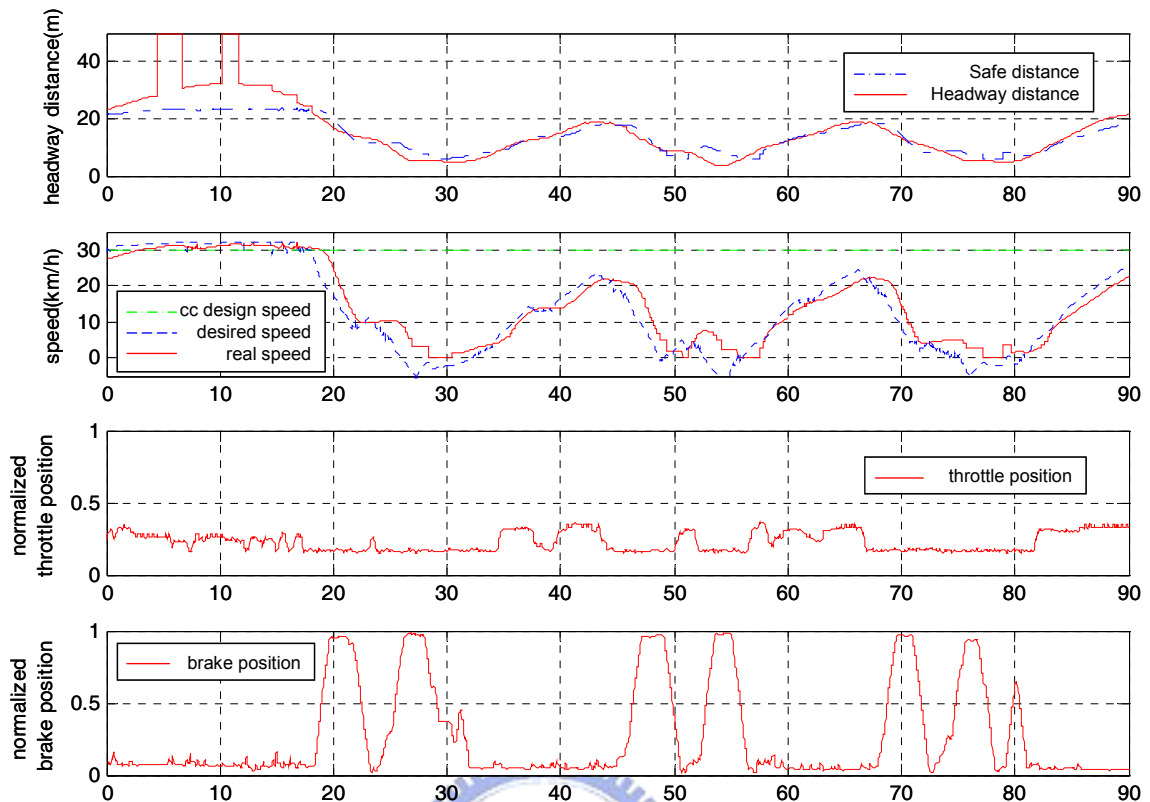


Fig. 6-16. Stop-and-go mode of the supreme 30 km/h.

This scenario is the realization of a stop-and-go automatic car-following. Figure 6-16 indicates the reaction of the controlled vehicle when the preceding one carries out successive stopping and restarting. The controlled vehicle tracks the preceding one very accurately and respects the headway targets, 2 s for headway time, and 4 m for minimum headway distance by using both pedals when necessary. As shown in the top figure, the controlled vehicle stops at 4 m behind the preceding vehicle at 27 s, 54 s and 75 s. While the preceding vehicle restarts, the controlled vehicle always tracks the safe distance to move. This experiment reflects the situation that the controlled vehicle tracks preceding one which stops and starts alternatively, as in a traffic jam. As speeds and distances are low, the rear-end crash risk decreases, but these situations are boring and tedious for human drivers and accidents are very common. The automation of these maneuvers is consequently one objective of the intelligent transportation systems.

In the Nanliao Harbor Park, the map information is initially obtained. Thus lane-change control based on the vision system and RTK-DGPS can be compared. In the following results, the term GPS offset (in cm unit) refers to the lateral offset which is recorded by RTK-DGPS

for the free lane-change maneuver. As shown in Fig. 6-17, the system can achieve the request of 3 meter offset for free lane-change maneuver. Though the vision-based lane-change is in the form of open-loop control, the performance is comparable to the GPS-guided lane-change which is shown in Fig. 6-18. Consequently, LC mode can be operated either using the vision system or GPS-guided map regarding to the driving circumstance.

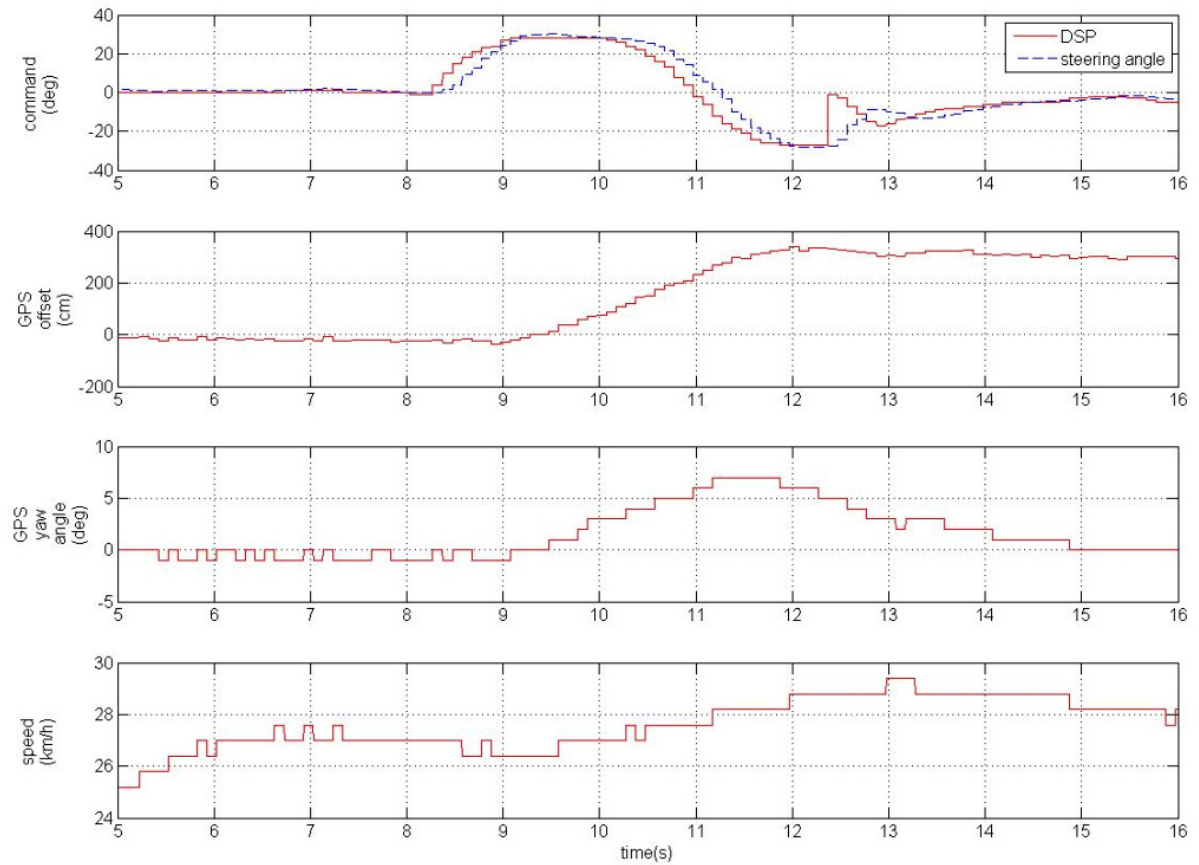


Fig. 6-17. Experimental results of the vision-based lane-change maneuver.

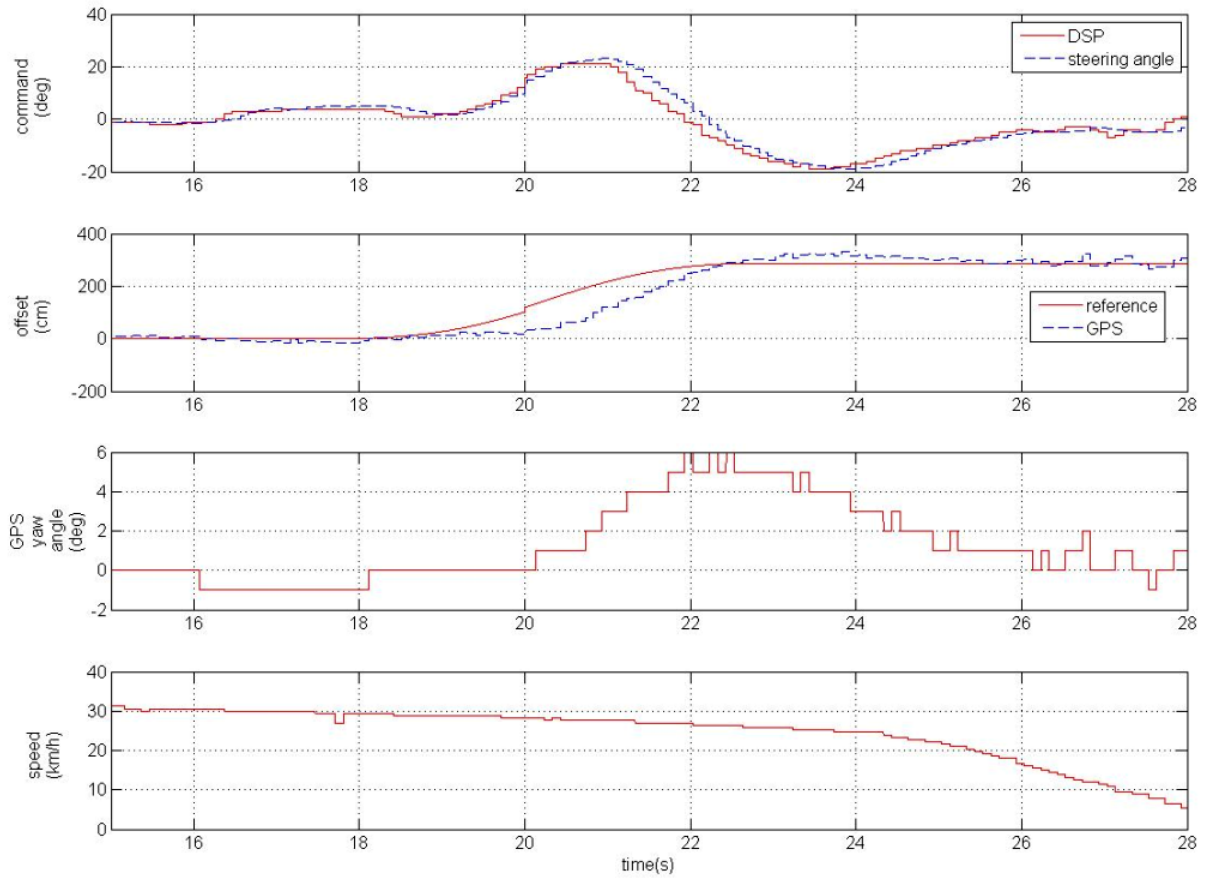
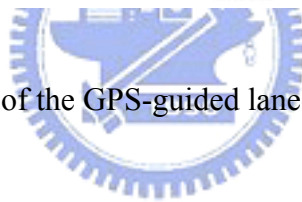


Fig. 6-18. Experimental results of the GPS-guided lane-change maneuver.



Chapter 7

Conclusions and Future Works

An automated driving control system with multi-mode operation is proposed. The system is constructed in a hierarchical autonomy structure to achieve integrated longitudinal and lateral motion control. Upper-level control determines the driving mode: the reference velocity is calculated by an adapted SMC technique with simplicity and robustness properties; the reference trajectory is generated by the ride comfort constraint. Vehicle-body control is designed on the basis of the fuzzy control technique for managing the vehicle's throttle-, brake- and SW-motor in such way to mimic a human driver. By means of the MABX or DSP board, and self-installed sensors and actuators, this system is implemented on an experimental vehicle, Taiwan *i*TS-1. The experimental results in real-traffic environments show that Taiwan *i*TS-1 not only performs well in expressway/highway for CC, ACC, LK, and LC mode, respectively, but also extends the low speed capability in the urban-road for stop-and-go mode. The implemented system is designed separately with regard to the vehicle longitudinal and lateral dynamics. Besides, to handle the coupling characteristics, a fuzzy systematic design of the combined control of vehicle longitudinal and lateral motions is also presented. Several conventional simplifications or assumptions on vehicle dynamics are not used to access the applicable region of driving conditions. Numerical simulations show the feasibility of our proposed control algorithm and its superior performance in comparison with other approaches.

In the future, we shall conduct more complex situations such as overtaking which can be utilized to dodge the obstacles or overtake a slow-moving vehicle ahead. More sensory systems (e.g., GPS, v-v communication) and sensor-fusion techniques will be more considered in our future design. Besides, for various road conditions in these complex traffic situations, the robustness of control design arises in the variation of tire/ground characteristics (e.g. slip friction on road surface). Furthermore, we shall integrate throttle, brake, and SW to achieve automated driving in urban roads, where more maneuvers are needed to make our driving system available for various driving situations. The adaptive scheme for handling different driving situations is required to be considered in the vehicle-body control design, e.g. adaptive controlling gain maneuver in speed regulation control. A novel spacing policy,

especially for stop-and-go mode, should be developed to grasp the realistic behavior of human drivers such as keeping tightly with the preceding vehicle. In order to achieve the more intact and omnibus automated driving system, the stop-and-go maneuver with extension to the assistance of intersection issue and related work will be our future research works.



References

- [1] H. S. Tan, J. Guldner, S. Patwardhan, C. Chen, and B. Bougler, "Development of an automated steering vehicle based on roadway magnets – case study of mechatronic system design," *IEEE/ASME Trans. Mechatronics*, vol. 4, no. 3, pp. 258-272, 1999.
- [2] R. Rajamani, H. H. Tan, B. K. Law, and W. B. Zhang, "Demonstration of integrated longitudinal and lateral control for the operation of automated vehicles in platoons," *IEEE Trans. Contr. Syst. Technol.*, vol. 8, no. 4, pp. 695-708, 2000.
- [3] T. Hessburg and M. Tomizuka, "Fuzzy logic control for lateral vehicle guidance," *IEEE Control Systems Magazine*, vol. 14, Issue: 4, pp. 55-63, Aug., 1994.
- [4] A. Stentz, M. Hebert, and M. Thorpe, *Intelligent Unmanned Ground Vehicles. Autonomous Navigation Research at Carnegie Mellon*. Norwell, MA: Kluwer, 1997.
- [5] R. E. Fenton and R. J. Mayhan, "Automated highway studies at the Ohio State University – an overview," *IEEE Trans. Vehicular Technology*, vol. 40, no. 1, pp. 100-113, 1991
- [6] C. Hatipoglu, K. A. Redmill and Ü. Özgüner, "Steering and lane change: a working system," in *Proc. IEEE Conf. Intelligent Transportation Systems*, pp. 272-277, Nov., 1997.
- [7] E. D. Dickmanns and D. Mysliwetz, "Recursive 3-D road and relative Ego-state recognition," *IEEE Trans. Pattern Analysis and Machine Intelligence*, vol. 14, no. 2, pp. 199-213, 1992.
- [8] E. Dickmanns, "The development of machine vision for road vehicles in the last decade", in *Proc. IEEE Intelligent Vehicle Symposium*, vol. 1, pp. 268-281, 2002.
- [9] A. Broggi, M. Bertozzi, A. Fascioli, and G. Conte, *Automatic Vehicle Guidance: The Experience of the ARGO Autonomous Vehicle*. Singapore: World Scientific, 1999.
- [10] J. E. Naranjo, C. Gonzalez, J. Reviejo, R. Garcia, and T. Pedro, "Adaptive fuzzy control for inter-vehicle gap keeping," *IEEE Trans. Intelligent Transportation Systems*, vol. 4, no. 3, pp. 132-142, 2003.
- [11] J. E. Naranjo, C. Gonzalez, J. Reviejo, R. Garcia, and T. Pedro, "ACC+Stop&go maneuvers with throttle and brake fuzzy control," *IEEE Trans. Intelligent Transportation Systems*, vol. 7, no. 2, pp. 213-225, 2006.
- [12] J. E. Naranjo, C. Gonzalez, R. Garcia, T. Pedro, and R. E. Haber, "Power-steering control architecture for automatic driving", *IEEE Trans. Intelligent Transportation Systems*, vol. 6, no. 4, pp. 406-415, 2005.
- [13] S. Tsugawa, "Vision-based vehicles in Japan: Machine vision systems and driving

- control systems,” *IEEE Trans. Industrial Electronics*, vol. 41, no. 4, pp. 398-405, 1994.
- [14] S. Kato, S. Tsugawa, K. Tokuda, T. Matsui, and H. Fujiri, “Vehicle control algorithms for cooperative driving with automated vehicles and intervehicle communications”, *IEEE Trans. Intelligent Transportation Systems*, vol. 3, no. 3, pp. 155-161, 2002.
- [15] K. Ni and K. He, “THMR-V: an effective and robust high-speed system in structure road”, in *Proc. IEEE Systems, Man, and Cybernetics*, vol. 5, pp. 4370-4374, 2003.
- [16] C. J. Taylor, J. Kosecka, R. Blasi and J. Malik, “A comparative study of vision-based lateral control strategies for autonomous highway driving,” *International Journal of Robotics Research*, vol. 18, pp. 442-453, 1999.
- [17] Y. Hayakawa, R. White, T. Kimura, and G. Naito, “Driver-compatible steering system for wide speed-range path following,” *IEEE/ASME Trans. Mechatronics*, vol. 9, no. 3, pp. 544-552, 2004.
- [18] C. J. Chen, “The study of the real-time image processing approaches to intelligent transportation systems,” Ph. D. dissertation, National Chiao Tung University, Taiwan, Oct., 2006.
- [19] H. M. Lim and J. K. Hedrick, “Lateral and longitudinal vehicle control coupling for automated vehicle operation,” in *Proc. ACC*, San Diego, 1999, pp. 3676-3680.
- [20] S. J. Xu and J. R. Zhang, “Nonlinear automatic steering control of vehicles based on Lyapunov approach,” in *Proc. 5th Int. Conf. Intelligent Transportation Systems*, Singapore, 2002.
- [21] J. R. Zhang, A. Rachid and S. J. Xu, “Velocity controller design for automatic steering of vehicles,” in *Proc. ACC*, Arlington, 2001, pp. 696-697.
- [22] J. R. Zhang et al., “Automatic path tracking control of vehicles based on Lyapunov approach,” in *Proc. 4th Int. Conf. Intelligent Transportation Systems*, USA, 2001, pp. 370-374.
- [23] H. Lee and M. Tomizuka, “Coordinated longitudinal and lateral motion control of vehicles for IVHS,” *ASME Journal of Dynamics, Systems, and Control*, Vol. 123, pp. 535-543, 2001.
- [24] S. Kumarawadu and T. T. Lee, “Neuroadaptive combined lateral and longitudinal control of highway vehicles using RBF networks,” *IEEE Trans. Intelligent Transportation Systems*, Vol. 7, No. 4, pp. 500-512, 2006.
- [25] B. F. Wu, C. J. Chen, H. H. Chiang, H. Y. Perng, J. W. Perng, L. S. Ma, and T. T. Lee, “The design of an intelligent real-time autonomous vehicle, Taiwan iTS-1,” *J. Chinese Institute of Engineers*, vol. 30, no. 5, pp. 829-842, 2007.

- [26] S. J. Wu and C. T. Lin, "Global optimal fuzzy tracker design based on local concept approach," *IEEE Trans. Fuzzy Systems*, vol. 10, pp. 128-143, 2002.
- [27] S. J. Wu and C. T. Lin, "Optimal fuzzy controller design: Local concept approach," *IEEE Trans. Fuzzy Systems*, vol. 8, no. 2, pp. 1-15, 2000.
- [28] *CarSim User Manual*, Version 5.11, Mechanical Simulation Corporation. 2001.
- [29] <http://www.dspace.com/ww/en/pub/home/products/hw/micautob.cfm>.
- [30] C. H. Yen, "DSP-based intelligent full-speed-range adaptive cruise control design," Master thesis, National Chiao Tung University, Taiwan, July, 2007.
- [31] C. H. Lee, "DSP-based intelligent steering control design for automated lane-keeping and lane-change," Master thesis, National Chiao Tung University, Taiwan, July, 2007.
- [32] S. J. Wu, H. H. Chiang, J. W. Perng, C. J. Chen, B. F. Wu, and T. T. Lee, "The heterogeneous systems integration design and implementation for lane-keeping on a vehicle," accepted to be published in *IEEE Trans. Intelligent Transportation Systems*, Oct., 2007.
- [33] H. H. Chiang, S. J. Wu, J. W. Perng, B. F. Wu, and T. T. Lee, "The human-in-the-loop design approach to the longitudinal automation system for an intelligent vehicle," accepted to be published in *IEEE Trans. Systems, Man, and Cybernetics – Part A: Systems and Humans*, Aug., 2007.
- [34] K. J. Astrom and T. Hagglund. *Automatic Tuning of PID Controllers*. Research Triangle Park, NC: Instrument Society of America, 1988.
- [35] H. Raza and P. Ioannou, "Vehicle following control design for automated highway systems," *IEEE Control Systems Magazine*, vol. 16, no. 6, pp. 43-60, 1996.
- [36] D. C. Liaw, H. H. Chiang, and T. T. Lee, "Elucidating vehicle lateral dynamics using a bifurcation analysis," *IEEE Trans. Intelligent Transportation Systems*, vol. 8, no. 2, pp. 195-207, 2007.
- [37] W. H. Crouse and D. L. Anglin, *Automotive Mechanics*. McGraw-Hill, Inc., 1993.
- [38] G. F. Franklin, J. D. Powell, and A. Emami-Naeini, *Feedback Control of Dynamic Systems*, 3rd Ed. Addison-Wesley, Inc., 1994.
- [39] B. C. Kuo, *Automatic Control Systems*, 7th Ed. Prentice Hall, Inc., 1995.
- [40] R. A. Hess and A. Modjtahedzadeh, "A control theoretic model of driver steering behavior," *IEEE Control Systems Magazine*, pp. 3-8, August, 1990.
- [41] C. Hatipoglu, Ü. Özgüner, and K. A. Redmill, "Automated lane change controller design," *IEEE Trans. Intelligent Transportation Systems*, vol. 4, pp. 13–22, March, 2003.

- [42] G. M. Takasaki and R. E. Fenton, "On the identification of vehicle longitudinal dynamics," *IEEE Trans. Automatic Control*, vol. AC-22, no. 4, pp. 610-615, 1977.
- [43] "ISO 15622: Transportation Information and Control Systems – Adaptive Cruise Control Systems – Performance Requirements and Test Procedures," 2002.
- [44] K. A. Unyelioglu, E. Hatipoglu, and U. Ozguner, "Design and stability analysis of a lane following controller," *IEEE Trans. Control Systems Technology*, vol. 5, no. 1, pp. 127-134, 1997.
- [45] J. Y. Wong, *Theory of Ground Vehicles*, John Wiley & Sons, Inc., 2001.
- [46] S. J. Wu, H. H. Chiang, J. W. Perng, T. T. Lee, and C. J. Chen, "The automated lane-keeping design for an intelligent vehicle," in *Proc. Intelligent Vehicle Symposium 2005*, Las Vegas, 2005, pp. 508-513.
- [47] J. E. Slotine and W. Li. *Applied Nonlinear Control*. Prentice-Hall, Inc., 1991.
- [48] Z. Bareket, P. S. Fancher, H. Peng, K. Lee, and C. A. Assaf, "Methodology for accessing cruise control behavior," *IEEE Trans. Intelligent Transportation Systems*, vol. 4, no. 3, pp. 123-131, 2003
- [49] B. J. Choi, S. W. Kwak, and B. K. Kim, "Design stability analysis of single-input fuzzy logic controller," *IEEE Trans. System, Man, and Cybernetics, Part: B*, vol. 30, no. 2, pp. 303-309, 2000.
- [50] "ISO 15623: Transport Information and Control Systems – Forward Vehicle Following Collision Warning Systems – Performance Requirements and Test Procedures," 2002.
- [51] R. Horst and J. Hogema, "Time-to-collision and collision avoidance systems," in *Proc. 6th ICTCT Workshop*, pp. 1-12, 1988.
- [52] T. Pilutti, G. Ulsoy, and D. Hrovat, "Vehicle steering intervention through differential braking," *ASME J. Dynamic Systems, Measurement, and Control*, vol. 120, pp. 314-321, 1998.
- [53] C. C. MacAdam, "Application of an optimal preview control for simulation of closed-loop automobile driving, " *IEEE Trans. Systems, Man, and Cybernetics*, vol. SMC-11, no. 6, pp. 393-399, 1981.
- [54] H. Perng and M. Tomizuka, "Preview control for vehicle lateral guidance in highway automation," *ASME J. Dynamic Systems, Measurements, and Control*, vol. 115, pp. 679-686.
- [55] E. Ono, S. Hosoe, H. D. Tuan, and S. Doi, "Bifurcation in vehicle dynamics and robust front wheel steering control," *IEEE Trans. Control Systems Technology*, vol. 6, no. 3, pp. 412-420, 1998.

- [56] L. Li, F. Y. Wang, and Q. Zhou, "Integrated longitudinal and lateral tire/road friction modeling and monitoring for vehicle motion control," *IEEE Trans. Intelligent Transportation Systems*, vol. 7, no. 1, pp. 1-19, 2006.
- [57] D. C. Liaw, H. H. Chiang, and T. T. Lee, "Elucidating vehicle lateral dynamics using a bifurcation analysis", *IEEE Trans. Intelligent Transportation Systems*, Vol. 8, No. 2, pp. 195-207, 2007.



Appendix A

The specification of Taiwan *i*TS-1 and equipments are listed in the following tables:

TABLE A.1 Specification of Taiwan *i*TS-1.

Mitsubishi SAVRIN 2.4	
Vehicle width	1.78 m
Vehicle length	4.70 m
Weight	1640 ~ 2200 kg
Engine type	L4 DOHC 16V VVT+DMM
Exhaust	2.4 L
Maximum Horsepower	150/6250 (HP/RPM)
Maximum Torsion	19.2/3000 (KGM/RPM)
Transmission	INVECS-II SPORTS-MODE 4 A/T
Powertrain	Front-wheel drive
Tire	205/65R15

TABLE A.2 List equipments in Taiwan *i*TS-1.

Data Acquiring Sensors	
CCD	Monochromatic CCD
Range finder	Laser range finder (LMS291)
GPS	RTK-DPGS
Signal Processors	
In-vehicle controller	MABX – dSPACE or DSP F2812
Image processor	DM642 – 600 M Hz
GPS processor	DSP C6713DSK
Perception Sensors	
Yaw rate sensor	IMU300CC
Accelerometer	IMU300CC
Velocity	Vehicle speedometer
Actuators	
SW motor	AC motor, MSMA042A1E by panasonic
Throttle motor	DC motor, AP500 by Liteon
Brake motor	DC motor, linear actuator by HIWIN Corp.

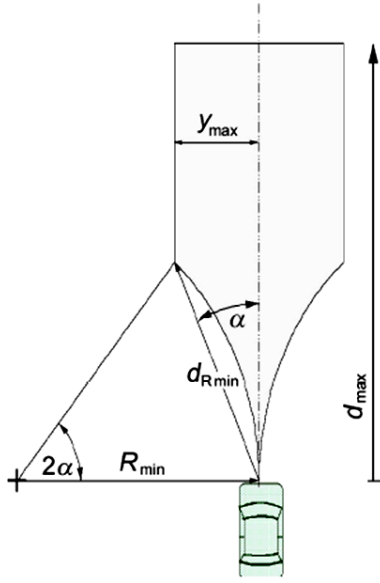
The nominal values of parameters for Taiwan *i*TS-1 is list in the following table:

TABLE A.3 Nominal parameter values of the vehicle platform (Taiwan *i*TS-1)

Symbol and description		Nominal value
m	Mass of the vehicle	1640 ~ 2200 kg
I_z	Yaw moment of inertia	2300 kg*m ²
a	Distance from CG to the front-axle	1.193 m
b	Distance from CG to the rear-axle	1.587 m
L_{wb}	Length of wheelbase	2.78 m
C_f	Total cornering stiffness of the front-tire	131391 Nt/rad
C_r	Total cornering stiffness of the rear-tire	115669 Nt/rad
f	Rotating friction coefficient	0.02
k_D	Drag coefficient from aerodynamics	0.41 Nt*s ² /m ²
k_L	Lift coefficient from aerodynamics	0.005 Nt*s ² /m ²



Appendix B: ISO 15622



- The driving trajectory is a circle with the radius R .
- R is greater than or equal to R_{min} .
- The width of vehicle is neglected.
- Lateral acceleration does not exceed $a_{lateral_max}$.
- Within curves a preview range shall be higher than optional range of ACC systems.
- The preview range is limited by the maximum detection range.

Fig. B.1. Horizontal detection area.

As a minimum requirement the detection and ranging shall cover at least the closest forward vehicle on the assumed trajectory on straight and in the constant radius part of curves. ISO 15622 specifies that the required length of the considered trajectory depends on the vehicle speed, which itself is limited by the maximum speed and lateral acceleration constraints.

Basic HDA formulas:

$$d_R = 2 \sin(\alpha) R \Leftrightarrow \alpha = \arcsin\left(\frac{d_R}{2R}\right) \quad (\text{B.1})$$

$$y_{max} = d_R \times \sin(\alpha) \Leftrightarrow R = \frac{d_R^2}{2y_{max}} \quad (\text{B.2})$$

Limitation of speed in curves to a maximum lateral acceleration:

$$\begin{aligned} \tau_{max}(v_{circle}) &= \frac{d_R}{v_{circle}} \Rightarrow d_R = \tau_{max}(v_{circle}) \times \sqrt{a_{lateral_max} \times R} \\ \Leftrightarrow \tau_{max}(v_{circle}) &= 2 \times \sin(\alpha) \sqrt{\frac{R}{a_{lateral_max}}} \\ \Leftrightarrow \alpha &= \arcsin\left(\frac{\tau_{max}(v_{circle})}{2} \times \sqrt{\frac{a_{lateral_max}}{R}}\right) \\ \Leftrightarrow y_{max} &= \frac{\tau_{max}(v_{circle})^2}{2} \times a_{lateral_max} \end{aligned} \quad (\text{B.3})$$

where $v_{circle} = \sqrt{a_{lateral_max} \times R_{min}}$.

Appendix C

The mathematical form of the Gipps model is shown as

$$V_n(t + \varepsilon) = \min \left\{ \begin{array}{l} V_n(t) + 2.5 \cdot a_n \cdot \varepsilon \cdot \left(1 - \frac{V_n(t)}{V_{no}}\right) \sqrt{0.025 + \frac{V_n(t)}{V_{no}}} \\ b_n \cdot \varepsilon + \sqrt{b_n^2 \cdot \varepsilon^2 - b_n \cdot \left[2 \cdot (X_{n-1}(t) - s_{n-1} - X_n(t) - V_n(t) \cdot \varepsilon) - \frac{V_{n-1}(t)^2}{\hat{b}}\right]} \end{array} \right. \quad (C.1)$$

where parameters are listed as follows:

- a_n Driver's maximum allowable acceleration, vehicle n;
- b_n Driver's maximum allowable deceleration, vehicle n;
- \hat{b} Estimated value for b_{n-1} ;
- s_{n-1} The effective size of vehicle n-1;
- $X_n(t)$ The location of the vehicle n at time t;
- $V_n(t)$ The velocity of vehicle n at time t;
- V_{no} Driver's desired velocity, vehicle n;
- ε The apparent reaction time.



Vita

Name: Hsin-Han Chiang

Personal:

Place of Birth: Kaohsiung, Taiwan, R.O.C.

Day of Birth: Oct. 1, 1979

Education:

<u>Degree</u>	<u>Date</u>	<u>School</u>
B.S. E.C.E	1997 – 2001	National Chiao Tung University, Hsinchu, Taiwan, R.O.C.
M.S. E.C.E	2001 – 2003	National Chiao Tung University, Hsinchu, Taiwan, R.O.C.
Ph.D. E.C.E	2003 – 2007	National Chiao Tung University, Hsinchu, Taiwan, R.O.C.

Advisor(s):

M.S. -

Professor Tsu-Tian Lee, National Chiao Tung University, Hsinchu, Taiwan, R.O.C.

Ph.D. -

Professor Bing-Fei Wu, National Chiao Tung University, Hsinchu, Taiwan, R.O.C.

Professor Tsu-Tian Lee, National Taipei University of Technology, Taipei, R.O.C.



Publication List

Accepted Journal Papers:

- [1] S. J. Wu, H. H. Chiang, H. T. Lin, and T. T. Lee, “Neural-network-based optimal fuzzy controller design for nonlinear systems,” *Fuzzy Sets and Systems*, Vol. 154, pp. 182-207, 2005.
- [2] D. C. Liaw, H. H. Chiang, and T. T. Lee, “Elucidating vehicle lateral dynamics using a bifurcation analysis”, *IEEE Trans. Intelligent Transportation Systems*, Vol. 8, No. 2, pp. 195-207, 2007.
- [3] B. F. Wu, C. J. Chen, H. H. Chiang, H. Y. Peng, J. W. Perng, L. S. Ma, and T. T. Lee, “The design of intelligent real-time autonomous vehicle, Taiwan *iTS-1*”, *Journal of the Chinese Institute of Engineerings*, Vol. 30, No. 5, pp. 829-842, 2007.
- [4] H. H. Chiang, S. J. Wu, J. W. Perng, B. F. Wu, and T. T. Lee, “The human-in-the-loop design approach to the longitudinal automation system for an intelligent vehicle”, accepted to be published in *IEEE Trans. Systems, Man, and Cybernetics-Part A: Systems and Humans*, Aug., 2007.
- [5] S. J. Wu, H. H. Chiang, J. W. Perng, C. J. Chen, B. F. Wu, and T. T. Lee, “The heterogeneous systems integration design and implementation for lane-keeping on a vehicle”, accepted to be published in *IEEE Trans. Intelligent Transportation Systems*, Oct., 2007.

Submitted Journal Papers:

- [1] S. J. Wu, C. T. Wu, H. H. Chiang, S. S. Yu, T. T. Lee, “Neural-fuzzy control design for current-controlled magnetic bearings with minimum power,” submitted to *IEEE Trans. Neural Networks*, Oct. 2007.
- [2] S. J. Wu, H. H. Chiang, J. W. Perng, B. F. Wu, and T. T. Lee, “Toward driver-free automated vehicle control systems on Taiwan *iTS-1*,” submitted to *IEEE/ASME Trans. Mechatronics*, Nov. 2007.

International Conference Papers:

- [1] H. H. Chiang, S. J. Wu, and T. T. Lee, "Application of fuzzy sets theory in process data filtering", in *Proc. IEEE International Conference on Fuzzy systems*, pp. 325-330, 2003, Minnesota, USA.
- [2] H. H. Chiang, S. J. Wu, and T. T. Lee, "Fuzzy approach for disturbance reduction", in *Proc. IEEE International Symposium on Computational Intelligence in Robotics and Automation (CIRA'03)*, pp. 1416-1420, 2003, Kobe, Japan.
- [3] S. J. Wu, H. H. Chiang, J. H. Chen, and T. T. Lee, "Optimal fuzzy control design for half-car active suspension systems", in *Proc. IEEE International Conference on Networking, Sensing, and Control (ICNSC'04)*, pp. 583-588, 2004, Taipei, Taiwan.
- [4] D. C. Liaw, H. H. Chiang, and T. T. Lee, "A bifurcation study of vehicle's steering dynamics", in *Proc. IEEE Intelligent Vehicles Symposium (IV'05)*, pp. 388-393, 2005, Las Vegas, USA.
- [5] S. J. Wu, H. H. Chiang, J. W. Perng, T. T. Lee, and C. J. Chen, "The automated lane-keeping design for an intelligent vehicle", in *Proc. IEEE Intelligent Vehicles Symposium (IV'05)*, pp. 508-513, 2005, Las Vegas, USA.
- [6] S. J. Wu, G. Z. Zeng, H. H. Chiang, and T. T. Lee, "Application of optimal fuzzy tracking control for automotive driving", in *Proc. IEEE International Conference on Systems, Man, and Cybernetics (SMC'05)*, pp. 3319-3324, Hawaii, 2005, USA.
- [7] H. H. Chiang, L. S. Ma, J. W. Perng, B. F. Wu, and T. T. Lee, "Longitudinal and lateral fuzzy control systems design for intelligent vehicles", in *Proc. IEEE International Conference on Networking, Sensing, and Control (ICNSC'06)*, pp. 573-578, 2006, Florida, USA.
- [8] H. H. Chiang, J. W. Perng, B. F. Wu, S. J. Wu, and T. T. Lee, "The human-in-the-loop design approach to the longitudinal automation system for the intelligent vehicle, TAIWAN iTS-1", in *Proc. IEEE International Conference on Systems, Man, and Cybernetics (SMC'06)*, pp. 383-388, Oct. 8-11, 2006, Taipei, Taiwan.
- [9] B. F. Wu, T. W. Chang, J. W. Perng, H. H. Chiang, C. J. Chen, T. Y. Liao, S. J. Wu, and T. T. Lee, "Design and implementation of the intelligent stop and go system in smart car, TAIWAN iTS-1", in *Proc. IEEE International Conference on Systems, Man, and Cybernetics*, pp. 2075-2080, Oct. 8-11, Taipei, Taiwan, 2006
- [10] H. H. Chiang, B. F. Wu, T. T. Lee, and J. W. Perng, "Integrated headway adaptation with collision avoidance system for intelligent systems," in *Proc. IEEE International Conference on Systems, Man, and Cybernetics (SMC'07)*, pp. 3276-3281, Oct. 7-10,

Montreal, Canada, 2007.

- [11] B. F. Wu, T. T. Lee, H. H. Chiang, J. J. Jiang, C. N. Lien, T. Y. Liao, and J. W. Perng, “GPS navigation based autonomous driving system design for intelligent vehicles,” in *Proc. IEEE International Conference on Systems, Man, and Cybernetics (SMC’07)*, pp. 3294-3299, Oct. 7-10, Montreal, Canada, 2007.

